DI ALEXANDER MEIERHOFER

A new Wheel-Rail Creep Force Model based on Elasto-Plastic Third Body Layers

DISSERTATION

zur Erlangung des akademischen Grades eines

Doktors der technischen Wissenschaften

eingereicht an der

TECHNISCHEN UNIVERSITÄT GRAZ

Betreuer und Erstbegutachter

Ao.Univ.-Prof. Dipl.-Ing. Dr.techn. Peter Dietmaier

Zweitbegutachter

Prof. Roger Lewis, MEng. PhD. CEng. FIMechE.

Graz, Juni 2015

Eidesstattliche Erklärung

Ich erkläre an Eides statt, dass ich die vorliegende Arbeit selbstständig verfasst, andere als die angegebenen Quellen/Hilfsmittel nicht benutzt, und die den benutzten Quellen wörtlich und inhaltlich entnommenen Stellen als solche kenntlich gemacht habe.

Graz, im Juni 2015 .....

Alexander Meierhofer

Acknowledgement

First, and foremost, I want to thank Klaus Six for his never ending patience, his guidance and support. Without him, this work would have never been possible. And I sincerely hope that, one day, I will be able to inspire others as he did inspire me.

Next, I have to thank Peter Dietmaier. He is one of the most knowledgeable persons I know. When I was in danger to get lost in details, he never lost track and reminded me of what is important .

I also want to mention Christof Marte and Martin Rosenberger, who were always sympathetic and did support me from the beginning. But most importantly, they kept all the bureaucracy far away from me, so that I could fully focus on my tasks.

Next, I have to thank Gabor Müller. He did a lot of the work with SIMPACK and it is a pleasure to work with him.

Then, there are all the others that inspired and helped me more indirectly: Anna Aichmayer, Josef Fuchs, Bernd Luber, Christian Nussbaumer, Robert Szlozarek, Bettina Suhr, Christof Bernsteiner, and, most importantly, Gerald Trummer. The discussions during lunch and during our coffee breaks always helped me to relax, clear my head, and regain my strength.

An old proverb says that a healthy mind needs a healthy body. Darko Stanisavljevic and Jürgen Zernig helped me to experience the truth of these words. Thank you for that.

Also very important were the people I met during my visit in Sheffield. Although there were many others, the most important ones are Chris Hardwick, Austin Lafferty, Michael Beck, who made my stay very enjoyable. In addition, I want to especially mention Roger Lewis. Without him, this work would not be what it is today.

Next, I wish to thank the "COMET K2 Forschungsförderungs-Programm" of the Austrian Federal Ministry for Transport, Innovation and Technology (BMVIT), the Austrian Federal Ministry of Economy, Family and Youth (BMWFJ), Österreichische Forschungsförderungsgesellschaft mbH (FFG), Das Land Steiermark, and Steirische Wirtschaftsförderung (SFG) for their financial support.

I would also like to thank the supporting companies and project partners: L.B. Foster Rail Technologies, ÖBB Infrastruktur AG, Siemens AG, and voestalpine Schienen GmbH, as well as Graz University of Technology.

Last, but not least, I wanted to thank all the other people in my life that helped and supported me over the years.

Hühnchen mit Brokkoli

Graz, February 2015 Alexander Meierhofer

Abstract

The accurate prediction of the wheel-rail creep forces is essential for a correct description of the vehicle-track interaction. This affects, e.g., wear and damage on wheel and rail, traction and braking behaviour, and vehicle dynamics. Therefore, factors influencing the creep force were investigated closely in this work: vehicle tests and Twin-Disc tests were performed for different creepages, different contact conditions (i.e., dry, wet, dry-sanded, wet-sanded), different speeds, and different normal loads.

The measured results were compared to three existing creep force models (FASTSIM, Polach model, Tomberger model). While these models were able to reproduce individual effects, none of them was able to satisfyingly replicate all measured effects, especially not the normal load dependency or transient effects caused by rapid changes of the creepage.

To investigate the normal load dependency in detail, High Pressure Torsion (HPT) tests were performed in this work. These tests showed a non-linear dependency of the friction on the displacement (similar to strain-hardening known from elasto-plastic materials) and the normal stress (comparable to the behaviour of granular materials). Additional investigations of the Twin-Disc surfaces using optical microscopy revealed the presence of a Third Body Layer (3BL), which is up to 50 µm thick and consists of compressed iron and iron oxide particles.

This information was used to create a new Extended Creepforce (ECF) model. There, it is assumed that an elasto-plastic 3BL, with normal stress and temperature dependent material properties, is present in-between the elastic wheel and rail. Additionally, the ECF model is formulated to include a full time dependency to reproduce transient effects caused by rapid changes in creepage, normal load, or geometry.

The ECF model was then parametrized and validated by HPT tests, Twin disc tests and vehicle tests. Therefore, the model was also implemented in Multi Body System (MBS) software. It was able to reproduce all measured effects qualitatively and quantitatively for all investigated normal loads, vehicle speeds, and contact conditions, including transient effects caused by rapid changes of the creepage.

In the future, the ECF model will be used for a multitude of applications, ranging from the investigation of drive-train and vehicle-dynamics with MBS software to improvements of wear and damage predictions or optimizations of traction and braking control devices.

Kurzfassung

Eine präzise Vorhersage der Kräfte zwischen Rad und Schiene ist essentiell für eine korrekte Beschreibung der Fahrzeug-Fahrwegs-Interaktion. Diese beeinflusst z.B. die Fahrzeugdynamik, das Brems- und Antriebsverhalten und auch den Verschleiß und die Schädigung von Rad und Schiene. In dieser Arbeit wurden daher beeinflussende Faktoren genauer untersucht: Fahrzeugtests und Twin-Disc-Tests wurden für unterschiedliche Schlüpfe, Kontaktbedingungen (z.b. trocken, nass, gesandet), Fahrzeuggeschwindigkeiten und Normallasten durchgeführt.

Die gemessenen Resultate wurden mit drei existierenden Kraftschlussmodellen (FASTSIM, Polach-Modell und Tomberger-Modell) verglichen. Zwar konnten diese Modelle einzelne Effekte nachbilden, aber keines war in der Lage das gemessene Gesamtverhalten zufriedenstellend zu reproduzieren. Vor allem die Normalspannungsabhängigkeit und transiente Effekte, verursacht durch schnelle Änderungen des Schlupfes, verursachten Probleme.

Um die Normalspannungsabhängigkeit genauer zu untersuchen, wurden im Zuge dieser Arbeit High-Pressure-Torsion-Tests (HPT-Tests) durchgeführt. Diese Tests zeigten einen nichtlinearen Zusammenhang zwischen Reibung und Verschiebung (ähnlich der Kaltverfestigung in elasto-plastischen Festkörpern) und der Normalspannung (vergleichbar mit dem Verhalten von granularen Materialien). Zusätzliche optische Untersuchungen der mikroskopischen Twin-Disc-Oberflächen zeigten das Vorkommen eines Third-Body-Layers (3BL), welcher bis zu 50 µm dick ist und aus komprimierten Eisen- und Eisenoxid-Partikeln besteht.

Diese Informationen wurden für die Entwicklung eines neuen erweiterten Kraftschlussmodells (ECF-Modell) benutzt. Dabei wurde angenommen, dass sich zwischen Rad und Schiene ein elasto-plastischer 3BL befindet, welcher normalspannungs- und temperaturabhängige Materialeigenschaften besitzt. Zusätzlich wurde im ECF-Modell die volle Zeitabhängigkeit berücksichtigt um transiente Effekte nachzubilden, welche durch schnelle Änderungen von Schlupf, Normallast oder Kontaktgeometrie entstehen können.

Das ECF-Modell wurde dann anhand von HPT-Tests, Twin-Disc-Tests und Fahrzeugtests parametrisiert und validiert. Dafüer wurde das Model auch in eine Multi-Body-System-Software (MBS-Software) eingebaut. Das Modell war in der Lage, alle gemessenen Effekte sowohl qualitativ als auch quantitativ zu reproduzieren: für alle untersuchten Normallasten, Fahrzeuggeschwindgkeiten und Kontaktbedingungen, aber auch transientes Verhalten, verursacht durch schnelle Änderungen des Schlupfes

In der Zukunft wird das ECF Modell für eine Vielzahl von Anwendungen verwendet werden, welche von Untersuchungen der Dynamik des Antriebsstrangs oder des Gesamtfahrzeugs mit Hilfe von MBS-Software bis hin zu Verbesserungen im Bereich von Verschleiß- und Schädigungsvorhersage oder der Optimierung von Antriebs- und Bremsregelungen reichen werden.

Contents

Abbreviations

Abbreviation	Description
3BL	Third Body Layer
ECF	Extended Creepforce
DC	Dry conditions
DS	Dry-sanded conditions
DSL	Dry-sanded conditions with low amount of sand
DSH	Dry-sanded conditions with high amount of sand
HPT tests	High Pressure Torsion tests
MBS	Multi Body System
PO model	Polach model
TD tests	Twin-Disc tests
TO model	Tomberger model
VH tests	Vehicle tests
WC	Wet conditions
WS	Wet-sanded conditions
WSL	Wet-sanded conditions with low amount of sand
WSH	Wet-sanded conditions with high amount of sand

Symbols

Latin

Symbol	Description
a	Semi-axes of elliptic contact in x-direction
b	Semi-axes of elliptic contact in y-direction
B	Bristle
c	Creepage
c_1	Initial creepage of the time dependent step function
c_2	End creepage of the time dependent step function
C_L	Stiffness of the long axle
C_S	Stiffness of the short axle
C_M	Stiffness of the drive shaft
c_m	Mean value of unsteady state oscillations
c_A	Amplitude of unsteady state oscillations
c_x	Longitudinal creepage
c_y	Lateral creepage
c_s	Spin creepage
$c_{x,L}$	Longitudinal creepage of the wheel on the long axle
$c_{x,S}$	Longitudinal creepage of the wheel on the short axle
D_L	Damping of the long axle
D_S	Damping of the short axle
D_M	Damping of the drive shaft
L_e	Inverted elastic stiffness
L_e^0, L_e^p, L_e^T	Material parameters describing the elastic behaviour of the 3BL
L_p	Plasticity factor
L_p^0, L_p^p, L_p^T	Material parameters describing the plastic behaviour of the 3BL
E_i	Young's modulus of the body i
E^*	Equivalent Young's modulus
f_0	Frequency of unsteady state oscillation
f	Traction coefficient
f_L	Traction coefficient of the wheel on the long axle
f_S	Traction coefficient of the wheel on the short axle

Symbol	Description
F_1, F_2	Functions to calculate the size of the contact in Hertzian theory
F_L	Creep force on the wheel on the long axle
F_S	Creep force on the wheel on the short axle
F_N	Normal load
$F_{N,\text{Line}}$	Line load
g	Ratio of the equivalent curvatures
h	Thickness of 3BL
H_A	Humidity of air
j_G	Gear ratio
J_L	Moment of inertia of the wheel on the long axle
J_S	Moment of inertia of the wheel on the short axle
J_M	Moment of inertia of the motor
J_G	Moment of inertia of the gear wheel
k_q	Percentage of plastic work that dissipates into heat
k_T	Correction factor necessary to adjust for elasticity in gear
p	Normal stress
p_0	Maximum normal stress
$\dot{q}$	Frictional power density
R	Wheel radius
R_1	Regime of steep increase of traction for very low creepages
R_2	Regime of moderate increase of traction for medium creepages
R_3	Regime of traction loss for very high creepages
R_x	Equivalent curvature in x-direction
$R_{x,i}$	Curvature of the body i in x-direction
R_y	Equivalent curvature in y-direction
$R_{y,i}$	Curvature of the body i in y-direction
R_m	Mean equivalent curvature
R_t	Maximum height of the surface profile
t	Time
T	Temperature
T_0	Room temperature
T_B	Bulk temperature
T_e	Environmental temperature
T_M	Motor torque
T_L	Torque of the long axle measured by a strain gauge
T_{HPT}	Measured torque in HPT tests
T_W	Temperature on surface of wheel
T_R	Temperature on surface of rail

Symbol	Description
u	Displacement
$\overline{u}$	Mean displacement
$\underline{v}$	Vehicle velocity
v	Vehicle speed
$\underline{v}_\omega$	Velocity of rotational centre of the wheel
w_e	Elastic work density
w_p	Plastic work density
w_t	total work density
x	Coordinate in longitudinal direction
y	Coordinate in lateral direction
z	Coordinate in normal direction

Greek

Symbol	Description
μ	Coefficient of friction in Coulomb's law
ν_i	Poisson ratio of body i
ϕ	Phase difference of the unsteady state oscillation
τ	Tangential or shear stress
τ_{c1}	First critical shear stress
τ_{c1}^0, τ_{c1}^p, τ_{c1}^T	Material parameters describing the behaviour of τ_{c1}
τ_{c2}	Second critical shear stress
τ_{c2}^0, τ_{c2}^p, τ_{c2}^T	Material parameters describing the behaviour of τ_{c2}
ω	Angular speed in HPT tests
ω_L	Angular speed of the wheel on the long axle
ω_S	Angular speed of the wheel on the short axle
ω_M	Angular speed of the motor
ω_G	Angular speed of the gear wheel
$\omega_{M,i}$	Angular speed of the motor of the i-th wheelset
$\omega_{M,des}$	Desired angular speed of the motor given to the controller
ϕ_L	Angle of revolution of the long axle
ϕ_S	Angle of revolution of the short axle
ϕ_M	Angle of revolution of the motor
ϕ_G	Angle of revolution of the gear wheel

1 Introduction

The accurate prediction of the creep force in railway systems is essential to correctly describe the vehicle-track interaction. Dividing the creep force by the normal load results in the traction coefficient (f). Although the name suggests that this value might be constant, recent publications presented in 1.1 have shown that the traction coefficient of the wheel-rail contact depends on many different parameters. The most important is the creepage. Depicting the dependency of the traction coefficient on the creepage is called the traction characteristic. Other examples for influencing factors are vehicle speed, normal load, and contact geometry. These dependencies affect, e.g., the quality of vehicle dynamic simulations, the control of traction and braking behaviour, or also the prediction of wear and damage on wheel and rail. Therefore, a lot of research has been done to develop a multitude of different creep force models which can be attributed to the multiple fields of application. Some of these models are able to reproduce certain effects qualitatively or even quantitatively, but none of them is capable of reproducing all effects measured in tests.

1.1 Known Effects from Literature

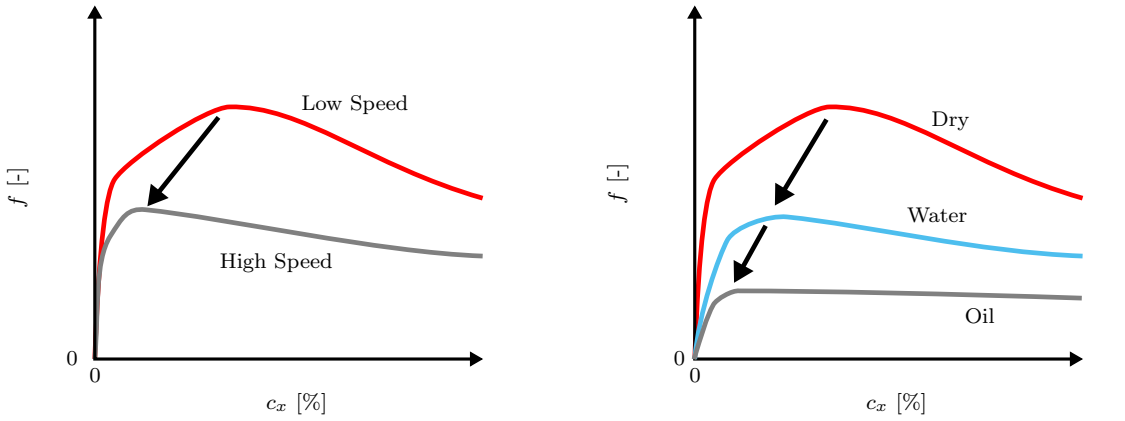

(a) Influence of the speed

(b) Influence of different contaminants in the contact

Fig. 1.1: Qualitative sketch of different traction characteristics: the traction coefficient (f) depending on the longitudinal creepage (c_x) for (a) different vehicle speeds and (b) different contaminants present in the contact. The black arrows indicate the shift of the traction maximum.

Some of the effects that have been shown in measurements are:

- The shape of the characteristic itself. An initial steep increase of traction for low creepages can be observed, then a moderate increase for medium creepages, before a maximum traction is achieved. For even higher creepages, the traction coefficient decreases again [1–4]. This is qualitatively shown as a sketch in Fig. 1.1 for different vehicle velocities and contaminants present in the contact.
- A shift of the maximum of the traction coefficient. For lower speeds, this maximum occurs at higher creepages than for high speeds. This has been shown for dry contact conditions in vehicle tests [1]. In addition, contaminating the contact with water or oil based lubricants, results in a similar shift of the maximum [5–9]. This shift of the maximum is indicated by the arrows in Fig. 1.1.
- A change of the overall traction level of the characteristic. This can again be attributed to the vehicle speed. For higher speeds, the whole characteristic shifts to lower traction levels, leading to a decrease of traction [2, 3]. The same is true for different contact conditions, e.g., lubrication with water or oil based lubricants [2, 10]. A sketch of this behaviour is shown in Fig. 1.1.
- The decrease of the maximum of the traction characteristic with increasing normal loads for dry conditions [2, 7–9, 11, 12]. This behaviour is similar to the speed dependency presented in Fig. 1.1(a)
- Influence of surface roughness: under dry conditions, the influence of the roughness seems negligible [7], while it is said to have an influence for watered conditions [11].
- Change of the behaviour of the traction characteristic due to contaminants in the contact [2, 5, 8, 9, 13–16]. Fig. 1.1(b) shows a sketch for three different contact conditions. For dry conditions, there is a steep increase in the traction coefficient for low creepages and a large decrease for high creepages. This increase and decrease is less pronounced for wet conditions [1]. For oiled conditions, there is only a soft increase for low creepages while the decrease for high creepages seems negligible [2].

1.2 Goals

The goals of this work are:

- A systematic investigation of the effects mentioned in the literature by vehicle tests and Twin-Disc tests.
- A comparison between the measured effects and three existing models and an analyse of the shortcomings of the different models.

- The development of a new more powerful and accurate creep force model, called Extended Creep Force (ECF) model that is able to reproduce all measured effects sufficiently.
- Parametrization and validation of the ECF model using experimental test data.

First, Chapter 2 gives an overview of the existing rolling contact theories, the assumptions used, their field of application and their shortcomings. Also, an overview of existing literature is given, focusing on experimental results regarding investigations of creep-forces in the wheel-rail contact.

The experiments specified and performed during this work are presented in Chapter 3. There, the results of those measurements are also compared to three existing models.

Next, the new ECF model is developed and the influence of its parameters is shown in Chapter 4. This ECF model is then parametrized in Chapter 5 and later validated for steady state and unsteady state in Chapter 6.

At the end, the summary can be found in Chapter 7.

2 The Rolling Contact

To correctly describe the wheel-rail interaction, an accurate prediction of the contact forces is essential. These forces result from the three main purposes of the wheel-rail contact as shown in Fig. 2.1 [17]:

- the contact must support the vehicle load,
- it provides guidance during a change of direction,
- it is responsible for the transmission of forces for acceleration or deceleration.

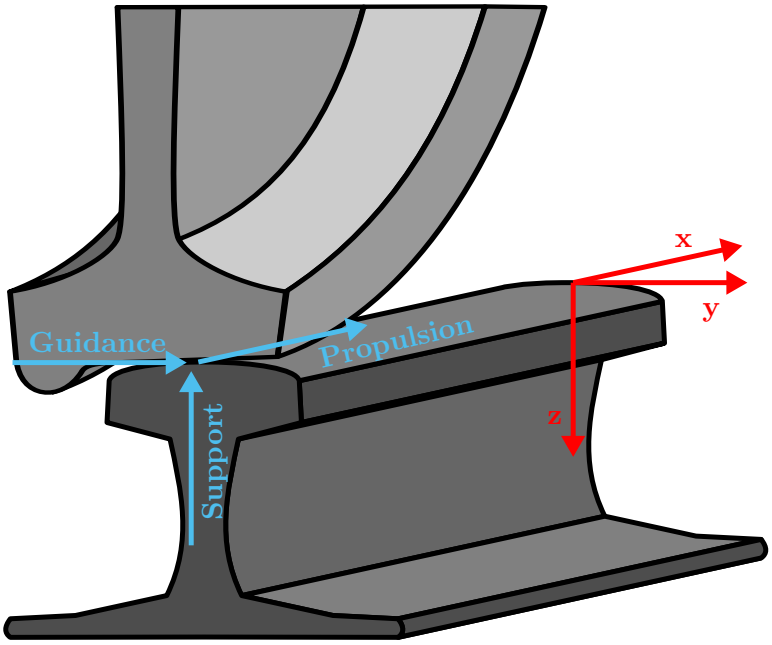

Fig. 2.1: Sketch of the wheel rail contact and its purpose.

The force supporting the vehicle load is one of the solutions of the normal contact problem. Others include the contact position, the shape and size of the contact, the normal stress distribution, and the displacements in normal direction. The solution of the tangential contact problem includes the guidance force and the forces necessary for acceleration and deceleration, as well as the respective displacements. Assuming linear elastic material properties for wheel and rail, the normal and tangential contact problem can be superposed, resulting in a system of differential equations. If the material behaviour can further be described by the same Young's modulus, then the resulting displacements in normal

direction are not dependent on the tangential stresses and vice versa [18–20]. Thus, it is possible to completely separate the problems and to solve them independently.

If a railway vehicle is moving with a constant speed and a constant creepage on a straight track without irregularities and the same contact conditions, the resulting contact forces are time-invariant. In certain scenarios, the contact forces can change rapidly, leading to transient effects. This can be caused by, e.g., the presence of track irregularities, changes in the contact geometry in curves, a sudden change of contact conditions, or rapid changes of the creepage due to drive-train oscillations. It is especially important to consider these effects when investigating dynamics and acoustics. Then, the contact problem including the time dependency must be solved [18, 21, 22].

For a close investigation of the contact forces, it is also necessary to differentiate between conforming and non-conforming contacts. A conforming contact occurs when the contours of the surfaces of the contacting bodies are similar. This happens, e.g., in ball bearings, but, under certain conditions, also in the wheel-rail contact when the profiles are severely worn. There, the contact area is very large and curved (see Fig. 2.2(a)). If the profiles are new, however, the contours of the surfaces are dissimilar, which leads to a non-conforming contact. Then, the contact area is much smaller than the dimensions of the contacting bodies and can be assumed to be nearly flat. This is shown in Fig. 2.2(b).

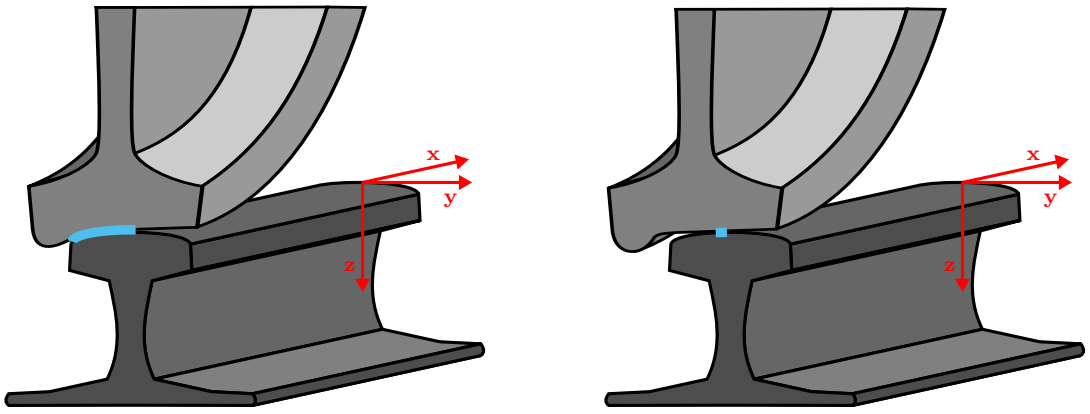

(a) Worn wheel profile: conforming contact

(b) New wheel profile: non-conforming contact

Fig. 2.2: Sketch of a conforming and a non-conforming wheel-rail contact. The blue line indicates the area of contact in both cases.

Typical normal loads for the wheel-rail contact are 60-110 kN. In case of a non-conforming contact, the resulting contact size can be compared to a small coin. This leads to normal stresses that frequently exceed 1 GPa. In addition, shear stresses of up to 0.6 GPa are possible. This causes severe plastic deformations in the near-surface layers of wheel and rail [23–25].

2.1 The Normal Contact Problem

In 1882, Hertz found an analytical solution for the normal contact problem when certain conditions are assumed [19, 20, 26]:

- The materials are isotropic and homogeneous.
- The materials of both, wheel and rail, can be considered elastic.
- There is either no friction between the two bodies or they both have the same Young's modulus and the same Poisson ratio.
- The surfaces of the bodies are continuous and the characteristic dimensions of the bodies are much larger than the size of the contact area. Then, each body can be described by half-space theory.
- The curvature of the bodies' surface can be considered constant in the contact.
- The vehicle speed is much less than the lowest wave propagation speed in the material. Thus, structural oscillations in the material itself have no influence on the solution of the normal contact problem.

Two bodies are pressed together with a normal force (F_N). The surface of the bodies in the contact is described by a polynomial function of second order, where $R_{x,i}$ and $R_{y,i}$ are the curvatures in the x- and y-direction respectively and the index $i = 1, 2$ referring to the respective bodies. Then, equivalent curvatures can be calculated by

$$\begin{aligned} \frac{1}{R_x} &= \frac{1}{R_{x,1}} + \frac{1}{R_{x,2}} \\ \frac{1}{R_y} &= \frac{1}{R_{y,1}} + \frac{1}{R_{y,2}} \end{aligned} \tag{2.1}$$

This reduces the problem of two contacting bodies to the problem of one equivalent body contacting a flat surface. Similar to the equivalent curvature in Eq. (2.1), an equivalent elastic modulus (E^*) can be defined:

$$\frac{1}{E^*} = \left(\frac{1 - \nu_1^2}{E_1} + \frac{1 - \nu_2^2}{E_2} \right) \tag{2.2}$$

Here, ν_i is the Poisson ratio and E_i is the Young's modulus; the index $i = 1, 2$ refers to the respective bodies.

If the equivalent body is not a cylinder, then the shape of the resulting contact is elliptical and a and b are the semi-axis in x- and y-direction respectively.

Then, a mean equivalent radius (R_m) is introduced

$$R_m = \sqrt{R_x R_y} \tag{2.3}$$

which is used, together with the E^* from Eq. (2.2), to calculate a and b [19, 20]:

$$\begin{aligned} a &= F_1(g)\sqrt[3]{\frac{3(1-\nu^2)}{2E}F_N R_m}\sqrt{\frac{g}{F_2(g)}} \\ b &= F_1(g)\sqrt[3]{\frac{3(1-\nu^2)}{2E}F_N R_m}\sqrt{\frac{F_2(g)}{g}} \end{aligned} \tag{2.4}$$

F_1 and F_2 both depend on g, which is the ratio of the equivalent curvatures and relates to the eccentricity of the contact ellipse. It is defined by

$$g^2 = \max\left(\frac{R_x}{R_y}, \frac{R_y}{R_x}\right) \tag{2.5}$$

The values for F_1 and F_2 in dependency of g can be taken from Fig. 2.3.

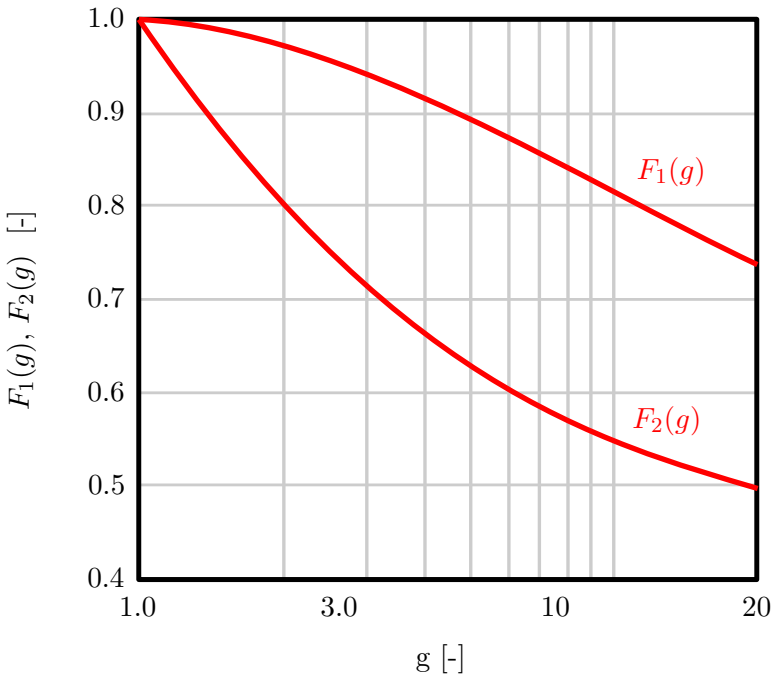

Fig. 2.3: The values for F_1 and F_2 depending on g [19, 20].

The resulting normal stress distribution ($p(x, y)$) is semi-ellipsoidal and given by [19, 20]

$$p(x,y) = \frac{3F_N}{2\pi ab}\sqrt{1-\frac{x^2}{a^2}-\frac{y^2}{b^2}} \tag{2.6}$$

One special case is line contact. There, the equivalent body is a cylinder. This can either be solved by a two dimensional approach or it can be considered as the limit when the equivalent curvature in y-direction (R_y) approaches infinity [19]. Assuming a constant line loading ($F_{N,\text{Line}}$), the resulting contact length (a) and normal stress distribution ($p(x)$)

for line contact are:

$$a = \sqrt{\frac{8\,(1-\nu^2)}{\pi E} F_{N,\mathrm{Line}} R_x}$$
$$p(x) = \frac{2F_{N,\mathrm{Line}}}{\pi a}\sqrt{1-\frac{x^2}{a^2}} \tag{2.7}$$

These assumptions are valid for most cases of wheel-rail contacts. Therefore, most creep-force models rely on the Hertzian theory to solve the normal contact problem. However, non-elliptic contacts do occur. Then, either more computational intensive means, e.g., Finite Element models [27] or CONTACT [28], can be used or approximate models, like the virtual interpenetration method [29–32].

2.2 The Tangential Contact Problem

As mentioned in Chapter 1, there are a multitude of models to solve the tangential contact problem, depending on the application for which it is used.

One of the most important models is CONTACT by Kalker [18]. This algorithm is based on Kalker's Exact Theory, which is able to solve the time dependent normal and tangential contact problem on a discrete grid without separating them. While it is assumed that the wheel and rail are both elastic, isotropic, and homogeneous bodies, it is possible to use different material constants for each. This theory uses Coulomb's Law to calculate the maximum tangential forces possible in the contact. Therefore, the coefficient of friction (μ) must be chosen in advance, manually adjusting it as necessary to take into account different levels of friction due to different surface roughness or contaminants in the contact. It also has a high computational effort, which causes problems when incorporating CONTACT into Multi Body System (MBS) simulations.

Early on, Kalker knew about the problems regarding the computational effort of his Exact Theory. Thus, he presented a Simplified Theory [18]. This theory can only be used if the tangential contact problem can be separated from the normal contact problem, i.e., both bodies consist of the same material. Also, the solution is time-invariant and instead of a any given contact area, only elliptic contacts can be considered. Again, a discrete grid is used. The main idea is that the contacting bodies consist of independent bristles with a constant stiffness. Hence, it is also called a brush model. It can be seen that the stiffness of the bristles, which is derived by comparing the results of the Simplified Theory to the Exact Theory, depends on the shape of the contact, the shear modulus, and the Poisson ratio. Using this stiffness, it is possible to calculate the tangential stresses within the contact and the resulting traction coefficient. Like the Exact Theory, the Simplified one also relies on Coulomb's Law and a user defined coefficient of friction (μ) to determine

the maximum tangential forces in the contact. This theory is the basis for FASTSIM, a very fast algorithm that is state of the art for MBS software.

A different approach to solve the time-invariant tangential contact problem was chosen by Polach [33]. Although this model still uses the Kalker stiffnesses, it does not use a discrete grid. This causes an additional improvement in computational effort compared to FASTSIM. The downside is that it also renders the model unable to deliver certain informations, e.g., local stress distribution in the contact. Recently, this model has been extended to use a discrete grid to circumvent this problem [34]. Its main advantage, however, is that the approach chosen by Polach assumes that the traction depends not only on the creepage but on the relative speed which is the product of the creepage and the vehicle speed. Thus, the Polach model is able to reproduce the vehicle speed dependency and the loss of traction for high creepages mentioned in Section 1.1. In addition, it is also able to replicate the moderate increase for medium creepages by using a variable flexibility depending on the ratio of the area of slip to the area of adhesion. To this end, three empirical functions are used that contain five parameters that must be chosen by the user: the maximum friction coefficient at zero slip velocity (μ_0), the friction coefficient at infinite slip velocity (μ_∞), the coefficient of exponential friction decrease (B), the reduction factor in the area of adhesion (k_A), and the reduction factor in the area of slip (k_S). This phenomenological nature is its biggest shortcoming: for every change in conditions, new tests must be performed to parametrize the values of the used coefficients. Also, no insight in the underlying physics can be gained. Nevertheless, it is one of the most widely used models in standard MBS software because of its low computational effort and its possibility to reproduce many measured effects.

Of course, all of these approaches have been modified and extended in the past by various authors. Recent modifications to Kalker's Exact Theory introduced an elastic Third Body Layer. Also, a relative speed dependent coefficient of friction (μ_s) was added [35]. This model is an advancement because it is now able to describe different initial increases in the traction for low creepages, the traction loss at high creepages, and the speed dependency. The added possibilities rely on phenomenological parameters and, therefore, suffer from the same shortcomings that the Polach model does. Also, the computational effort of this model is similar to CONTACT and, thus, still unsuitable for MBS simulations.

Not only the Exact Theory was extended. Because the Simplified Theory in its original formulation is time-invariant, it has been modified by Alonso and Gimenez to solve the time-dependent tangential contact problem [21]. Similar to the modification in the Exact Theory mentioned above, they were also able to include the loss of traction at high creepages by introducing a second phenomenological coefficient of friction [36], resulting in the same problems that all phenomenological approaches share: the lack of understanding of the underlying physics and the necessity to perform additional tests in order to parametrize the model for every change in conditions.

To avoid this, Tomberger et al. proposed a sub-model based time-invariant model: instead of using phenomenological functions or a user chosen global coefficient of friction, this model calculates a local friction coefficient by using five different sub-models, which take into account micro roughness, interfacial fluids, load dependency, and temperature effects [37]. The model is able to reproduce the traction loss for high creepages and the speed dependency. Two important input parameters of the model are the boundary lubrication factor (k_b), which represents the traction loss due to traces of humidity in the contact, and the roughness factor (k_r), which is a measure for the surface roughness of wheel and rail. However, the influence of solid contaminants is not considered. The model has only been parametrized and validated by data taken from the literature. Also worth mentioning is its high computational effort which makes it infeasible for MBS simulations. Despite these problems, the Tomberger model is more stable considering changes in conditions and gives also a more detailed insight in the actual cause of observed effects. Thus, it is very interesting and similar ideas have been used by other authors recently [38].

One of the goals of this work was to compare the results from vehicle tests and Twin disc tests to existing models. Therefore, three different models were chosen: the original FASTSIM, the original Polach model, and the Tomberger model. FASTSIM and the Polach model are considered state of the art in MBS simulations and, thus, it is of high interest to see how their results compare to measurements. The Tomberger model was chosen because of its sub-model based approach which is a unique idea that might become very relevant for future models.

To compare the prediction quality of these models to test results, the root-mean-square error (RMSE) was calculated:

$$\mathrm{RMSE} = \sqrt{\mathrm{mean}\left(\left[\kappa - \hat{\kappa}\right]^2\right)} \tag{2.8}$$

Here, $\hat{\kappa}$ are the model predictions which are compared to the measured reference values given by κ.

To avoid unit dependencies, the relative error (ϵ) is calculated by using the coefficient of variation of the RMSE:

$$\epsilon = \mathrm{CV(RMSE)} = 100\frac{\mathrm{RMSE}}{\mathrm{mean}\left(\kappa\right)} \tag{2.9}$$

2.3 Experimental Results from Literature

To develop, parametrize, and validate the different models mentioned in Section 2.2, a lot of different tests had to be performed.

One category are the so called vehicle tests. There, a railway vehicle is mounted with sensory equipment. All necessary values are measured either during normal operation or

on a special test track. The results of such tests were published by different authors [1–7, 10, 14] and an overview concerning the measured effects was presented in Section 1.1. Repeating such tests for every conceivable set of parameters and fitting a very simple phenomenological model to reproduce these results would be a valid modelling approach. However, the wheel-rail contact problem is very complex and the parameters range from varying wheel and rail profiles to curve radii, different contact conditions (e.g. dry or wet), changing creepages, different loads, and, last but not least, different vehicles. Even a single vehicle test is very expensive, making it impossible to investigate all of these scenarios in such a way. Also, most tracks are outdoors, which results in a variety of uncontrollable influences regarding contact conditions.

To better control these influences, reduce costs, and automatize the measurements, full-scale roller test rigs were built [11, 39–41]. There, vehicles or bogies are running on a rail that is circumferentially mounted on cylindrical rollers. While these rigs are often used for investigations of noise and oscillations, especially at high speeds, they can also be used to test creepage dependent effects. However, high creepages lead to increased wear and rolling contact fatigue and, thus, the rail needs to be changed more often, which is more expensive on such a full-scale roller test rig than changing a rail on a real track.

A less expensive and less complex alternative under laboratory conditions is a linear full-scale rail-wheel test rig [42–44]. There, a single wheel is pressed with realistic vertical and lateral loads against a rail, which is only a few meters long and moving back and forth with a set speed. By applying a pre-defined angular speed to the wheel, it is possible to prescribe a longitudinal creepage. These test rigs are able to measure the development of rolling contact fatigue, wear, and traction due to different contaminants, creepages, and speeds. However, the capabilities are limited, e.g. the test rig at voestalpine cannot exceed a maximum speed of 0.5 ms^{-1} [44].

An alternative often found in the literature are disc-on-disc tests [8, 9, 12–16, 45–51]: instead of a full-scale wheel and a rail, two cylindrical discs with parallel axes and relatively small diameters, one representing the wheel and one the rail, are pressed against each other with realistic normal stresses known from actual wheel-rail contacts. In case that the two discs share the same dimensions, these tests are called Twin-Disc tests. The State-of-the-Art test rigs mentioned above allow for a separate control of the angular speeds, thus, the reference speed and the longitudinal creepage can be set independently. The main advantage is the relative effortless replacement of the discs, resulting in very low costs compared to all of the previously mentioned tests. However, due to the small disc size and their shape, differences between the actual wheel-rail contact forces and the results of the Twin-Disc tests are expected: e.g., the bulk temperature and the contact shape are different. Therefore, these tests are a very useful tool to investigate the qualitative behaviour of the contact forces for a lot of different parameters with the downside that the scalability of the quantitative behaviour is a complex issue, especially for very small

discs.

Other possible tests include roller-on-rail [52], which is a small version of a full-scale rail-wheel test, or roller-on-disc [53], where a roller rolls on a perpendicularly mounted disc. These tests are similar to the disc-on-disc tests: they are inexpensive and all important parameters can be controlled with the drawback that they are only model representations of the actual problem.

Sometimes, it is necessary to investigate the basic frictional behaviour instead of rolling contacts. Therefore, pin-on-disc tests have been performed in the past [13]. This is increasingly important when investigating contaminated contacts and it is necessary to examine the basic properties of the contaminant. However, these results do not directly translate to the wheel-rail contact forces and using them in an actual creep-force model is a complex task.

3 Experiments

As mentioned in Section 1.1, the traction coefficient is dependent on different parameters. These influences were investigated in the past, amongst others by the tests mentioned in Section 2.3. However, some of these test results were published decades ago with old measurement equipment [1, 10]. In addition, a lot of important knowledge is not available from the literature, e.g. type of vehicle or wheel and rail profiles. Therefore, it was necessary to systematically investigate occurring effects during the work presented in this thesis:

- In Section 3.1, the results of the performed vehicle tests are presented. There, the influence of the creepage, the velocity, and contact conditions on the traction coefficient and transient effects caused by drive train oscillations were investigated. The results of these tests are then compared to the three models mentioned at the end of Section 2.2.
- Because it was not possible to change the normal load in the vehicle tests, additional tests were performed at a Twin-Disc machine. There, it was possible to change the velocity, the normal load, and the creepage. However, the main advantage compared to other measurement methods was the possibility to optically investigate the used discs for every set of parameters to gain insight in their surface and near surface properties. While parts of this study were also previously published by Meierhofer et al. [12], Section 3.2 presents a complete summary and detailed analysis of these Twin-Disc tests.
- One of the goals of this work was to model the influence of roughness, sand, and water on the friction level. Therefore, it was necessary to perform more basic tests to investigate the behaviour and influence of such contaminants. But instead of pin-on-disc tests, which were mentioned in Section 2.3, so called High Pressure Torsion (HPT) tests were used. These tests are a novel approach that has not been mentioned in this way in the literature to the authors knowledge. The main idea was to press two stamps of the same material together with high normal load and then rotate one of the discs. The resulting torque was measured. In these tests, it was possible to apply different normal loads, different roughnesses, and add different contaminants. The goal was to measure the change in the frictional behaviour due to these normal load and contact conditions in dependency of the displacement. A summary of the tests can be found in Section 3.3.

3.1 Vehicle (VH) Tests

In this work, vehicle tests were performed with a Vectron locomotive on the Siemens test ring in Wildenrath. The goal was to measure the influence of certain parameters on the traction coefficient. These parameters were:

- The longitudinal creepage (c_x)
- The vehicle speed (v)
- The influence on the traction if the measurements were performed on different days
- The influence of different sections of the track
- The influence of four different contact conditions: dry conditions (DC), wet conditions (WC), dry with sand (DS), and wet with sand (WS)
- The occurrence of transient effects, i.e., drive-train oscillations, and its influence on the traction characteristic.

The tests were performed on different sections of the test ring as shown in Fig. 3.1(a). The axle load of a Vectron locomotive is 220 kN. Because the measurements were performed on approximately straight tracks, the normal load for one wheel was assumed to be half the axle load: $F_N = 110$ kN.

The tests were also performed on two different days and the environmental temperature (T_e) and humidity of air (H_A) were measured. While the first axle was driven, the second, third, and fourth axle were in pure rolling. A second locomotive was attached that kept the vehicle speed constant. The angular speed of the motor of the first wheelset ($\omega_{M,1}$) and the fourth wheelset ($\omega_{M,4}$) were measured. Because the fourth wheelset was in pure

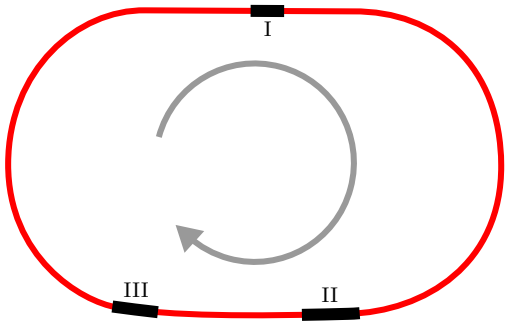

(a) Schematic diagram of the Siemens test ring in Wildenrath with the three sections where the measurements took place. Length of the test ring is 6.1 km, the curve radii are approximately 700 m with a super elevation of 0.15 m.

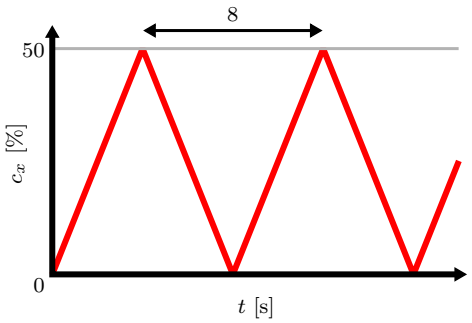

(b) Change of the longitudinal creepage (c_x) over time (t) during the tests.

Fig. 3.1: Schematic overview of the test ring and the applied creepage during the tests.

rolling, the angular speed of its motor, together with the gear ratio (j_G) and the radius of the wheel (R), are used to calculate the vehicle speed (v):

$$v = \frac{\omega_{M,4} R}{j_G} \tag{3.1}$$

Also, the mean longitudinal creepage (c_x) of both wheels on the first wheelset can be approximated by using the angular speeds of the motor of the first wheelset ($\omega_{M,1}$), the vehicle speed (v), and the gear ratio (j_G):

$$c_x = \frac{j_G v - \omega_{M,1} R}{j_G v} \tag{3.2}$$

During each test, the creepage on the wheels of the first axle was changed from 0% to 50% in the time interval $\Delta t = 8$ s as shown in Fig. 3.1(b). The interval was chosen to ensure near quasi-steady behaviour of the drive-train. However, it as unavoidable that oscillations of the drive-train occurred for certain working conditions, causing a transient behaviour. In the following, these two different behaviours are discussed separately.

3.1.1 Quasi-Steady Behaviour of the Drive-Train

To investigate the quasi-steady behaviour, it was possible to calculate the traction coefficient (f) directly from the measured motor torque (T_M), normal load (F_N), the gear ratio (j_G), and the wheel radius (R):

$$f = \frac{-j_G T_M}{2 F_N R} \tag{3.3}$$

In Fig. 3.2(a), the results for a typical traction characteristic are shown. It was calculated

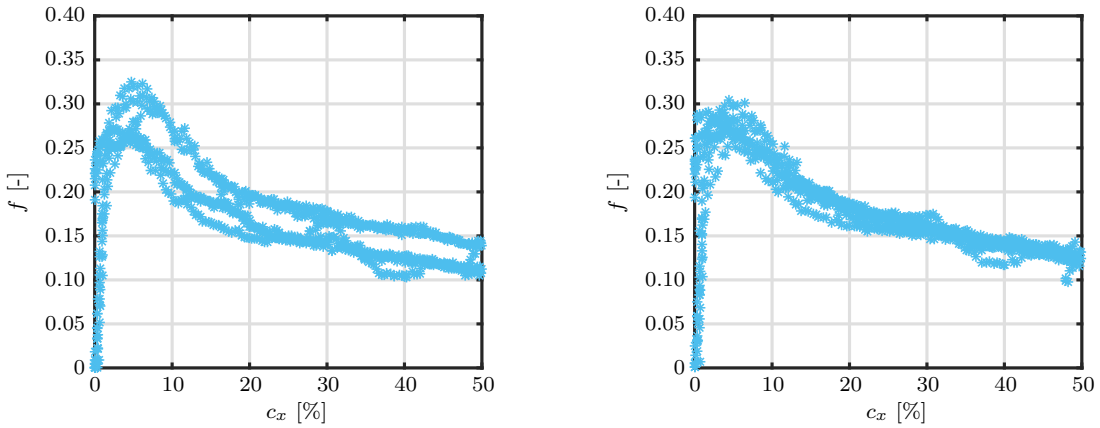

(a) Without compensation for the inertia of the drive-train

(b) An observer is used to compensate for the inertia of the drive-train

Fig. 3.2: Results of the vehicle tests for $v = 10$ ms^{-1} on second day in section II with DC with and without compensation for the inertia of the drive-train.

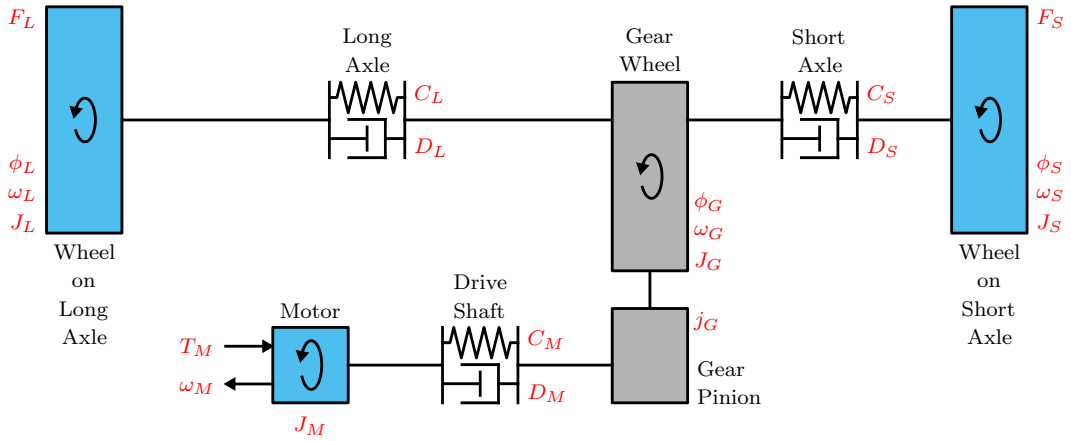

Fig. 3.3: Schematic sketch of the investigated wheelset.

by using Eq. (3.2) and Eq. (3.3) to calculate the longitudinal creepage (c_x) and the traction coefficient (f) respectively. The data presented is from the second day in section II for DC with a speed of $v = 10$ ms^{-1}. Because the creepage is constantly varried from 0% to 50% and back (see Fig. 3.1(b)), a hysteresis is visible, caused by the inertia of the drive-train.

To compensate for this effect, an observer was created and the resulting traction characteristic is shown in Fig. 3.2(b). The used observer was based on the model presented in Fig. 3.3, F_L and F_S were modelled as disturbances. The corresponding equations are:

$$\begin{aligned}
J_L\dot{\omega}_L &= C_L(\phi_G - \phi_L) + D_L(\omega_G - \omega_L) - F_L R \\
J_S\dot{\omega}_S &= C_S(\phi_G - \phi_S) + D_S(\omega_G - \omega_S) - F_S R \\
J_M\dot{\omega}_M &= C_M(j_G\phi_G - \phi_M) + D_M(j_G\omega_G - \omega_M) + T_M \\
J_G\dot{\omega}_G &= C_L(\phi_L - \phi_G) + C_S(\phi_S - \phi_G) + j_G C_M(\phi_M - j_G\phi_G) \\
&\quad + D_L(\omega_L - \omega_G) + D_S(\omega_S - \omega_G) + j_G D_M(\omega_M - j_G\omega_G)
\end{aligned} \tag{3.4}$$

Here, T_M is the motor torque, R the wheel radius, j_G the gear ratio, J_i are the moments of inertia, C_i the stiffnesses, D_i the dampings, ω_i the angular speeds, ϕ_i the angle of revolution, and F_i the frictional forces. The indices $i = L, S, M, G$ denote the wheel on the long and short axle, the motor and the gear respectively. While R, j_G, J_i, C_i, and D_i are known constants, ω_M, T_M were measured during the tests. The mean traction coefficient of both wheels (f) can then be calculated by

$$f = \frac{F_L + F_S}{2F_N} \tag{3.5}$$

Fig. 3.4(a) shows the results of the observed traction characteristic on section II on the second day for $v = 10$ ms^{-1} for 0% to 20% longitudinal creepage (c_x). There are three different regimes visible. In the regime R_1, with low creepages ($c_x \lesssim 2\%$), the increase in traction is very steep. Then, there is a second regime, marked R_2 ($2\% \lesssim c_x \lesssim 5\%$),

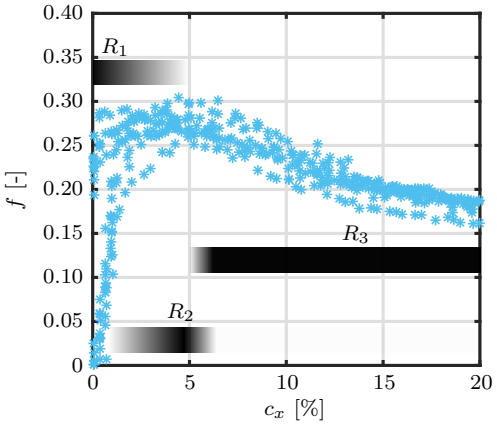

(a) The three different regimes: R_1 shows a high increase in traction for low creepages, R_2 shows a moderate increase for medium creepages, R_3 shows a loss of traction for high creepages.

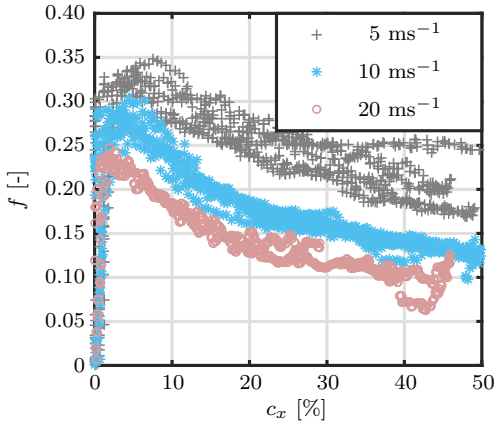

(b) Influence of the vehicle speed: for higher speeds, the traction coefficient decreases for all creepages and the maximum of the traction coefficient moves to the left to lower creepages.

Fig. 3.4: Results of the vehicle tests for (a) $v = 10$ ms^{-1} and (b) three different speeds on second day in section II with DC.

with a moderate increase of traction for medium creepages until the maximum traction coefficient is reached at $c_x \approx 5\%$. Finally, in regime R_3, a loss in traction is visible for high creepages ($c_x \gtrsim 5\%$). Fig. 3.4(b) shows the speed influence for three different speeds and DC. The traction level decreases for higher speeds resulting in the lowest traction level for $v = 20$ ms^{-1}. Also, the maximum of the traction coefficient moves to lower creepages for higher speeds. However, the steep increase for low creepages (R_1) is speed independent.

The results for the first day and the second day are compared for DC in section III in Fig. 3.5. While the maximum traction coefficient is nearly the same for both days, the creepage at which this maximum occurs changes slightly, especially for $v = 20$ ms^{-1}.

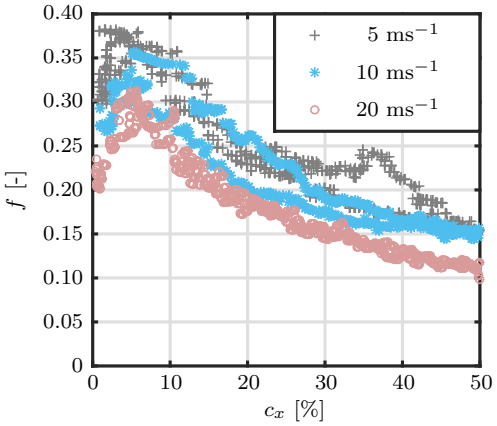

(a) First day, $T_e = 17.7°$C, $H_A = 77.2\%$

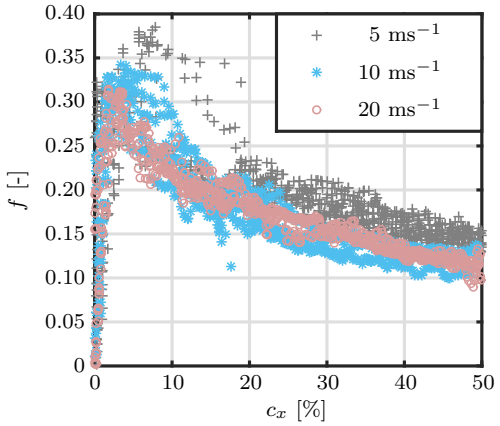

(b) Second day, $T_e = 15°$C, $H_A = 86.8\%$

Fig. 3.5: Results of the vehicle tests for three different speeds on two different days on section III with DC.

Also, the traction coefficient for $c_x = 50\%$ shows some deviations for $v = 10$ ms^{-1} and $v = 20$ ms^{-1}. These differences can be explained by different conditions during the tests: while the tests on the first day were performed during day, with a humidity of air of $H_A = 77.2\%$ and an environmental temperature of $T_e = 17.7°$C, the tests on the second day were performed at night with $H_A = 86.8\%$ and $T_e = 15°$C. The following comparisons take this into account and only results from the same day will be compared.

Next, the results from the three different sections were compared for DC on the second day in Fig. 3.6. In all tests, the slowest speed resulted in the highest traction while the fastest speed showed the lowest traction level. Also, the general behaviour is similar: the three different regimes are clearly observable in all cases. However, the quantitative values show deviations. Also, the speed dependency does not seem to be exactly the same in these measurements. The reasons might be contaminations of the track, uncertainties in the measurements, and slightly different contact geometries.

One goal of the VH tests was to measure the influence of different contact conditions on

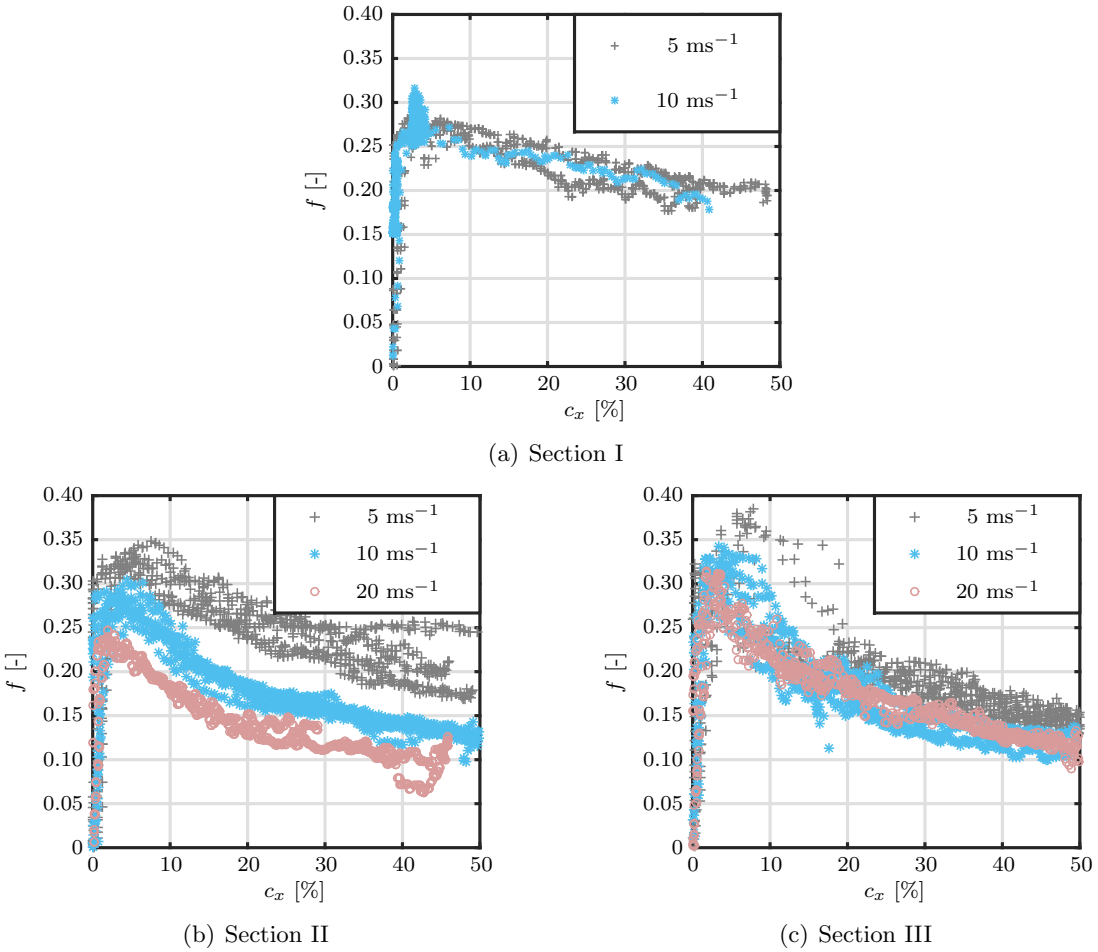

(a) Section I

(b) Section II

(c) Section III

Fig. 3.6: Results of the vehicle tests for different vehicle speeds on the second day on different sections with DC.

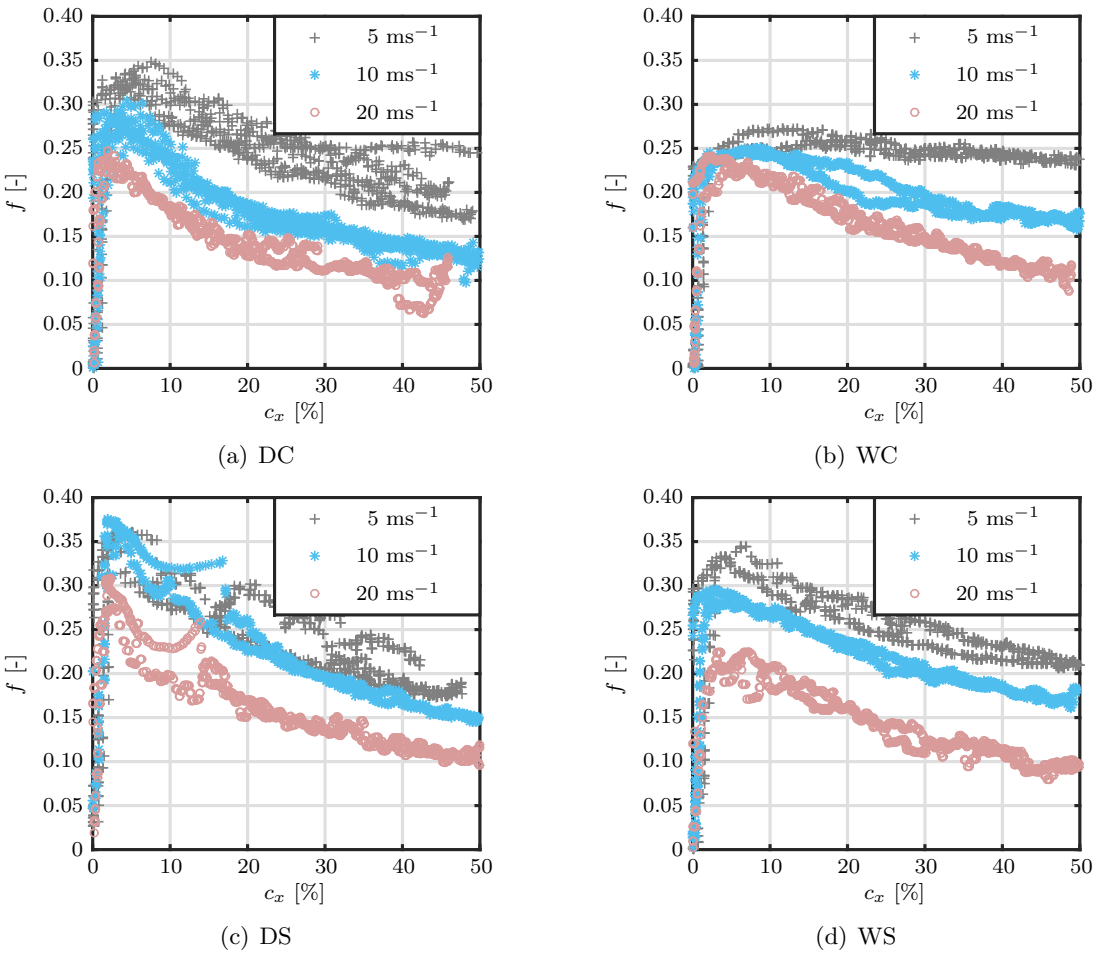

Fig. 3.7: Results of the vehicle tests for different contact conditions: dry (DC), wet (WC), dry with sand (DS), and wet with sand (WS) on the same section on the same day.

the traction coefficient. The results of these investigations are shown in Fig. 3.7. There, the initial increase in traction is the same for all contact conditions, i.e., DC, WC, DS, and WS. This is in contrast to findings from the literature, where different initial increases were reported for wet conditions [1]. Also, all except WC (i.e., DC, DS, and WS) show a qualitative accordance: they have a similar shape for all speeds and similar maxima for $v = 5\,\mathrm{ms}^{-1}$. Although the results are slightly different for $v = 10\,\mathrm{ms}^{-1}$, they all show a similarly high influence of the speed. It can be argued that the differences are not significant as they are in the same order of magnitude as the difference between measurements performed on the first and second day (see Fig. 3.5) and might be attributed to uncertainties in the measurements. Also, it has to be mentioned that there were uncertainties regarding the exact location these measurements took place due to the resolution of the used GPS signal. Another uncertainty are the exact contact geometries that were impossible to measure and can influence the results.

Fig. 3.7(b) shows that the traction characteristic looks different for WC: for all speeds,

the maxima are nearly the same and the increase and loss of traction is less pronounced. Especially for $v = 5$ ms^{-1} and high creepages, the traction loss is nearly non existent.

It is also worth noting that in case of sanded conditions, the original sanding system of the locomotive was used. This system uses a nozzle that always sprays the same amount of sand into the contact, independent of speed. Due to turbulent streams, it is possible that nearly no sand contaminated the contact at high speeds. This might explain why the results for WS and WC look similar in case of $v = 20$ ms^{-1}, while they look different for other speeds.

The next step was to compare the results of the VH tests to the creepforce models that were mentioned in Section 2.2: FASTSIM (FS), the Polach model (PO), and the Tomberger (TO) model. The normal load used in these simulations was 110 kN and the half axis of the contact ellipse were $a = 7.63$ mm and $b = 7.88$ mm, which are reasonable values for the Vectron locomotive on a straight track. The results of these comparisons are shown in Fig. 3.8 and the relative error (ϵ) of the models compared to the test results is given for

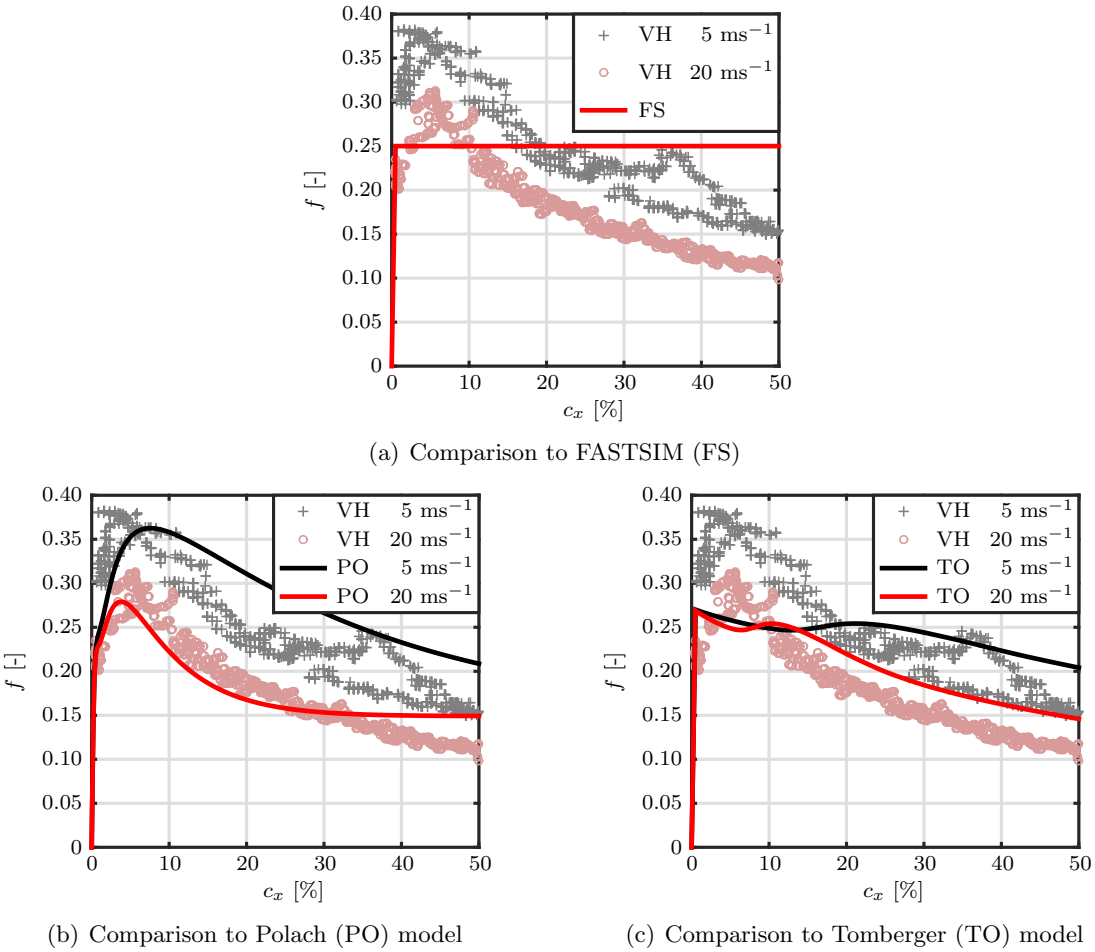

(a) Comparison to FASTSIM (FS)

(b) Comparison to Polach (PO) model

(c) Comparison to Tomberger (TO) model

Fig. 3.8: Comparison of the VH tests in section II under DC to three different models from the literature and a ploynomial fit of the fifth order.

Table 3.1: The relative error as defined by Eq. (2.9) for different models:

Model	5 ms^{-1}	20 ms^{-1}	Mean
FASTSIM	27.58%	49.53%	38.56%
Polach	21.30%	12.73%	17.01%
Tomberger	21.91%	17.07%	19.49%

different vehicle speeds in Tab. 3.1 (see also Section 2.2 and Eq. (2.9)).

As expected, FASTSIM was not able to replicate the vehicle test results, neither qualitatively nor quantitatively. The coefficient of friction in this case was chosen as $\mu = 0.25$ to best reproduce the results for $v = 5$ ms^{-1}. It is not formulated to include speed dependencies, hence the simulated curve is identical for both speeds. As presented in Tab. 3.1, it has the highest relative error. For $v = 20$ ms^{-1}, the error is nearly 50%.

The Polach model, on the other hand, is able to reproduce a speed dependency and a traction loss for high creepages, although the traction level is slightly to high for $v = 5$ ms^{-1} and the traction loss for high creepages does not fit the measured data for $v = 20$ ms^{-1}. This results in a mean error of $\bar{\epsilon} = 17.01\%$. The parameters used for this simulation were $\mu_0 = 0.35$, $\mu_\infty = 0.105$, $B = 0.7$, $k_a = 0.68$, and $k_s = 0.14$. However, these parameters have no physical meaning and must be readjusted for changes in the measurement conditions.

Lastly, the VH tests were compared to the Tomberger model. Here, the boundary lubrication factor of the model was set to $k_b = 0.6$ and the roughness factor to $k_r = 0.5$. The Tomberger model is able to reproduce the speed influence and also the negative gradient for high creepages. This is caused by the included temperature sub-model. On the other hand, the results for low and medium creepages are very different from the test results. In addition, no quantitative agreement could be achieved with the chosen parameters: $\bar{\epsilon} = 19.49\%$. It is worth noting, however, that the Tomberger model was parametrized and validated by using data from the literature. Thus, differences are expected and an extended parametrization and validation might increase the quality of the predicted traction characteristics, but only at high creepages.

While all three models take the stiffness of the wheel and rail material into account, only the Polach model was able to accurately predict the increase of traction for low and medium creepages, resulting in the smallest mean error: $\bar{\epsilon} = 17.01\%$ (see Tab. 3.1). This is the case because Polach uses an phenomenological parameter (k_s) to reproduce the increase in traction at medium creepages. Literature suggests, that these differences for low and medium creepages stem from an elastic-plastic Third Body Layer that is present even under dry conditions [13, 54].

3.1.2 Drive-Train Oscillations

To investigate drive-train oscillations, a strain gauge was applied to the long axle, which was measuring the difference of the angles ϕ_G and ϕ_L. Considering the stiffness of the axle (C_L), the static torque of the long axle (T_L) is obtained by:

$$T_L = C_L(\phi_G - \phi_L) \tag{3.6}$$

The kinematic equation was used to calculate the angular speed for the wheel on the long axle (ω_L) from the angular speed of the motor and gear (ω_M and ω_G respectively) using the gear ratio (j_G):

$$j_G\omega_L = \omega_M - j_G(\omega_M - \omega_G) - j_G(\omega_G - \omega_L) \tag{3.7}$$

Inserting the time derivative of Eq. (3.6) and dividing by j_G gives

$$\omega_L = \frac{\omega_M}{j_G} - (\omega_M - \omega_G) - \frac{\dot{T}_L}{C_L} \tag{3.8}$$

It must be mentioned that the relative angular speed between the motor and the gear box ($\Delta\omega_{M,G} = \omega_M - \omega_G$) was not measured. However, Multi Body System (MBS) simulations showed that $\Delta\omega_{M,G}$ oscillates with the same frequency as $\dot{T}_L$ and a phase difference of half of its wave length, leading to a reduction of the amplitude. Thus, $\Delta\omega_{M,G}$ can be approximated by introducing a correction factor (k_T). Eq. (3.8) then reads:

$$\omega_L = \frac{\omega_M}{j_G} - k_T\frac{\dot{T}_L}{C_L} \tag{3.9}$$

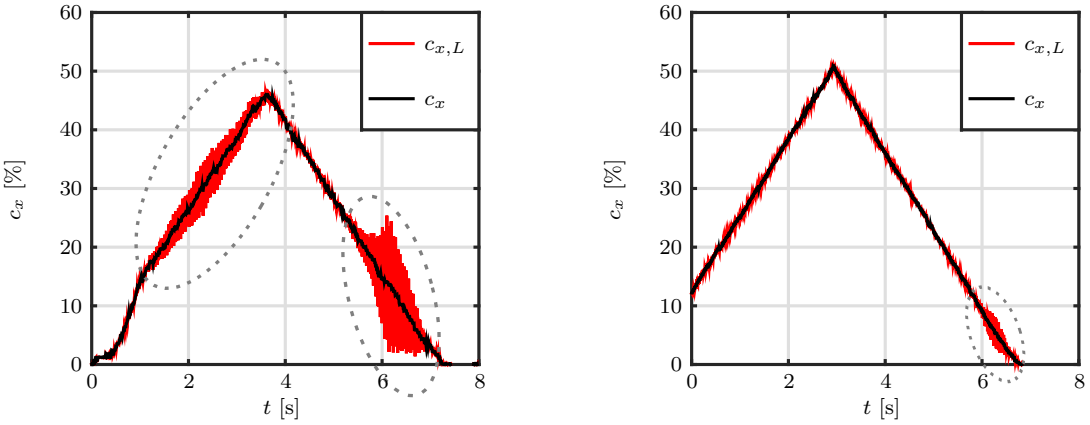

(a) $v = 5$ ms^{-1} (b) $v = 10$ ms^{-1}

Fig. 3.9: Comparison of the measured mean creepage of both wheels (c_x) to the creepage on the wheel on the long axle ($c_{x,L}$) for two different vehicle speeds (v) depending on time (t). The marked areas show the occurrence of drive-train oscillations.

The correction factor was determined by the MBS simulations: $k_T = 0.6$.

Using Eq. (3.9) and the vehicle speed (v), the longitudinal creepage on the long axle ($c_{x,L}$) is expressed as

$$c_{x,L} = \frac{v - \omega_L R}{v} \tag{3.10}$$

The next step is to obtain the frictional force of the wheel on the long axle (F_L) from the equation of motion:

$$J_L \dot{\omega}_L = T_L - D_L \frac{\dot{T}_L}{C_L} - F_L R \tag{3.11}$$

Using the normal load (F_N), this then yields the traction coefficient for the wheel on the long axle (f_L):

$$f_L = \frac{F_L}{F_N} \tag{3.12}$$

The resulting drive-train oscillations are shown over time in Fig. 3.9 for dry conditions and two different vehicle speeds: $v = 5$ ms^{-1} and $v = 10$ ms^{-1}. The frequency of these oscillations is approximately 53 Hz (see the marked areas in Fig. 3.9). They are not symmetric: increasing the creepages leads to different results compared to a decreasing creepage. Also, the amplitude of the oscillations decreases with increasing vehicle speed.

These drive-train oscillations can also be seen in the traction characteristic. To proof this, the traction coefficient of the wheel on the long axle (f_L), calculated by Eq. (3.11) and Eq. (3.12), is compared the mean value of the coefficient of friction for both wheels (f), which was calculated by Eq. (3.4) and Eq. (3.5). The results are plotted over the mean longitudinal creepage (c_x) and are presented in Fig. 3.10. Here, a hysteresis with a complex pattern is visible. Because of the rapid changes of the creepage, it is necessary to develop

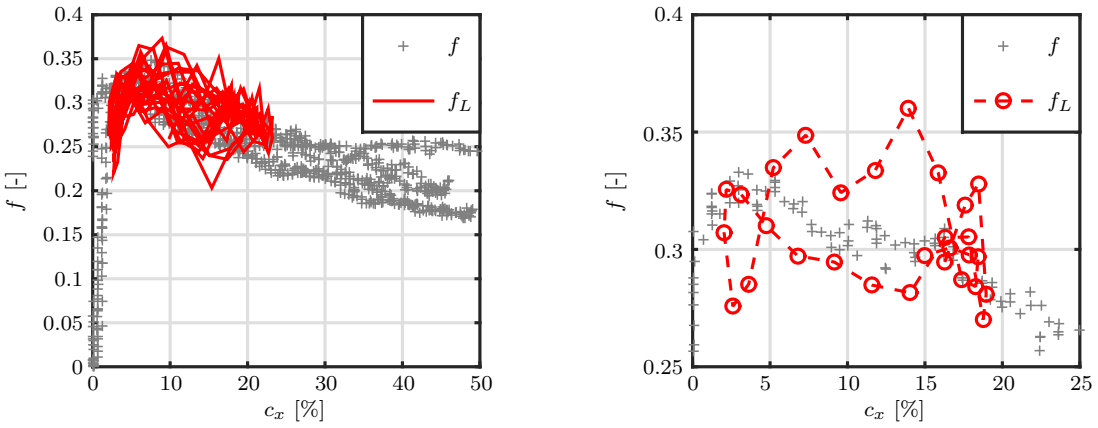

(a) Total result of drive-train oscillations

(b) Close up result for one oscillation

Fig. 3.10: Mean traction coefficient (f) and the traction coefficient of the wheel on the long axle (f_L) depending on the longitudinal creepage (c_x) measured during vehicle tests. A visible hysteresis is caused by drive-train oscillations.

a time dependent model that is able to reproduce such transient effects in order to further investigate such drive-train oscillations.

3.2 Twin-Disc (TD) Tests

There were two main reasons to perform Twin-Disc tests in the presented work: The first was to measure the influence of the normal load on the traction coefficient. The second reason was to investigate the surface and near surface properties of the used discs because the literature suggests that the presence of a solid Third Body Layer (3BL) with elastic-plastic material properties influences the traction characteristic even under dry conditions [13, 54]. The schematics of the test machine is shown in Fig. 3.11, more information regarding the machine was published previously [12, 55, 56]. For the tests, cylindrical discs made of different materials with a diameter of 47 mm and a width of 10 mm were used, thus approximately forming a line contact. In these investigation, R8 wheel material was used for the wheel discs and R260 rail material for the rail disc. Before testing, all discs were polished and cleaned in an ultrasonic acetone bath while great care was taken to avoid a contamination of the discs.

The tests themselves consisted of a measurement of the traction coefficient for different longitudinal creepages (c_x), the speeds (v), and the normal loads (F_N). An overview of the performed measurements can be found in Tab. 3.2. From the literature it was known that it takes a certain amount of time until steady state is reached in these tests [56]. Hence, the tests were performed until a stable value for the traction coefficient was reached which indicated stable frictional properties and, thus, a steady state.

During the testing, the room temperature was in between 20°C and 24°C. The humidity of air was in between 34% and 48%. Additionally, the bulk temperature was measured, as it was not possible to measure the contact temperature directly. The bulk temperature

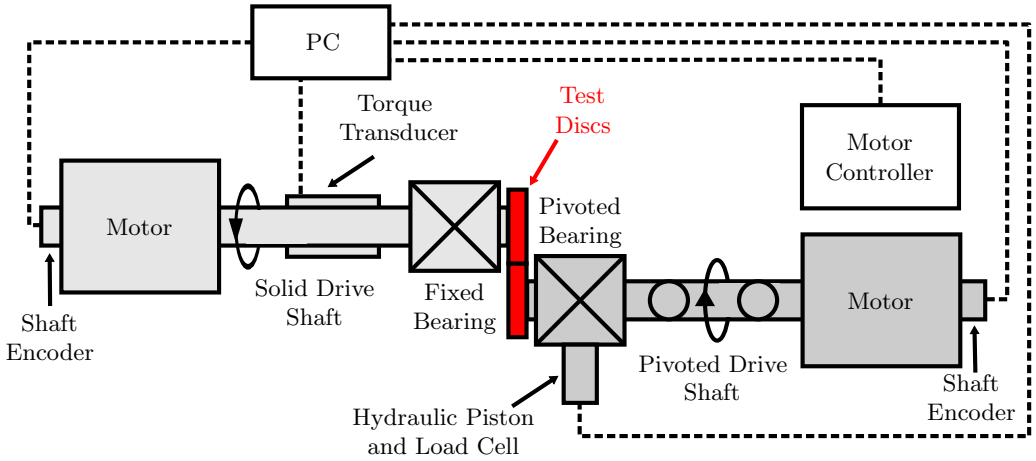

Fig. 3.11: Schematic diagram of the Twin-Disc test rig used [12, 55, 56].

Table 3.2: List of the different performed tests and the respective parameters: speed (v), normal load (F_N), the resulting maximum normal stress (p_0), and longitudinal creepages (c_x).

Test	v [ms^{-1}]	F_N [N]	p_0 [GPa]	c_x [%]
1	0.5	2500	0.9	0.26, 0.47, 1.09, 1.54, 3.08, 5.06, 5.11
2	0.5	7100	1.5	0.04, 1.05, 4.54
3	1	2500	0.9	0.08, 0.24, 0.45, 3.00, 5.00, 5.00
4	1	7100	1.5	0.00, 0.09, 0.31, 0.50, 1.00, 2.00, 5.00

never exceeded 100°C. Also, the discs were encased in a box that was used to collect wear debris. Later investigations of the composition of the wear debris are an indication of the composition of the resulting Third Body Layer (3BL) that was formed during the tests on the surface of the discs.

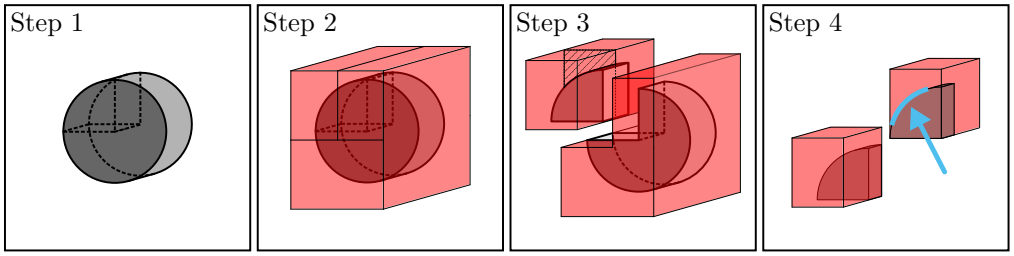

Fig. 3.12: After the tests, the discs were embedded in a resin. Later, they were sectioned. The blue arrow indicates the area that was microscopically investigated.

After the Twin-Disc tests were performed, the discs were embedded in a resin for subsequent microscopical investigations. Fig. 3.12 shows the sectioning of the discs where the blue arrow and the blue line indicate the area that was microscopically investigated. The results were then compared to the microscopical investigation of unused discs that served as baselines.

3.2.1 Twin-Disc Test Results

On the surface of the rail discs, microscopical investigations show a flake like structure with cracks where also small particles can be seen in Fig. 3.13. While these cracks can also be found on the surface of the wheel disc, the more striking feature is a formation of a layer of compacted particles (see Fig. 3.14).

The variance of the thickness of the layer is ± 20% for a given set of parameters. For creepages below 1%, the layer only covers parts of the surface. A continuous layer can be found covering the whole surface for higher creepages. The maximum observed thickness was 50 µm in uncompressed state when loaded with $c_x = 5\%$, $v = 0.5$ ms^{-1}, and $p_0 = 1.5$ GPa. Its thickness increases with increasing normal load and creepage, while

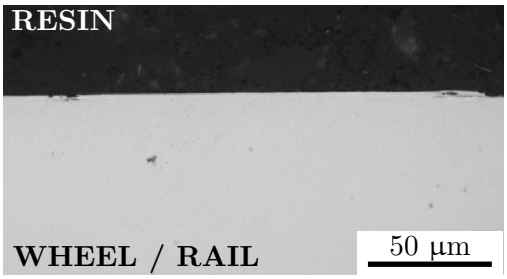

(a) Unused disc as baseline, results are similar for wheel and rail disc

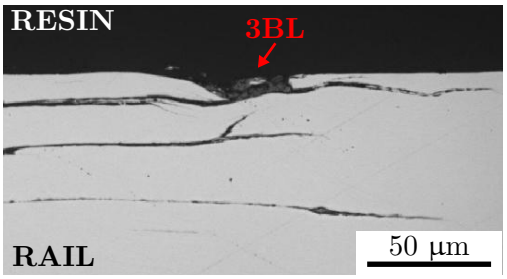

(b) Rail disc after testing.

Fig. 3.13: Results of the microscopical investigations. The test parameters were $v = 0.5\ \mathrm{ms}^{-1}$, $p_0 = 0.9$ GPa, $c_x = 5\%$. The surface of the rail discs shows similar results for all test conditions: a flake like structure and cracks, no noteworthy layer

.

it decreases with increasing speed (see Fig. 3.15). However, the number and the depth of the observed cracks increased with increasing speed as shown in Fig. 3.15. Although it was not possible to investigate the exact composition of the layer, the X-Ray Powder Defraction analysis of the wear debris showed that it consists of iron oxides and iron.

In addition, the samples were etched to investigate the subsurface deformations. Severe plastic deformations were observed on the wheel and the rail disc as shown in Fig. 3.16.

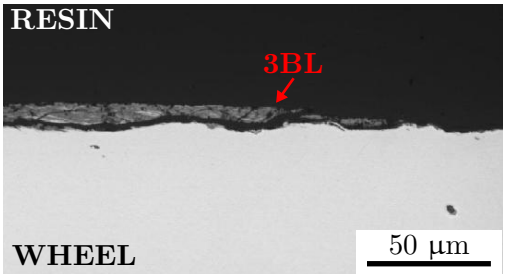

(a) Wheel, $p_0 = 0.9$ GPa, $c_x = 0.2\%$: no continuous layer visible, only flakes

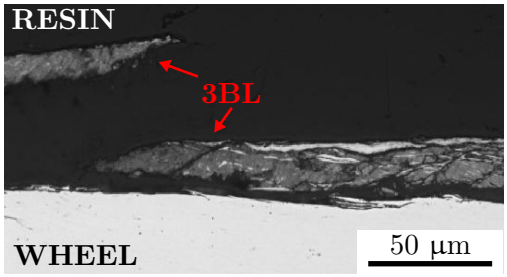

(b) Wheel, $p_0 = 0.9$ GPa, $c_x = 1\%$: layer becomes continuous, thickness increases

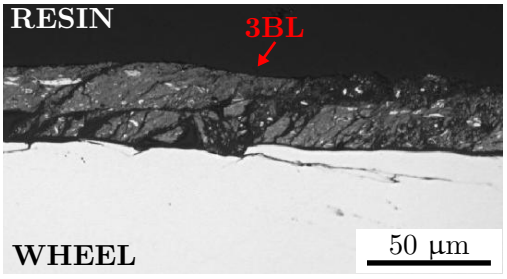

(c) Wheel, $p_0 = 0.9$ GPa, $c_x = 5\%$: covered with an up to 20 µm thick continuous layer of compacted iron and iron oxide particles.

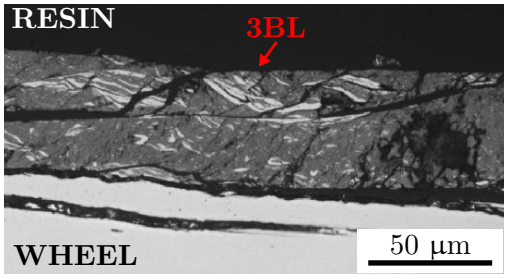

(d) Wheel, $p_0 = 1.5$ GPa, $c_x = 5\%$: thickness of layer increases to 50 µm with increased normal load.

Fig. 3.14: Results of the microscopical investigations. The speed used was $v = 0.5\ \mathrm{ms}^{-1}$. The thickness of the layer increases with normal load and creepage.

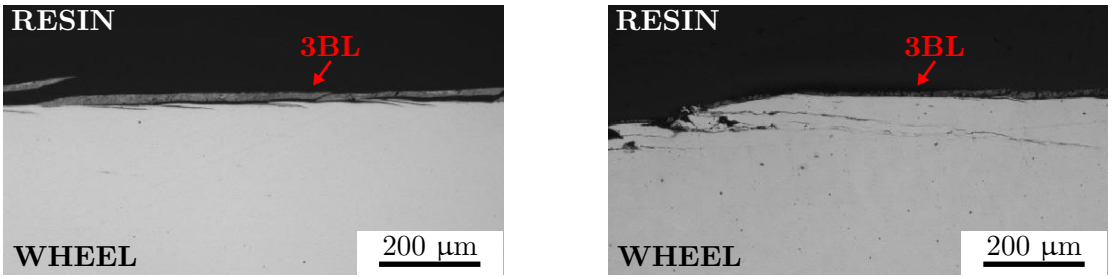

(a) Wheel, $v = 0.5$ ms^{-1} (b) Wheel, $v = 1$ ms^{-1}

Fig. 3.15: Results of the microscopical investigations for $p_0 = 1.5$ GPa, and $c_x = 5\%$. While the thickness of the layer decreases with increasing speed, the number of subsurface cracks increase.

Finally, the measured traction coefficients (f) depending on the longitudinal creepage (c_x) were investigated. Fig. 3.17 shows these traction characteristics for two different normal loads and two different speeds. The results show that an increasing speed leads to a decrease in the traction. This is similar to the results of the vehicle tests, which were discussed in Section 3.1. While it was not possible to vary the normal load in the vehicle tests, this influence could be investigated here. The results show that an increase in the normal load leads also to a decrease in the maximum traction coefficient, which was even more pronounced than the influence of the speed in the investigated cases. This normal load dependency is in contrast to Coulomb's Law, which assumes a constant coefficient of friction independent of the normal load. However, it can also be seen that neither the speed, similar to the results of the vehicle tests (see also Fig. 3.4(b)), nor the normal load seem to significantly change the increase of traction for low creepages ($c_x \lesssim 1\%$).

The normal load dependency was then compared to two different models mentioned in Chapter 2.2: FASTSIM (FS) and Tomberger (TO) model. The Polach model was not chosen for this comparison because the algorithm is formulated for point contact and it was impossible to calculate adequate results for line loading. Also, the speed influence was neglected. Fig. 3.18 shows the comparisons and Tab. 3.3 presents the relative errors for different maximum normal stresses, calculated by Eq. (2.9).

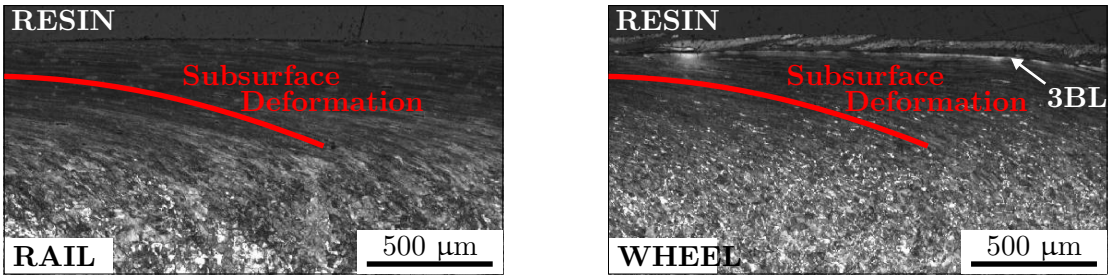

(a) Rail, etched (b) Wheel, etched

Fig. 3.16: Subsurface deformations on the wheel and rail disc.

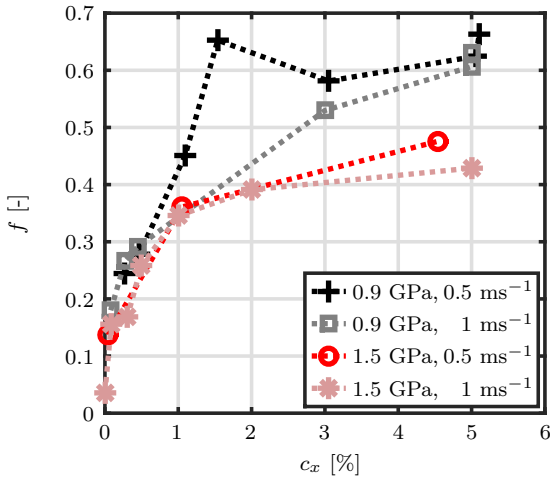

Fig. 3.17: Coefficients of friction measured by the TD tests.

In case of FASTSIM, the coefficient of friction was set to $\mu = 0.6$. For the Tomberger model, the boundary lubrication factor was set to $k_b = 1.3$ and the roughness factor to $k_r = 0.5$. FASTSIM and the Tomberger model show slightly different results depending on the normal load.

FASTSIM yields two different increases in traction for low creepages due to different normal loads because a higher normal load leads to a larger contact area and, thus, to a different stiffness. However, the model is not able to reproduce different maxima depending on the normal load: for $c_x = 5\%$, both scenarios result in the same traction coefficient (see Fig. 3.18(a)). The reason is that FASTSIM relies on Coulomb's Law, where the coefficient of friction is not normal load dependent.

The Tomberger model, on the other hand, uses a sub-model that incorporates the influence

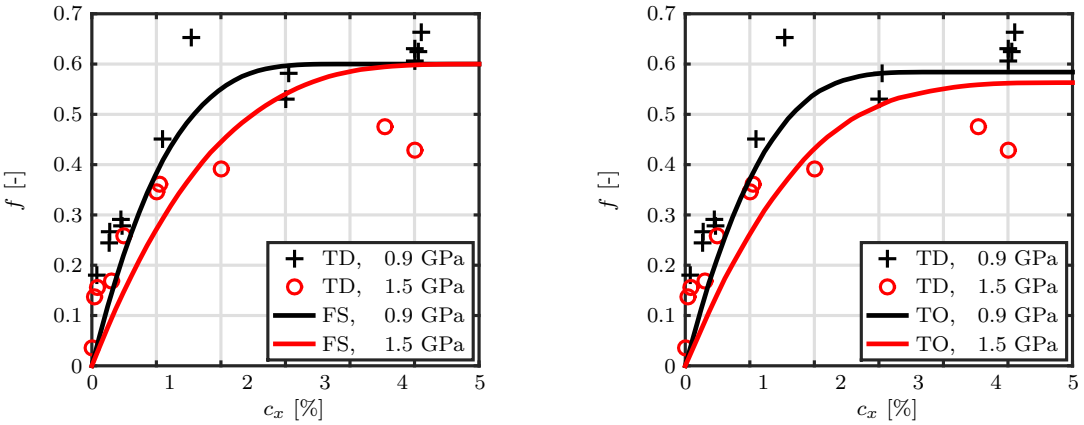

(a) FASTSIM (FS)

(b) Tomberger (TO) model

Fig. 3.18: Comparison of the traction coefficient (f) depending on the longitudinal creepage (c_x) measured on the Twin-Disc (TD) test machine vs. two different models from the literature. The influence of the speed was neglected.

Table 3.3: The relative error as defined by Eq. (2.9) for different models:

Model	0.9 GPa	1.5 GPa	Mean
FASTSIM	19.19%	37.67%	28.43%
Tomberger	20.46%	35.25%	27.85%

of the micro roughness. This influence is depending on the elastic and plastic properties of the asperities. Therefore, the Tomberger model is able to qualitatively, although not quantitatively, reproduce a normal load dependency. As mentioned before in Section 3.1.1, the Tomberger model was parametrized using data from the literature. So, deviations must be expected and further parametrization can improve the quality of the results.

3.3 High Pressure Torsion (HPT) Tests

In Section 3.2, the Twin-Disc tests showed that none of the used models was able to predict the influence of the normal load correctly. FASTSIM relies on Coulomb's Law with a chosen global coefficient of friction (μ), which defines the height of the maximum and does not depend on the normal load. This explains its inability to reproduce the change in the maximum due to different normal loads [18]. The Tomberger model does not use a pre-set coefficient of friction. Instead, it calculates a local coefficient of friction by using sub-models. One of these sub-models takes into account the micro roughness of the surfaces. There, it is assumed that the normal load changes the size of the actual micro contact area due to the elastic-plastic properties of the asperities [37]. While this model was able to qualitatively reproduce the influence of the normal load on the measured traction characteristics, the results did not agree quantitatively. The reason is that the model was parametrized only by using data from literature.

Another reason for a normal load dependency of the traction coefficient is the presence of a compacted granular surface layer, i.e., a solid Third Body Layer (3BL). In Section 3.2, it was shown that the thickness of the 3BL varies with the normal load which can possibly influence the resulting traction. Also, compacted granular materials show a change of their mechanical properties, e.g, the yield stress, due to different normal loads [57–66].

In the past, Pin on disc tests were performed to investigate the influence of different 3BL under high normal load ($p > 0.5$ GPa) on the friction [13]. In addition, it is also possible to use different roughnesses and normal loads. The main benefit of Pin on Disc tests is that these test rigs are easy to built: they have a very small area of contact, which means that low normal loads yield high normal stresses. However, the contact size in such tests is not comparable to the wheel-rail contact. Also, a statistically even distribution of granular materials on the contact surface is more difficult for small areas. Therefore, it is

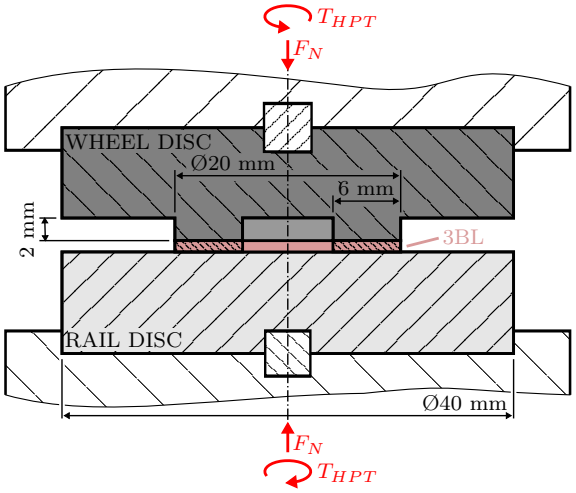

Fig. 3.19: Schematic diagram of the HPT test. T_{HPT} is the measured torque, F_N the applied normal load.

beneficial to investigate the normal load dependencies with a different test where larger contact areas can be realized.

Such a test machine is the High Pressure Torsion (HPT) test machine at the Erich Schmid Institute in Leoben, which is capable of applying a normal load of 264 kN on a contact area of $A \approx 264$ mm^2, thus resulting in a maximum normal stress of $p_0 \approx 1$ GPa. The geometry of the test is depicted in Fig. 3.19. There, two discs are pressed together. Although the two discs were made of the same R8 rail material, the upper disc will be called wheel disc and the lower rail disc. Before testing, both discs were cleaned with acetone. The testing was started by rotating the wheel disc. Then, while it was rotating, the normal load was applied. Although this mode of operation is not a rolling contact, the time the two discs were pressed together was short enough to ensure a resulting displacement that is comparable to the displacements occurring in the actual wheel-rail contact for a certain creepage.

The tests were performed on three different days. The angular velocity (ω) was chosen to be as low as possible to reduce the frictional power generated to maintain near room temperature in the material and, thus, minimizing temperature related effects. This angular velocity was approximately constant for each test: $\omega = 0.015\mathrm{s}^{-1}$. Also, the environmental

Table 3.4: The results for the angular velocity (ω), environmental temperature (T_e), and humidity of air (H_A) measured on the three different days and the calculated mean values.

	Day 1	Day 2	Day 3	Mean
T_e [°C]	24.7	25.1	24.8	24.9
H_A [%]	21	22.1	37.9	27

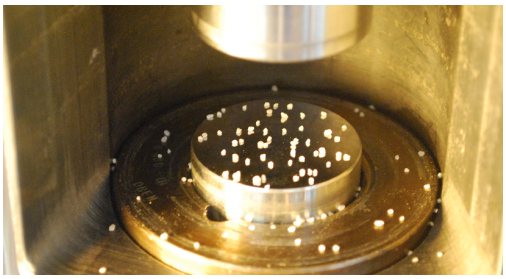

(a) DSL conditions: clean contact area with a few sand grains.

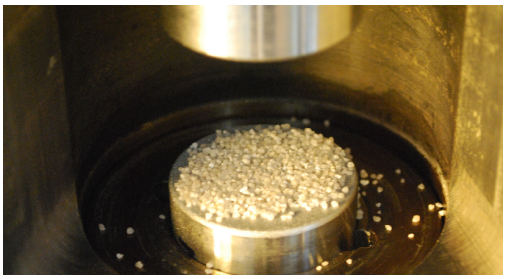

(b) DSH conditions: clean contact area with a continuous layer of sand.

Fig. 3.20: Dry-sanded conditions with (a) low and (b) high amount of sand.

temperature (T_e) and the humidity of air (H_A) were measured during the tests. Tab. 3.4 shows the results of these values for the three different days. To investigate the influence of these factors, certain tests were repeated on each day.

The rotation of the rail disc resulted in a displacement $u(r,t)$, depending on the different radii (r) and different time (t), and a torque $T_{\mathrm{HPT}}(t)$. The mean displacement $\overline{u}(t)$ was calculated using the mean radius of the contact $\overline{r} = 7$ mm:

$$\overline{u}(t) = \omega \overline{r} t \tag{3.13}$$

The resulting shear stress $\tau(t)$ was calculated from the measured torque $T_{\mathrm{HPT}}(t)$:

$$\tau(t) = \frac{T_{\mathrm{HPT}}(t)}{A\ \overline{r}} \tag{3.14}$$

To investigate the influence of the roughness, the surfaces of half of the discs have been polished until the maximum profile height was $R_t < 1$ µm. This will be called smooth surface. The other discs were treated with abrasive blasting, resulting in a maximum height of $R_t \approx 33$ µm, which will be called rough surface. In addition, it was possible to investigate the influence of different contact conditions:

- Dry condition (DC) indicates that no additional substances were added to the contact.
- For wet conditions (WC), 1 ml of water was poured into surface of the rail disc with a syringe. Assuming an evenly distributed water layer on the whole rail disc surface, the thickness of the water layer is approximately 200 µm.
- Dry-sanded with low amount of sand (DSL) indicates a dry contact with a few sand grains brought into the contact area as shown in Fig. 3.20(a).
- Dry-sanded with high amount of sand (DSH) is the same as DSL but instead of a few grains of sand, a continuous layer was added on top of the surface (see Fig. 3.20(b)

- For wet-sanded with low amount of sand (WSL), 1 ml of water was added to the same conditions as DSL.
- Wet-sanded with high amount of sand (WSH) is the same as WSL but with a continuous layer of sand

3.3.1 HPT Results

A typical result of such an HPT test is shown in Fig. 3.21. In this case, discs with a rough surface were used. The tests were done with cyclic loading to simulate the rolling process and to investigate the stability of the results. Here, four cycles were performed. While there are slight deviations from cycle to cycle, the results show an overall stable behaviour. For a better analysis, the mean shear stress $\overline{\tau}$ and the mean normal stress $\overline{p}$ were calculated from those cycles. These can then be plotted in dependency of the mean displacement $\overline{u}$ as shown in Fig. 3.21(b).

The length of a cycle was $\Delta t > 15$ s. According to Eq. (3.13), this results in a mean displacement of $\overline{u}(t) > 1.5$ mm for the given angular velocity and geometry. However, at the beginning of each cycle, it took some time for the normal load to become constant. Then, the normal load was kept constant for a time of $\Delta t > 7$ s which results in a change of displacement of $\Delta\overline{u}(t) > 0.7$ mm. Considering a typical wheel-rail contact length of 14 mm, this correlates to a longitudinal creepage of $c_x > 5\%$. As mentioned above, the angular velocity was kept constant to minimize temperature related effects. In the wheel-rail contact, the surface temperature of the contact area increases with creepage and its influence becomes the dominant influence on the traction coefficient for high creepages,

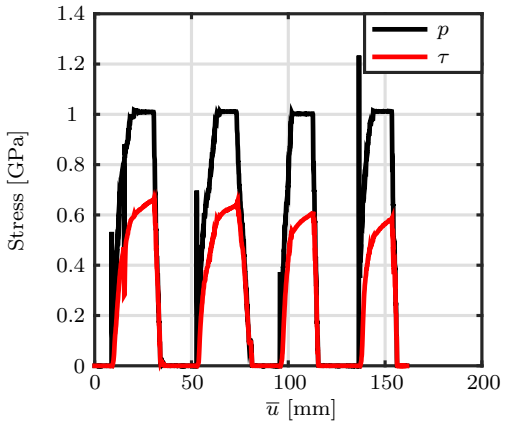

(a) The shear stress (τ) and the normal stress (p) depending on the mean displacement ($\overline{u}$) for four different cycles

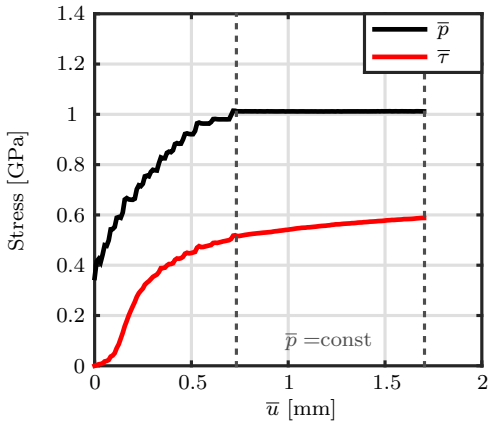

(b) Mean shear stress ($\overline{\tau}$) and mean normal stress ($\overline{p}$) calculated from (a) depending on the mean displacement ($\overline{u}$)

Fig. 3.21: Results of a HPT test with DC and rough surface performed on the first day.

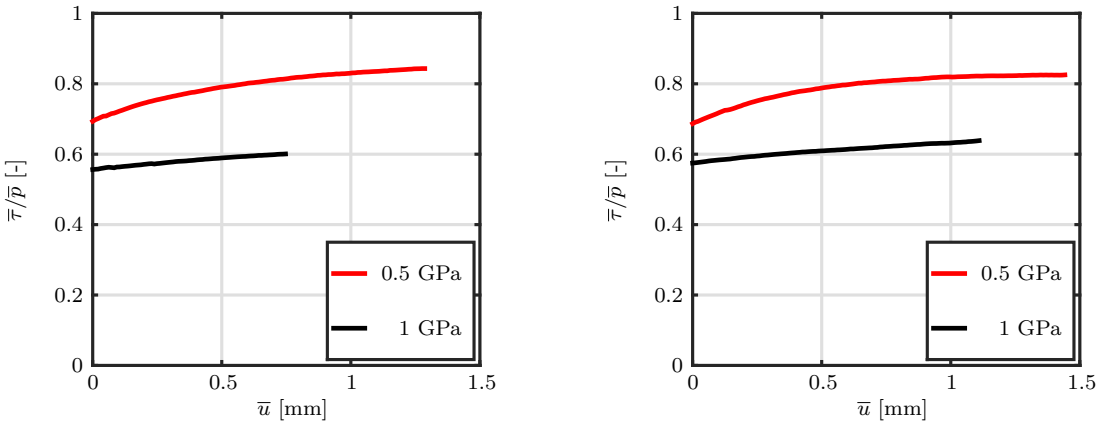

(a) Rough surface

(b) Smooth surface

Fig. 3.22: The mean shear stress ($\overline{\tau}$) divided by the mean normal stress ($\overline{p}$) depending on the mean displacement ($\overline{u}$) for two different maximum normal stresses on the first day and for two different surface roughnesses. The shown frictional behaviour does not obey Coulombs Law.

especially for $c_x > 5\%$ [37, 67]. Thus, it was not deemed necessary to measure the behaviour of the friction for displacements much higher than $\Delta\overline{u}(t) \approx 0.7$ mm. In the following investigations of this section, only the results for constant normal load are discussed.

One important parameter that was investigated, was the influence of the maximum normal load. Fig. 3.22 shows some chosen results of this investigation for two different surface roughnesses. According to the test results, the dependency of the tangential stress on the normal stress does not obey Coulomb's Law: the ratio of the mean shear stress divided by the mean normal stress is not constant, instead it is higher for a lower normal load. This effect is similar to the behaviour of granular materials [57–66]. In addition, the mean shear

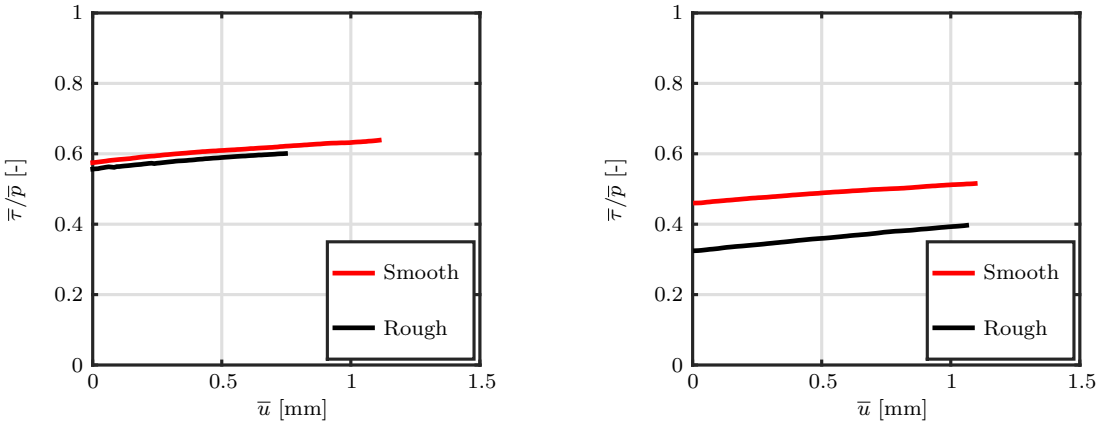

(a) Results for different surface roughnesses on the first day.

(b) Results for different surface roughnesses on the second day.

Fig. 3.23: Results for the HPT tests on two different days with different surface roughnesses under DC. The normal stress was $p = 1$ GPa.

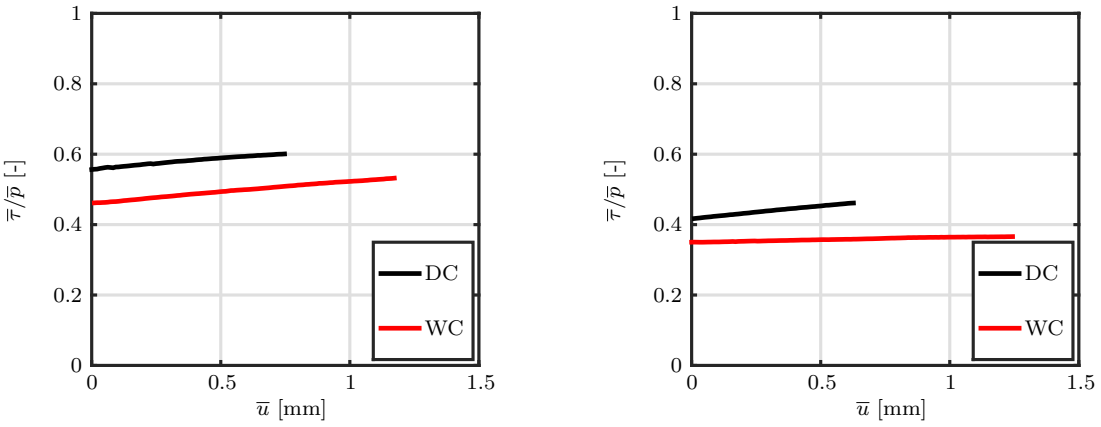

(a) First day

(b) Third day

Fig. 3.24: Results for the HPT tests on two different days for rough surfaces with DC and WC. The normal stress was $p = 1$ GPa.

stress increases with the displacement, comparable to strain-hardening effects observed in solids. Also worth noting is the fact that the hardening becomes less pronounced for higher displacements, especially for $\overline{p} = 500$ Mpa.

The surface roughness dependency is investigated more closely in Fig. 3.23. There, the results of the HPT tests for different roughnesses on different days with DC is shown. First, it must be noted that all the results show a strain-hardening similar to Fig. 3.22. In addition, it can be seen that the overall level of friction is lower on the second day. It must be added that the reason for the different levels of traction on the different days was not due to a different humidity of air or a change of the environmental temperature because they were nearly the same as shown in Tab. 3.4. Also, the results show that the discs with the smooth surface produce higher friction. However, the difference in the results between the first and the second day is larger than the difference between rough and smooth surface. Hence, it can be concluded that the influence of the surface roughness not significant.

Fig. 3.24 shows the influence of water in the contact. The tests were performed on the first and the last day with rough surfaces. Comparing the two days, it can be seen that the first day shows an overall higher level of friction for both conditions. However, there is a qualitative agreement: the results for WC are lower than for DC. This seems to be in accordance with the results of the vehicle tests, which showed lower maxima for WC (see also Fig. 3.7). Also, the strain-hardening is less pronounced for WC on the third day.

Next, different contact conditions were investigated. Especially sanded conditions were of great interest. The results for DSH and DSL for two different surface roughnesses is compared to the results of DC in Fig. 3.25. All of them were from the same day. For rough surfaces, the level of friction is higher for DSL than DSH. This is contrary to the results for smooth surfaces, where the DSH shows a higher frictional level than the DSL. It is worth noting that the results for high sanding are closer to dry contact conditions

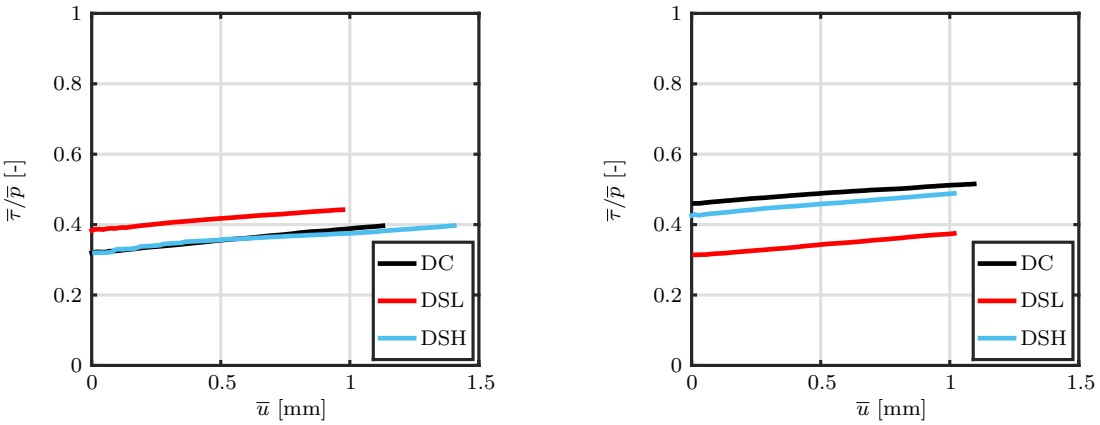

(a) Rough surface (b) Smooth surface

Fig. 3.25: Results for the HPT tests on the second day with different surface roughnesses for DSL and DSH. The normal stress was $p = 1$ GPa.

than the results for low sanding. Another interesting feature of Fig. 3.25 is, again, the strain-hardening-like increase of friction for high displacements.

Finally, a comparison of the results for DC to WSL and WSH conditions for rough surfaces on two different days is shown in Fig. 3.26. These results show a very similar behaviour to dry-sanded conditions: the amount of sand used seems not important and the level of friction seems comparable to the dry results. When comparing these results to the results for WC in Fig. 3.24, the conclusion can be drawn that sanding under wet condition increases the level of friction to the same level as it was for dry conditions. Also worth noting is the fact that both tests under wet-sanded conditions show less strain-hardening than during dry conditions on the third day. However, the overall traction level was in a similar range, especially when comparing dry conditions.

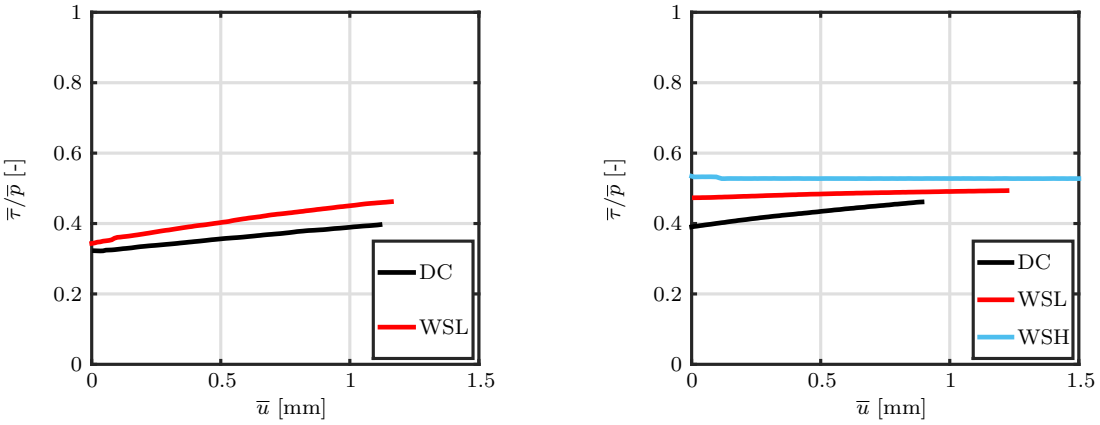

(a) Second day (b) Third day

Fig. 3.26: Results for the HPT tests on two different days with rough surfaces for DC, WSL, and WSH. The normal stress was $p = 1$ GPa.

All of these results of the HTP tests, i.e., the normal load dependency, the strain-hardening, and the influence of different contact conditions, are used as a basis for a new creep force model that will be developed in the next chapter.

4 The Extended Creepforce (ECF) Model

As mentioned in Chapter 3, the existing models were neither able to reproduce the results from the vehicle tests nor the Twin-Disc tests. Thus, a new creep force model was developed in this work that is able to reproduce all of the following effects:

- A steep increase of the traction coefficient for low creepages
- A moderate increase in traction for medium creepages
- A traction loss for high creepages
- A velocity dependency of the traction level of the characteristic
- A shift of the maximum traction to lower creepages for higher velocities
- An influence of different contact conditions on the traction
- A normal load dependency of the traction level

The core of this new model is a Third Body Layer (3BL) sub-model which is developed in Section 4.1. The wheel and the rail are considered to be homogeneous, isotropic, and ideally elastic. As shown in Fig. 4.1, the 3BL consists of fluids and solid particles in between wheel and rail, as well as the surface layers of wheel and rail, including asperities and micro-cracks

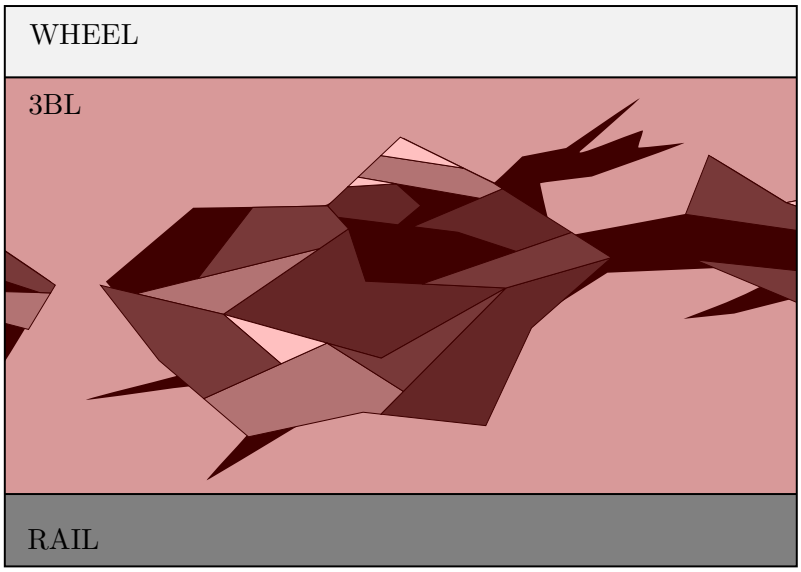

Fig. 4.1: Idea of the 3BL sub-model: the 3BL (red) consists of granular particles and micro-cracks.

with a depth in the order of micrometers. While the layer is obviously inhomogeneous and anisotropic on a microscopical level, it is approximated by an homogeneous and isotropic material model on a macroscopic level.

The main innovation of this new model is the implementation of an elasto-plastic material law, depending on the normal stress distribution and the local temperature, to describe the behaviour of the 3BL. Thus, effects observed during the HPT tests can be replicated. The normal stress distribution is assumed to be Hertzian (see Section 2.1). The local temperature depends on the strains and is calculated by an additional sub-model which is presented in Section 4.2. All sub-models are formulated to include a full time dependency in order to reproduce transient effects. The final algorithm will be presented as a whole in Section 4.3. Also, some possible future additions to the model are discussed there.

Then, the ECF model will be subject to a closer investigation. The influence of the parameters used on the traction will be shown on a local and global scale for scenarios where the forces and creepages are quasi-steady in Section 4.4 or for a rapidly changing creepage in Section 4.5.

4.1 The time-dependent 3BL Sub-Model

In the introduction of Chapter 4 it was mentioned that, microscopically, the 3BL consists of particles in-between the wheel and rail as well as the topmost micrometers of the surface layers of wheel and rail, containing asperities and micro-cracks. Macroscopically, the 3BL is modelled as an isotropic and homogeneous material adhering to both, wheel and rail. The HPT tests presented in Section 3.3 showed effects similar to strain-hardening known from elasto-plastic solids. To reproduce this, an elasto-plastic material behaviour had to be included into the model.

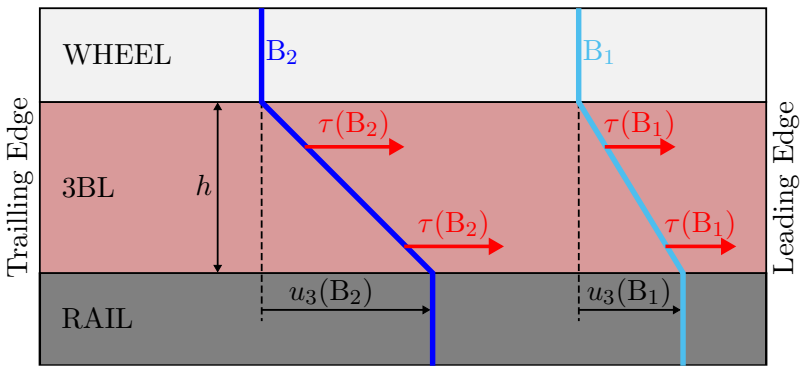

Fig. 4.2: Sketch of the 3BL in-between wheel and rail with two different independent bristles (B_1 and B_2), their relative displacements (u_3) and the stresses acting on each bristle (τ). The displacements and stresses increase as the bristles travel trough the contact.

According to the Twin-Disc tests from Section 3.2, the thickness of the layer (h) is up to 50 µm and, thus, much smaller than the dimensions of the contact, which are in the range of a few millimetres (see also Section 2). As shown in Fig. 4.6, a brush model is used to describe the layer: the 3BL consists of independent bristles normal to the contact plane and the tangential stresses are considered constant along each bristle [68].

In the model, the bristles are linear elastic for tangential stresses ($\underline{\tau} = (\tau_x, \tau_y)$) lower than a first critical shear stress (τ_{c1}). In this case, the resulting displacements of the bristles ($\underline{u_3}$) are calculated by using the inverted stiffness of the 3BL (L_e):

$$\underline{\tau} = \frac{\underline{u_3}}{L_e} \qquad \text{for} \quad |\underline{\tau}| \leq \tau_{c1} \tag{4.1}$$

For higher stresses, a plastic deformation of the bristles is assumed. To describe the resulting stresses, the Voce strain-hardening law was chosen [69]:

$$|\underline{\tau}| = \tau_{c1} + (\tau_{c2} - \tau_{c1}) \left[1 - \exp\left(\frac{-|\underline{u_3}| + \Delta u}{L_p}\right)\right] \qquad \text{for} \quad \tau_{c1} < |\underline{\tau}| < \tau_{c2} \tag{4.2}$$

with the so-called plasticity factor (L_p) and a second critical shear stress ($\tau_{c,2}$), which cannot be exceeded due to the exponential nature of this law. Here, $\Delta u = \tau_{c1} L_e$, which is the necessary shift to ensure a continuous transition from elastic to plastic behaviour.

The resulting tangential stresses are now depending on four parameters (L_e, L_p, τ_{c1}, and τ_{c2}) which are describing the elasto-plastic material behaviour of the independent bristles. A qualitative sketch of their influence is shown in Fig. 4.3. The value of L_e influences the initial gradient for stresses lower than τ_{c1}, while L_p influences the shape of the strain-hardening for stresses between τ_{c1} and τ_{c2}.

In Section 3.3, the HPT tests showed a normal stress dependency of the tangential stresses

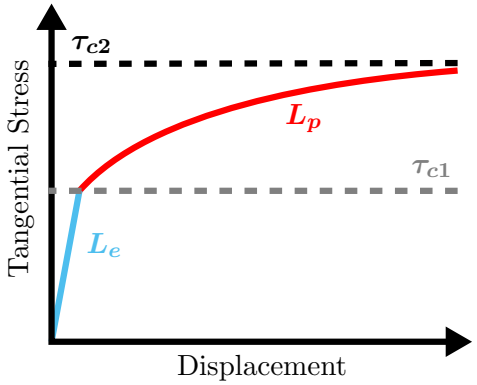

Fig. 4.3: Areas of influence of the four material parameters: L_e is the inverted elastic stiffness. For stresses higher than τ_{c1}, the material behaviour changes from elastic to plastic described by L_p. The maximum stress is τ_{c2} which can never be exceeded.

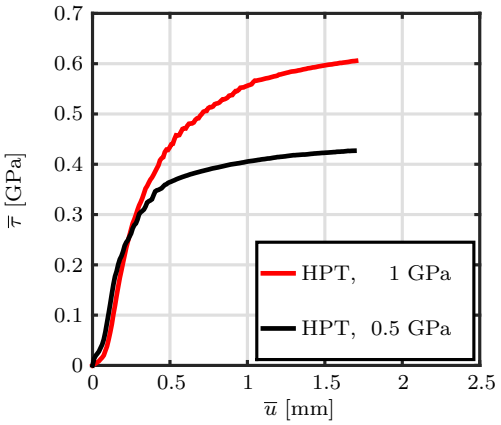

(a) Result of HPT test for two different normal stresses (see also Section 3.3).

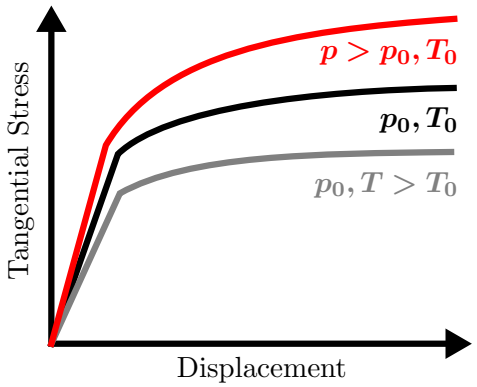

(b) Idea for the influence of normal stress (p) and temperature (T) in the 3BL sub-model.

Fig. 4.4: Comparison of the HPT test results and a sketch of the idea to describe the influence of normal stress and temperature on the material properties in the 3BL sub-model.

similar to the behaviour of granular materials. There, the shear resistance increases with increasing normal stress while also depending on the properties of the particles. These become softer with increasing temperatures, thus reducing the resulting shear stresses [57–66].

To account for these effects, the next logical step in the development of the 3BL sub-model was the introduction of a normal stress and temperature dependency for the four material parameters describing the elasto-plastic behaviour. Eventual gradients along each bristle are neglected due the dimensions of the layer. Fig. 4.4 shows a sketch of this idea compared to results from the HPT tests.

A similar approach was also featured in the Tomberger model [37]. There, complicated sub-models are responsible for the reproduction of this behaviour. Here, simple exponential laws are used to describe this temperature (T) and normal stress (p) dependency of the material parameters. For the critical shear stresses, these laws are:

$$\begin{aligned} \tau_{c1}(p,T) &= \tau_{c1}^0 \left[1 - \exp\left(-p\tau_{c1}^p\right)\right] \left[\exp\left(-\left(T - T_0\right)\tau_{c1}^T\right)\right] \\ \tau_{c2}(p,T) &= \tau_{c2}^0 \left[1 - \exp\left(-p\tau_{c2}^p\right)\right] \left[\exp\left(-\left(T - T_0\right)\tau_{c2}^T\right)\right] \end{aligned} \tag{4.3}$$

where T_0 is room temperature and τ_{c1}^0, τ_{c1}^p, τ_{c1}^T, τ_{c2}^0, τ_{c2}^p, and τ_{c2}^T are constants. While τ_{c1}^p and τ_{c2}^p modify the influence of the normal load on these stresses, τ_{c1}^T and τ_{c2}^T describe the influence of the temperature. For a lower normal load, the 3BL is less compressed and the asperities and the granular particles are less entangled, leading to a decrease of cohesion [57–66]. The functions ensure that the resulting critical shear stresses (τ_{c1} and τ_{c2}) decrease with decreasing normal load and, thus, are always lower than τ_{c1}^0 and τ_{c2}^0. The same is true for an increase of the temperature, were the material also becomes less

cohesive and a reduction of the two critical shear stresses is expected [70]. Therefore, τ_{c1}^0 can be interpreted as maximum of the yield stress and τ_{c2}^0 as the maximum shear strength of the 3BL.

Similar functions are assumed for the inverted elastic stiffness ($L_e(p,T)$) and the plasticity factor ($L_p(p,T)$):

$$\begin{aligned} L_\mathrm{e}(p,T) &= L_\mathrm{e}^0 \left[1-\exp\left(-pL_\mathrm{e}^p\right)\right]^{-1} \left[\exp\left(-\left(T-T_0\right)L_\mathrm{e}^T\right)\right]^{-1} \\ L_\mathrm{p}(p,T) &= L_\mathrm{p}^0 \left[1-\exp\left(-pL_\mathrm{p}^p\right)\right]^{-1} \left[\exp\left(-\left(T-T_0\right)L_\mathrm{p}^T\right)\right]^{-1} \end{aligned} \tag{4.4}$$

Again, T_0 is room temperature and L_e^0, L_e^p, L_e^T, L_p^0, L_p^p, and L_p^T are constants. Also, L_e^p and L_p^p are connected to the influence of the normal load, while L_e^T and L_p^T describe the temperature influence. Because a higher inverted elastic stiffness and a higher plasticity factor describe a less cohesive material, L_e and L_p increase for a decreasing normal load and increase with temperature. Thus, L_e^0 is the minimum inverted stiffness and L_p^0 the minimum plasticity factor of the 3BL.

The occurring twelve constants (L_e^0, L_e^p, L_e^T, L_p^0, L_p^p, L_p^T, τ_{c1}^0, τ_{c1}^p, τ_{c1}^T, τ_{c2}^0, τ_{c2}^p, and τ_{c2}^T) are not purely mathematical fit parameters, but have a measurable interpretation. Thus, their values can be identified by tests: while L_e^0, L_e^p, L_p^0, L_p^p, τ_{c1}^0, τ_{c1}^p, τ_{c2}^0, and τ_{c2}^p will be parametrized directly by HPT tests, L_e^T, L_p^T, τ_{c1}^T, and τ_{c2}^T are parametrized indirectly by vehicle tests.

While traversing the wheel-rail contact, each bristle experiences different normal stresses and temperatures over time. The parameters describing the elasto-plasticity change accordingly, which was necessary to consider in the 3BL sub-model.

At the time $t = t_0$, the displacement of a bristle is $\underline{u_3}(t_0)$ and the tangential stress is $\underline{\tau}(t_0)$. It is assumed that the normal stress acting on each bristle and its temperature are constant for a given time interval:

$$\begin{aligned} p(t) &= p(t_1) \\ T(t) &= T(t_1) \end{aligned} \quad \text{for} \quad t_0 < t \leq t_1 \tag{4.5}$$

The resulting material parameters are also constant during this time step:

$$\begin{aligned} L_e(p(t),T(t)) &= L_e(t_1) \\ L_p(p(t),T(t)) &= L_p(t_1) \\ \tau_{c1}(p(t),T(t)) &= \tau_{c1}(t_1) \\ \tau_{c2}(p(t),T(t)) &= \tau_{c1}(t_1) \end{aligned} \quad \text{for} \quad t_0 < t \leq t_1 \tag{4.6}$$

Depending on $\underline{u_3}(t_1)$, the resulting tangential stress $\underline{\tau}(t_1)$ can now be calculated, using Eq. (4.1) - Eq. (4.4).

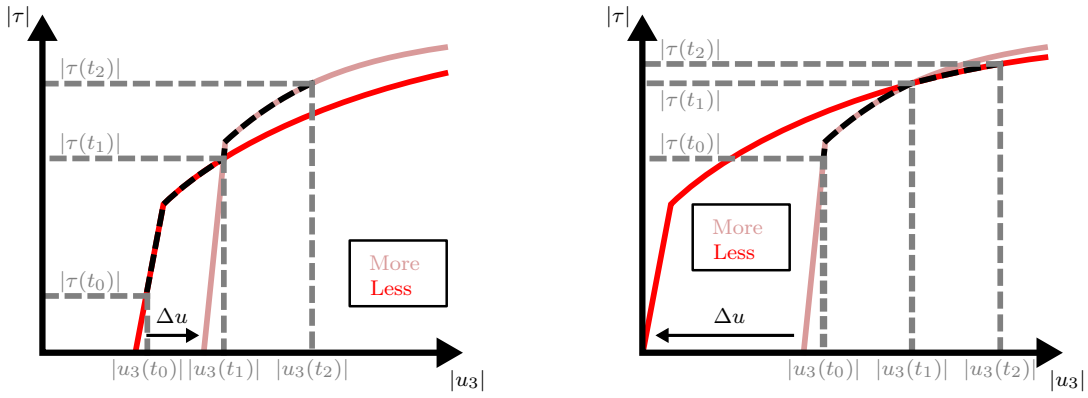

(a) Transition from less to more cohesion.

(b) Transition from more to less cohesion.

Fig. 4.5: Sketch of the tangential stresses used in the 3BL sub-model during changes in cohesion due to different normal stresses or temperatures.

For $t_1 < t \leq t_2$, the normal stress and the temperature increase or decrease ($p(t_2) \neq p(t_1)$ and $T(t_2) \neq T(t_1)$), resulting in a different cohesion of the 3BL. In the model, it was assumed that the stresses and the displacements are continuous despite the changed elasto-plastic behaviour of the bristles. Therefore, the new stress-displacement characteristic is shifted by Δu to intersect at $(u_3(t_1), \tau(t_1))$ as shown in Fig. 4.5. This is then used to calculate $\underline{\tau}(t_2)$ depending on $\underline{u_3}(t_2)$.

It must be added that if a transition from more to less coherent material occurs, it is possible that $\tau_{c2}(t_2) \leq |\underline{\tau}(t_1)|$. Then, it is impossible to find a Δu to intersect the two characteristics. In this case, the cohesion of the layer is not strong enough to withstand the tangential stresses, resulting in breaking and sliding processes. To describe this behaviour, the tangential stresses in the bristle must be reduced:

$$|\tau(t)| = \tau_{c2}(t_2) \quad \text{for} \quad t_1 < t \leq t_2 \quad \text{if} \quad \tau_{c2}(t_2) \leq |\underline{\tau}(t_1)| \tag{4.7}$$

In contrast to Coulomb's law, which is widely used in creep force models as mentioned in Section 2.2, the layer still adheres to wheel and rail: the sliding process occurs within the layer. Also, second critical shear stress (τ_{c2}) is not directly proportional to the normal stress but instead calculated by Eq. (4.3) from the temperature and the normal stress acting on a bristle at a certain time.

As mentioned before and shown in Fig. 4.6, the 3BL is attached to the wheel but adheres to both, wheel and rail. Thus, the total displacement of a bristle ($\underline{u}$) at a given time (t) is the sum of the displacement of the wheel ($\underline{u_w}$), the rail ($\underline{u_r}$) and the 3BL ($\underline{u_3}$):

$$\underline{u}(t) = \underline{u_w}(t) + \underline{u_3}(t) - \underline{u_r}(t) \tag{4.8}$$

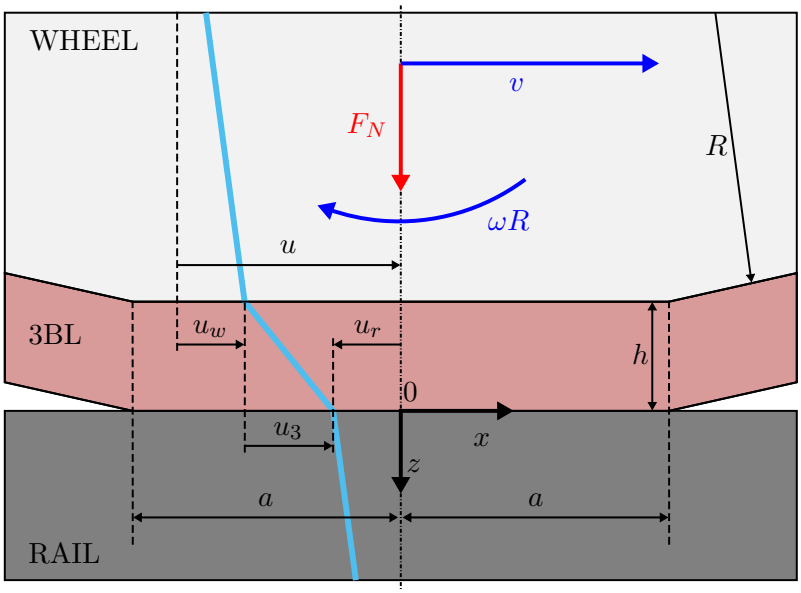

Fig. 4.6: Sketch of the wheel-rail contact.

and can be determined by solving the kinematic relation:

$$\frac{\mathrm{d}\underline{u}}{\mathrm{d}t} = \underline{v_\omega} + \underline{\omega} \times \left[\underline{r_B} - \underline{r_\omega}\right] \tag{4.9}$$

where $\underline{\omega}$ is the angular velocity of the wheel, $\underline{r_B}$ is the location of the bristle, and $\underline{r_\omega}$ is the location of the rotational centre of the wheel, which is moving with the velocity $\underline{v_\omega}$.

Now, the coordinate system shown in Fig. 4.6 is introduced: it is fixed on the rail, the z-direction is pointing into the rail and the x-direction points in the direction the vehicle is moving: $\underline{v}(t) = (v(t), 0, 0)$. The displacements in z-direction are very small compared to the radius of the wheel ($u_z \ll R$) and can, thus, be neglected. While $\underline{r_B}$ is constant due the choice of the coordinate system, $\underline{r_\omega}(t)$ is time dependent and moving with $\underline{v_\omega}(t) = (v_{\omega,x}(t), v_{\omega,y}(t), 0)$. For a time $t \geq 0$, the vector $\underline{r}$ is introduced:

$$\underline{r}(t) = \underline{r_B} - \underline{r_\omega}(t) = \begin{pmatrix} x_B - x_\omega - v_{\omega,x}(t)t \\ y_B - y_\omega - v_{\omega,y}(t)t \\ R \end{pmatrix} = \begin{pmatrix} x - v_{\omega,x}(t)t \\ y - v_{\omega,y}(t)t \\ R \end{pmatrix} \tag{4.10}$$

Using Eq. (4.10), Eq. (4.9) for the tangential displacements yields:

$$\frac{\mathrm{d}\underline{u}(t)}{\mathrm{d}t} = \begin{pmatrix} v_{\omega,x}(t) + \omega_y(t)R - \omega_z(t)\left[y - v_{\omega,y}(t)t\right] \\ v_{\omega,y}(t) - \omega_x(t)R + \omega_z(t)\left[x - v_{\omega,x}(t)t\right] \end{pmatrix} \tag{4.11}$$

The longitudinal, lateral and spin creepage (c_x, c_y, and c_s respectively) are now defined as

$$c_x(t) = \frac{v_x(t) + \omega_y(t)R}{v(t)} \quad , \quad c_y(t) = \frac{v_y(t) - \omega_x(t)R}{v(t)} \quad , \quad c_s(t) = \frac{\omega_z(t)}{v(t)} \tag{4.12}$$

with the vehicle speed $v(t)$.

Eq. (4.12) can be used to rewrite Eq. (4.11):

$$\frac{1}{v(t)} \frac{\mathrm{d}\underline{u}(t)}{\mathrm{d}t} = \begin{pmatrix} c_x(t) - c_s(t)\left[y - v_{\omega,y}(t)t\right] \\ c_y(t) + c_s(t)\left[x - v_{\omega,x}(t)t\right] \end{pmatrix} \tag{4.13}$$

The solution of Eq. (4.13) is:

$$\underline{u}(t) = \underline{u}(t_0) + \int_{t_0}^{t} v(t') \begin{pmatrix} c_x(t') - c_s(t')\left[y - v_{\omega,y}(t')t'\right] \\ c_y(t') + c_s(t')\left[x - v_{\omega,x}(t')t'\right] \end{pmatrix} \mathrm{d}t' \tag{4.14}$$

The bristle enters the contact area at the time $t_0 = 0$ and leaves the contact at $t = t_n$. To solve the integral in Eq. (4.14), it is assumed that the velocity and the creepages are constant in a time interval $t_{i-1} < t \leq t_i$ for $i = 1, 2, ..., n$:

$$\begin{gathered} \underline{v}(t) = \underline{v}(t_i) \quad , \quad \underline{v}_\omega(t) = \underline{v}_\omega(t_i) \\ c_x(t) = c_x(t_i) \quad , \quad c_y(t) = c_y(t_i) \quad , \quad c_s(t) = c_s(t_i) \end{gathered} \tag{4.15}$$

This yields the time-discrete solution of the kinematic relation:

$$\underline{u}(t_i) = u(t_{i-1}) + v(t_i)\Delta t_i \begin{pmatrix} c_x(t_i) - c_s(t_i)\left[y - v_{\omega,y}(t_i)\dfrac{t_{i-1} + t_i}{2}\right] \\ c_y(t_i) + c_s(t_i)\left[x - v_{\omega,x}(t_i)\dfrac{t_{i-1} + t_i}{2}\right] \end{pmatrix} \tag{4.16}$$

with the initial condition:

$$\underline{u}(t_0 = 0) = \underline{0} \tag{4.17}$$

As mentioned at the beginning of this chapter, the 3BL deforms plastically for stresses in between the first and the second critical shear stress ($\tau_{c1} < |\underline{\tau}| < \tau_{c2}$). In this case, the displacements in the layer are much larger than the elastic deformations of wheel and rail:

$$|\underline{u}_w| + |\underline{u}_r| \ll |\underline{u}_3| \tag{4.18}$$

Then, u_r and u_w can be neglected in Eq. (4.8). Using Eq. (4.16), it is possible to rewrite Eq. (4.2) for $\tau_{c1}(t_i) < |\underline{\tau}(t_i)| < \tau_{c2}(t_i)$

$$|\underline{\tau}(t_i)| = \tau_{c1}(t_i) + (\tau_{c2}(t_i) - \tau_{c1}(t_i)) \left[1 - \exp\left(\frac{-|\underline{u}(t_i)| - \Delta u(t_i)}{L_p(t_i)}\right)\right] \tag{4.19}$$

where Δu is the necessary shift in order to intersect the current stress-displacement characteristic with the former at $(\underline{u}(t_{i-1}), \underline{\tau}(t_{i-1}))$ as also shown in Fig. 4.5.

If the resulting stress is smaller than the first critical shear stress ($|\underline{\tau}| \leq \tau_{c1}$), the 3BL exhibits a linear elastic behaviour. Assuming a fully elastic wheel and rail consisting of similar materials, which can be described by the same shear modulus and Poisson ratio, their respective displacements are:

$$\underline{u}_w(t) = -\underline{u}_r(t) \tag{4.20}$$

To describe their elastic behaviour, the Kalker stiffnesses (L_x, L_y, and L_s) from Kalker's simplified theory are used [28]. These are inserted in Eq. (4.16) and together withEq. (4.1), the tangential stresses can be calculated for $|\underline{\tau}| < \tau_{c1}$:

$$\underline{\tau}(t_i) = \underline{\tau}(t_{i-1}) + v(t_i)\Delta t_i \begin{pmatrix} \dfrac{c_x(t_i)}{L_x + L_e(t_i)} - \dfrac{c_s(t_i)}{L_s + L_e(t_i)} \left[y - v_{\omega,y}(t_i) \dfrac{t_{i-1} + t_i}{2} \right] \\ \dfrac{c_y(t_i)}{L_y + L_e(t_i)} + \dfrac{c_s(t_i)}{L_s + L_e(t_i)} \left[x - v_{\omega,x}(t_i) \dfrac{t_{i-1} + t_i}{2} \right] \end{pmatrix} \tag{4.21}$$

4.2 The time-dependent Temperature Sub-Model

In Section 4.1, it was mentioned that the material properties of the 3BL depend on the temperature of a bristle (see Eq. (4.3) and Eq. (4.4)). The thickness of the layer was up to 50 µm and it consists of iron and iron oxides according to the Twin-Disc tests presented in Section 3.2. Due to its dimension and the thermal conductivity of the materials involved, it is assumed that the temperature (T) is constant along each bristle. In addition, it is assumed that the frictional power density ($\dot{q}$) at a given time (t) is proportional to the work used for the plastic deformation:

$$\dot{q}(t) = k_q \frac{\mathrm{d}w_p(t)}{\mathrm{d}t} \quad \text{with} \quad 0 \leq k_q \leq 1 \tag{4.22}$$

Here, w_p is the plastic work density, which is the work per area used to plastically deform the material and $0 \leq k_q \leq 1$ is the dissipation coefficient. The plastic work density can be calculated using the total work density (w_t) and the elastic work density (w_e):

$$w_p(t) = w_t(t) - w_e(t) \tag{4.23}$$

The total work density (w_t) is the integral of the tangential stress ($\underline{\tau}$) over the displacement ($\underline{u}$):

$$w_t(t) = \int_{t_0}^{t} \underline{\tau}(t') \, \frac{\mathrm{d}\underline{u}(t')}{\mathrm{d}t} \, \mathrm{d}t' \tag{4.24}$$

Using Eq. (4.13) Eq. (4.24) can be rewritten as:

$$w_t(t) = v \int_{t_0}^{t} \underline{\tau}(t') \begin{pmatrix} c_x(t') - c_s(t') \left[y - v_{\omega,y}(t')t' \right] \\ c_y(t') + c_s(t') \left[x - v_{\omega,x}(t')t' \right] \end{pmatrix} \mathrm{d}t' \tag{4.25}$$

Similarly to Eq. (4.24), the elastic work density (w_e) can be expressed as follows:

$$w_e(x, y, t) = \int_{t_0}^{t} \underline{\tau}(t') \, \frac{\mathrm{d}\underline{u}_e(t')}{\mathrm{d}t} \, \mathrm{d}t' \tag{4.26}$$

To calculate the elastic displacement ($\underline{u}_e$), the approach presented by Tomberger et al. is followed [71]. There, a generalized elastic stiffness ($\underline{L}^g = (L_x^g, L_y^g)$) is introduced to calculate $\underline{u}_e$ from the tangential stresses ($\tau = (\tau_x, \tau_y)$) :

$$\underline{u}_e(t) = \begin{pmatrix} L_x^g \, \tau_x(t) \\ L_y^g \, \tau_y(t) \end{pmatrix} \tag{4.27}$$

This stiffness is derived by solving the following equations (see also Eq. (4.14)):

$$\begin{aligned} &\int_{t_0}^{t} \left(v(t') \frac{c_x(t') - c_s(t') \left[y - v_{\omega,y}(t')t' \right]}{L_x^g(t')} \right) \mathrm{d}t' \\ &\qquad = \int_{t_0}^{t} \left(v(t') \frac{c_x(t')}{L_x + L_e(t')} - \frac{c_s(t') \left[y - v_{\omega,y}(t')t' \right]}{L_s + L_e(t')} \right) \mathrm{d}t \\ &\int_{t_0}^{t} \left(v(t') \frac{c_y(t') + c_s(t') \left[x - v_{\omega,x}(t')t' \right]}{L_y^g(t')} \right) \mathrm{d}t' \\ &\qquad = \int_{t_0}^{t} \left(v(t') \frac{c_y(t')}{L_y + L_e(t')} + \frac{c_s(t') \left[x - v_{\omega,x}(t')t' \right]}{L_s + L_e(t')} \right) \mathrm{d}t \end{aligned} \tag{4.28}$$

Inserting Eq. (4.24), Eq. (4.26), and Eq. (4.23) into Eq. (4.22) results in:

$$\dot{q}(t) = k_q \, \underline{\tau}(t) \left[\frac{\partial \underline{u}(t)}{\partial t} - \frac{\partial \underline{u}_e(t)}{\partial t} \right] \tag{4.29}$$

For $k_q = 1$, this is the same expression for the frictional power that has been used before [37]. Therefore, the same argument used by Tomberger et al. is also valid in this case: The amount of energy that is stored in structural deformation, e.g., generation of dislocations, creation of debris and cracks, is negligible compared to the amount of heat that is created during frictional contact. However, for future investigations it might be of interested to investigate this more closely and adjust k_q accordingly.

As mentioned at the beginning of the section, eventual gradients of the temperature along each bristle are neglected. Hence, the temperature on the surface of the wheel and the rail

are the same. However, due to different materials and different velocities, the heat flow is different for both. Therefore, the heat partitioning factor (α) is introduced which depends on the vehicle velocity (v) and the circumferential velocity of the wheel (v_w) [67]:

$$\alpha = \frac{\sqrt{v_w}}{\sqrt{v_w} + \beta\sqrt{v}} \tag{4.30}$$

with

$$\beta = \frac{\lambda_r\sqrt{\kappa_w}}{\lambda_w\sqrt{\kappa_r}} \tag{4.31}$$

where κ is the thermal diffusivity, λ the thermal conductivity and the indices w and r denote wheel and rail respectively. The frictional power density that flows into the wheel ($\dot{q}_w$) and the rail ($\dot{q}_r$) are then

$$\begin{aligned} \dot{q}_w(t) &= \quad \alpha \;\; \dot{q}(t) \\ \dot{q}_r(t) &= (1-\alpha)\; \dot{q}(t) \end{aligned} \tag{4.32}$$

The lateral and longitudinal heat conduction in wheel and rail can be neglected if the Péclet condition is met [37, 67]:

$$a\,(v + v_w) > 20\,(\kappa_r + \kappa_w) \tag{4.33}$$

where a is the semi-axis in x-direction, v_w is the circumferential velocity of the wheel, v is the vehicle velocity and κ_w and κ_r are the thermal diffusivity of the wheel and rail respectively. Regarding the wheel-rail contact, the Péclet condition is almost always met for velocities greater than 0.1 ms^{-1}.

Using Eq. (4.32), the temperature (T) on the surface ($z = 0$) due the frictional heating at a given time (t) can be calculated by [67]

$$T(t) = T(t_0) + \frac{\sqrt{\kappa}_w}{\lambda_w\sqrt{\pi}}\int_{t_0}^{t} \dot{q}_w(t')\frac{\mathrm{d}t'}{\sqrt{t-t'}} \tag{4.34}$$

To solve the integral in Eq. (4.34), it is assumed that the frictional power is constant for a given discrete time interval $t_{i-1} < t \leq t_i$ with $i = 1, 2, ..., n$ and $t_0 = 0$. Then, Eq. (4.34) yields [67]

$$\begin{aligned} T(t_n) = T(t_0) + \frac{2\sqrt{\kappa}_w}{\lambda_w\sqrt{\pi}} \Bigg[& \dot{q}_w(t_n)\sqrt{t_n - t_{n-1}} \\ & + \sum_{i=1}^{n-1} \dot{q}_w(t_i)\left(\sqrt{t_n - t_{i-1}} - \sqrt{t_n - t_i}\right) \Bigg] \end{aligned} \tag{4.35}$$

with the initial condition that the temperature of the bristle at t_0 equals the bulk temperature: $T(t_0) = T_B$.

4.3 The Algorithm

The final ECF model consists of the 3BL sub-model and the Temperature sub-model. After the prescription of the input parameters, the actual algorithm starts by solving the 3Bl sub-model. The stiffnesses used in the 3BL sub-model are normal stress and temperature dependent (see Section 4.1). The normal stress distribution is already given. The end results must not depend on the initial condition, so any initial temperature can be chosen.

Next, the tangential stresses derived from the 3BL sub-model are used in the temeprature sub-model to calculate the frictional power and, thus, the temperature. In the next iteration, the new temperature is then used in the 3BL sub-model. This continues until the change in temperature between two iterations is smaller than a predefined value. Fig. 4.7 gives an overview of the algorithm used in this ECF model.

It has to be mentioned here, that both sub-models yield time dependent solutions. Thus, the resulting algorithm is able to calculate the unsteady state solution, which can have an impact on fast dynamic effects, e.g., drive-train oscillations. In case that all variables describing the state are time invariant, the model provides the steady state solution of the problem.

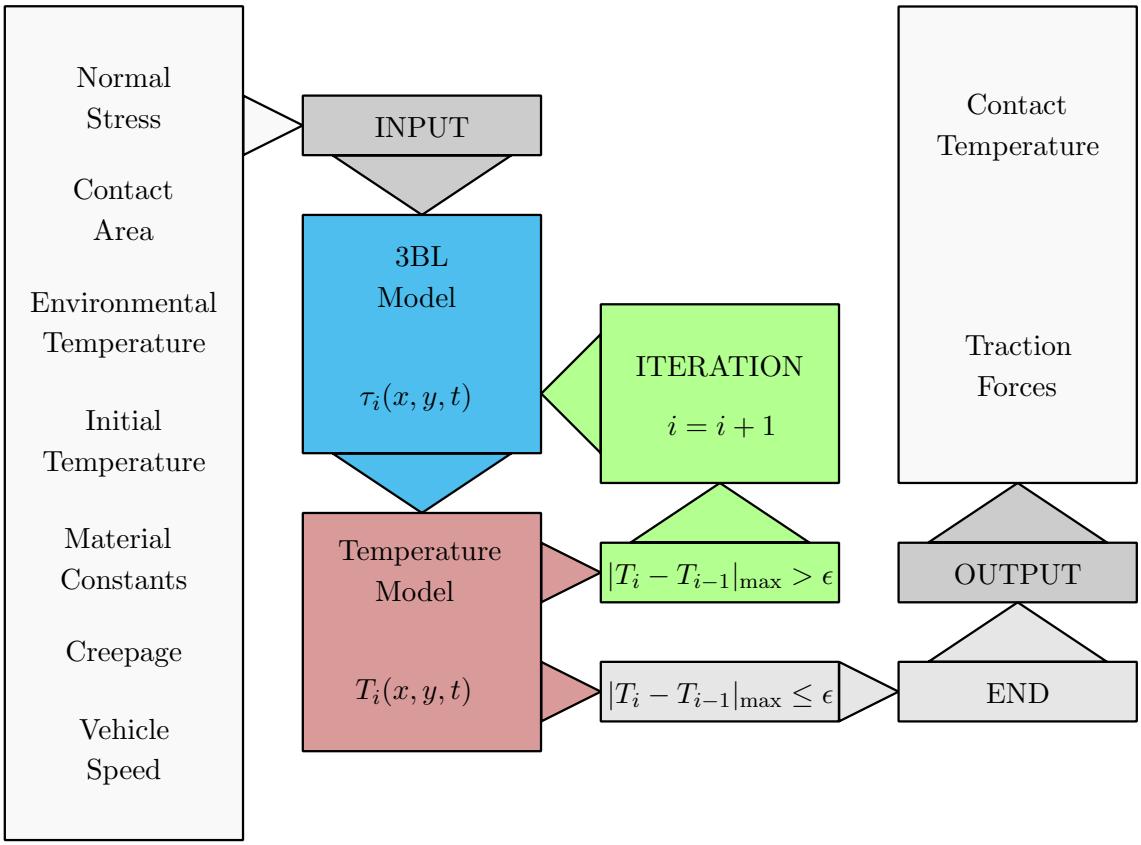

Fig. 4.7: The algorithm of the ECF model.

Investigations regarding the computational effort reveal that using the ECF model needs on average four times more computational effort than using FASTSIM: the ECF model needs approximately four iterations to solve the problem. However, the computational effort of the ECF model is still small enough to be reasonably implemented in Multi Body System software.

Also, due to the modular nature of the ECF model, it is easy to expand the algorithm. While the Hertzian theory is used as default to calculate the normal stress distribution and the contact area, it was possible to incorporate the solution for non-elliptic contacts [32]. Also, a interfacial fluid model [37] could be integrated into the ECF model. However, discussing the effects of these additional sub-models on the results of the ECF model would exceed the scope of this work, so it will not be investigated here and will be a focus of future publications.

4.4 Parameter Study for Quasi-Steady State

The 3BL sub-model and the temperature sub-model are formulated fully time dependent as mentioned in Section 4.1 and Section 4.2. In case that the variables describing the state, e.g. creepage or normal load, are time invariant, the ECF model yields the quasi-steady state solution. These results are now investigated closely.

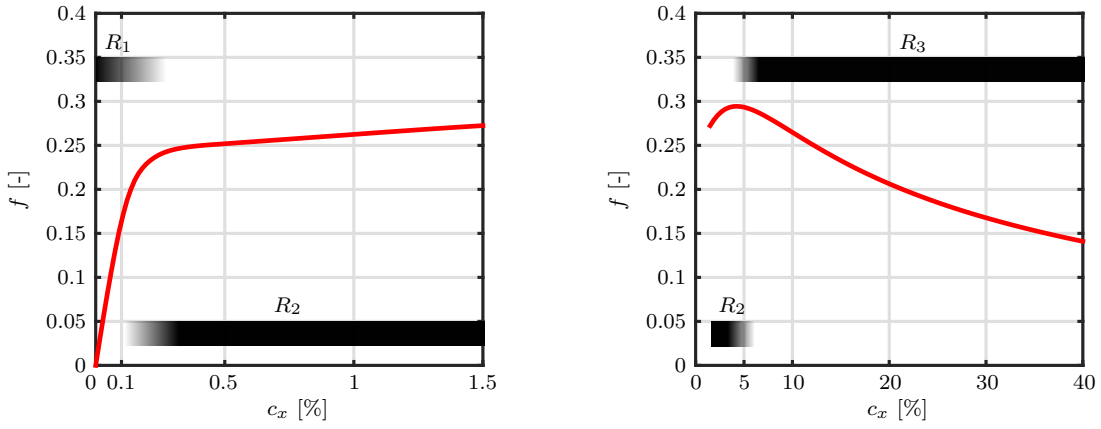

(a) Results for $c_x \leq 1.5\%$.

(b) Results for $1.5\% \leq c_x \leq 40\%$.

Fig. 4.8: Results of the ECF model for the traction coefficient (f) depending on the longitudinal creepage (c_x). The material parameters used are given in Tab. 4.1. Also shown are the three regions (R_1, R_2, and R_3) mentioned in Section 3.1.

Fig. 4.8 shows a typical result of the ECF model for the steady state. The parameters used are given in Tab. 4.1. In addition to the 3BL parameters mentioned in Section 4.1, a normal load of $F_N = 110$ kN and a velocity of $v = 20$ ms^{-1} are used. The half axis of the contact ellipse are $a = 7.63$ mm and $b = 7.88$ mm. These values are taken from a Multi Body Systems simulation of a Vectron locomotive on a straight track. It can be seen that the model produces the three different regimes that were mentioned in Section 3.1: a steep

Table 4.1: Default parameters for steady state investigations.

$L_e^0 = 0.2522 \frac{\mu m}{GPa}$	$L_p^0 = 0.25$ mm	$\tau_{c1}^0 = 0.3$ GPa	$\tau_{c2}^0 = 1.1$ GPa
$L_e^p = \infty \frac{1}{GPa}$	$L_p^p = 1 \frac{1}{GPa}$	$\tau_{c1}^p = 1 \frac{1}{GPa}$	$\tau_{c2}^p = 1 \frac{1}{GPa}$
$L_e^T = 0 \frac{1}{°C}$	$L_p^T = 0.0025 \frac{1}{°C}$	$\tau_{c1}^T = 0.0025 \frac{1}{°C}$	$\tau_{c2}^T = 0.0025 \frac{1}{°C}$
$F_N = 110$ kN	$v = 20$ ms^{-1}	$a = 7.63$ mm	$b = 7.88$ mm

increase of traction for low creepages (R_1), a moderate increase for medium creepages (R_2) and a traction loss for high creepages (R_3).

For a closer investigation of this behaviour, the tangential stress distribution (τ) and the distributions of the two critical shear stresses (τ_{c1} and τ_{c2}) are analysed for four different longitudinal creepages (c_x). The coordinate system is centred in the middle of the contact ellipse at a time $t = t_1$, x and y depict the positions of the bristles. Shown is the cross

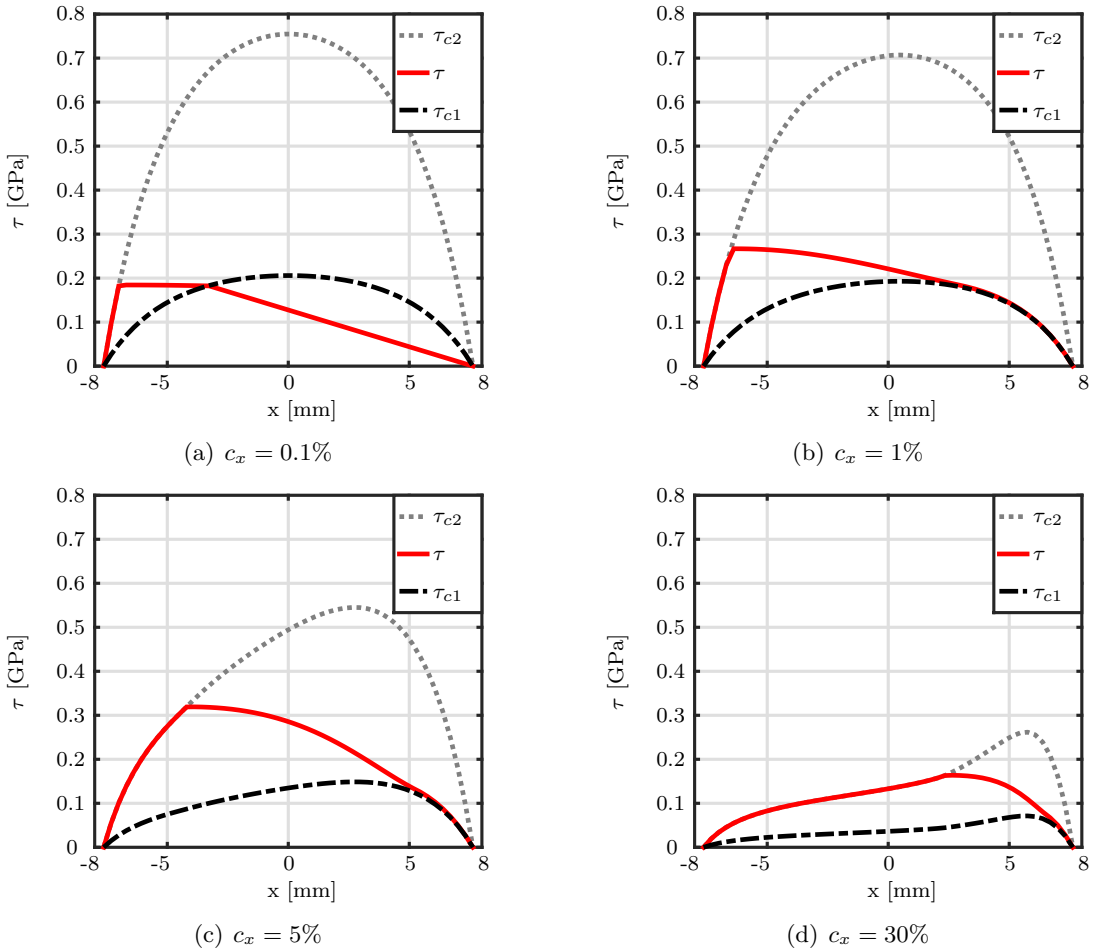

(a) $c_x = 0.1\%$ (b) $c_x = 1\%$

(c) $c_x = 5\%$ (d) $c_x = 30\%$

Fig. 4.9: Results for the local tangential stress ($\tau(x, y = 0)$) and the local critical shear stresses ($\tau_{c1}(x, y = 0)$ and $\tau_{c2}(x, y = 0)$) depending on the longitudinal creepage (c_x).

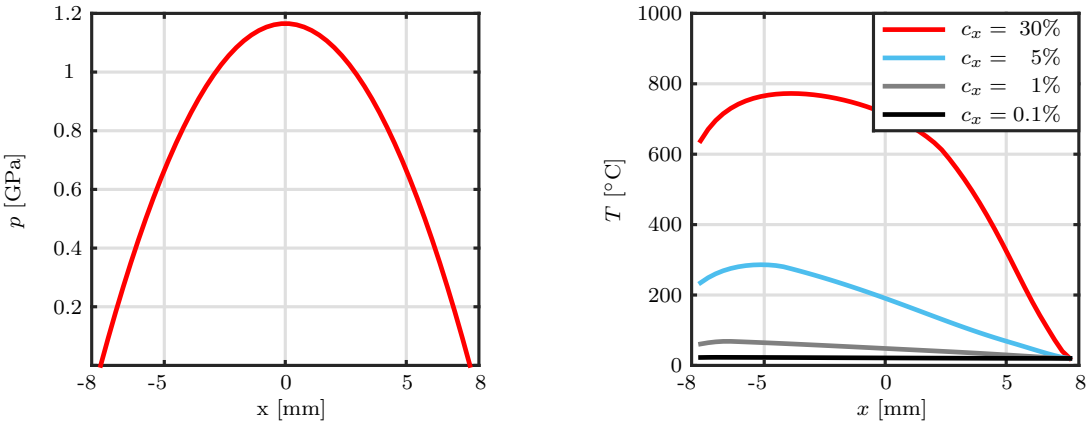

(a) Normal stress distribution (p)

(b) Local temperature (T)

Fig. 4.10: Local normal stress and local temperature distribution for the chosen traction characteristic.

section for $y = 0$.

To show the results for the three different regimes, the creepages were chosen accordingly. The results are shown in Fig. 4.9 for the cross section $y = 0$. The leading edge is on the right side, while the trailing edge is on the left.

The first creepage that was investigated was $c_x = 0.1\%$. This represents the results for the steep increase of traction at low creepages (R_1). Interesting to see in Fig. 4.9(a) is the distribution of the critical shear stresses which depends on the normal load and also on the temperature, although the temperature is very low and has no significant influence at this creepage (see also Fig. 4.10). Here, the tangential stress is dominated by the elasticity of wheel and rail in combination with the elastic behaviour of the 3BL given by Eq. (4.21). This dominant elastic behaviour is responsible for the very steep increase in traction in R_1 (see Fig. 4.8(a)): small changes in the creepage lead to a big change of the area below the tangential stress curve and, thus, to a high change in the tangential force. Only close to the trailing edge, for $x \lesssim -4$ mm, the material shows a strain-hardening effect. There, the tangential stresses are calculated by Eq. (4.19).

Next, the results for $c_x = 1\%$ were investigated in Fig. 4.9(b). It can be seen that elastic-plastic transition now occurs closer to the leading edge. Thus, the 3BL behaves plastically in nearly the whole contact. Increasing the creepage now leads only to a slight increase of the area below the tangential stress. This causes the moderate increase of traction for medium creepages in the second regime (R_2 in Fig. 4.8(a)).

Fig. 4.9(c) shows the result for $c_x = 5\%$, a typical result for a creepage close to the maximum traction, representing the transition between R_2 and R_3. Fig. 4.10(b) shows that the temperature now increases significantly. This leads to a decrease of the values of the critical shear stresses which are now distorted. This reduction counters the increase in traction due to the higher creepage and causes the maximum traction shown in Fig. 4.8(b).

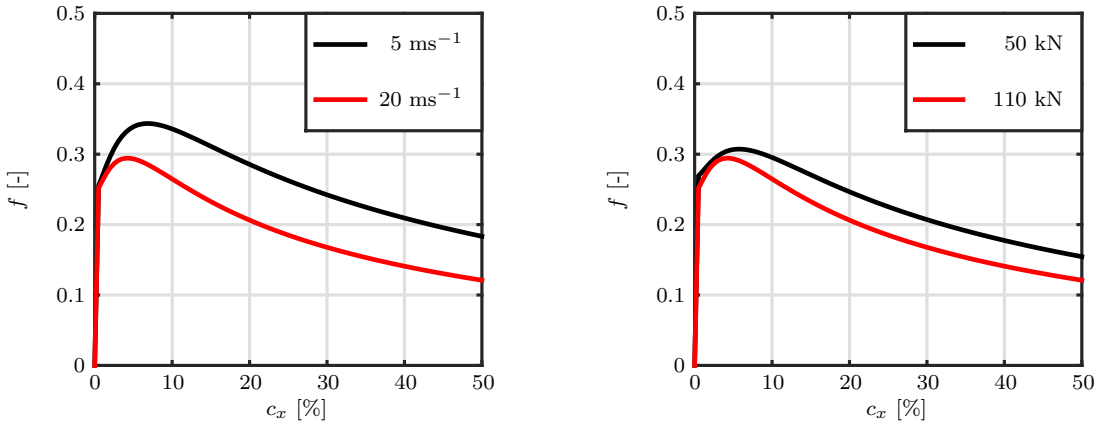

(a) Vehicle velocity dependency.

(b) Normal load dependency.

Fig. 4.11: Parameter study of the influence of the vehicle velocity and the normal load on the traction coefficient (f) depending on the longitudinal creepage (c_x). The default parameters are given in Tab. 4.1.

For even higher creepages, the temperature influence becomes dominant. The decrease of the critical shear stresses now reduces the tangential stress, leading to a decrease of the resulting tangential force, which then leads to the traction loss for very high creepages (R_3) that can be seen in Fig. 4.8(b). As a representation for the local stress behaviour in this regime, $c_x = 30\%$ was chosen. The results are shown Fig. 4.9(d).

As mentioned in Section 3.1 and Section 3.2, it was necessary to develop a model that includes a normal load and velocity dependency. The here developed ECF model is able to reproduce such effects. This is shown in Fig. 4.11: an increase in velocity or an increase in normal load both lead to an increased temperature, which again leads to a decrease of the critical shear stresses and, thus, to a decrease of the overall traction level. The default values are given again in Tab. 4.1. It must be mentioned that the size of the contact was changed due to the Hertzian normal load dependency of the contact area: the half axes were reduced to $a = 5.87$ mm and $b = 6.06$ mm for $F_N = 50$ kN.

Next, the influence of the material parameters mentioned in Eq. (4.3) and Eq. (4.4) was investigated. Therefore, the traction characteristic calculated by the default parameters given in Tab. 4.1 was compared to the traction characteristics with changed parameters. For these investigations, the vehicle velocity was set to $v = 5$ ms^{-1}. The results are shown in Fig. 4.12. Not shown are the influence of L_e^p and L_e^T because they did not significantly change the traction characteristic. However, L_e^0 has an influence on the initial increase of traction for very low creepages (R_1) as shown in Fig. 4.12(a). It is worth noting that this parameter had to be adjusted by three orders of magnitude in this example. Its influence on the rest of the characteristic is insignificant. In Fig. 4.12(b), the influence of the coefficients related to the plastic material properties of the 3BL are shown. These properties influence the maximum of the characteristic. Next, Fig. 4.12(c) shows the influence of the coefficients related to the first critical shear stress (τ_{c1}). These parameters

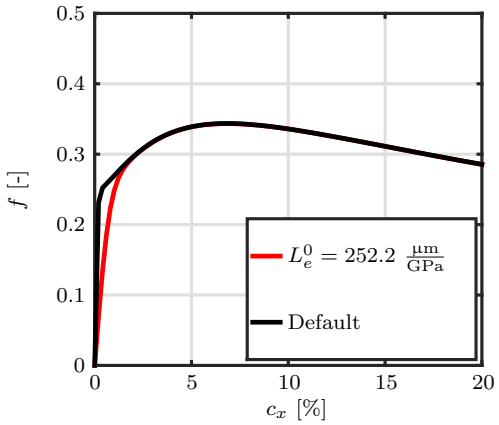

(a) Change in coefficients related to the elasticity of the 3BL.

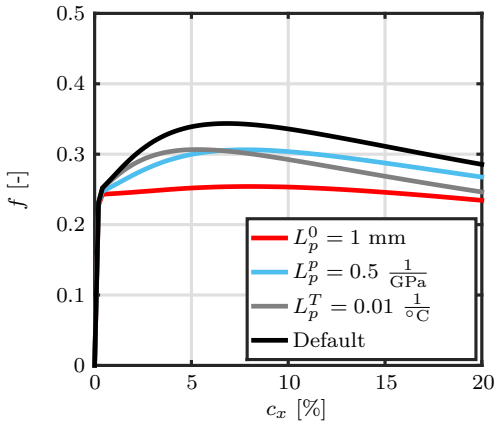

(b) Change in coefficients related to the plasticity of the 3BL.

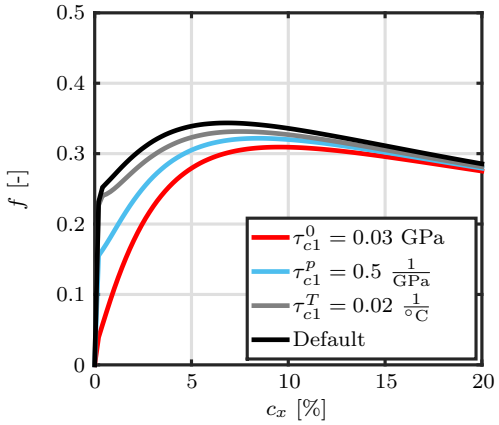

(c) Change in coefficients related to the first critical shear stress τ_{c1} of the 3BL.

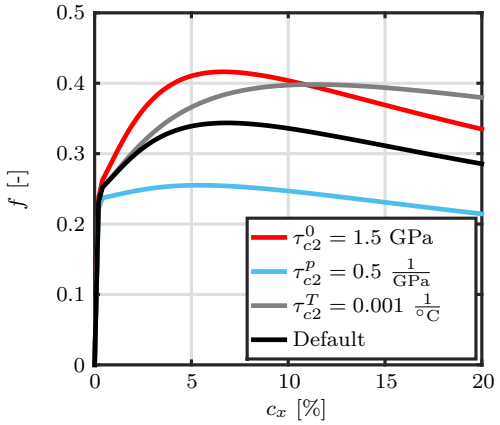

(d) Change in coefficients related to the first critical shear stress τ_{c2} of the 3BL.

Fig. 4.12: Parameter study of the influence of the coefficients in Eq. (4.3) and Eq. (4.4). Default parameters are taken from Tab. 4.1, except the vehicle velocity which was set to $v = 5$ ms^{-1}.

highly influence the moderate increase in traction for medium creepages (R_2). Lastly, the influence of the parameters connected to the second critical shear stress (τ_{c2}) was investigated in Fig. 4.12(d). This parameters highly influence the overall level of traction for medium and high creepages (R_2 and R_3).

4.5 Parameter Study concerning Transient Effects

As mentioned in Section 3.1, drive-train oscillations were observed during the vehicle tests. In this case, the creepage changes rapidly, causing transient effects. To reproduce such effects, the ECF model was formulated to include the time dependency in both, the 3BL sub-model and the Temperature sub-model (see Section 4.1 and Section 4.2).

Table 4.2: Default parameters for investigating transient effects.

$L_e^0 = 0.2522 \frac{\mu m}{GPa}$	$L_p^0 = 0.25$ mm	$\tau_{c1}^0 = 0.3$ GPa	$\tau_{c2}^0 = 1.1$ GPa
$L_e^p = \infty \frac{1}{GPa}$	$L_p^p = 1 \frac{1}{GPa}$	$\tau_{c1}^p = 1 \frac{1}{GPa}$	$\tau_{c2}^p = 1 \frac{1}{GPa}$
$L_e^T = 0 \frac{1}{°C}$	$L_p^T = 0.0025 \frac{1}{°C}$	$\tau_{c1}^T = 0.0025 \frac{1}{°C}$	$\tau_{c2}^T = 0.0025 \frac{1}{°C}$
$F_N = 110$ kN	$v = 5$ ms^{-1}	$a = 7.63$ mm	$b = 7.88$ mm

4.5.1 Results for a Sudden Change of the Creepage

In the first investigation of transient effects, a step function is used to model a sudden change of the longitudinal creepage (c_x)

$$c_x(t) = \begin{cases} c_a & \text{for} \quad t \leq 0 \\ c_b & \text{for} \quad t > 0 \end{cases} \tag{4.36}$$

To analyse the transient behaviour caused by a transition from regime R_1 to R_2 (see also Section 4.4), the longitudinal creepage was changed from $c_a = 0.1\%$ to $c_b = 1\%$.

Results for the tangential stress distribution (τ) at the cross section $y = 0$ are shown in Fig. 4.13 for a coordinate system fixed on the rail and one moving with the wheel. For $t \leq 0$, the creepage is $c_x = 0.1\%$ and the stress distribution is the same as for the steady state. Then, the creepage is changed for $t > 0$ to $c_x = 1\%$ and the stress distribution starts to slowly approach the steady state solution of the new creepage. At $t = \frac{2a}{v} = 3.1$ ms, all bristles remaining in the contact entered the contact at $t > 0$ and, thus, experienced a creepage of $c_x = 1\%$ only. Hence, the stress distribution finally reaches the steady state distribution of $c_x = 1\%$ for $t \geq 3.1$ ms.

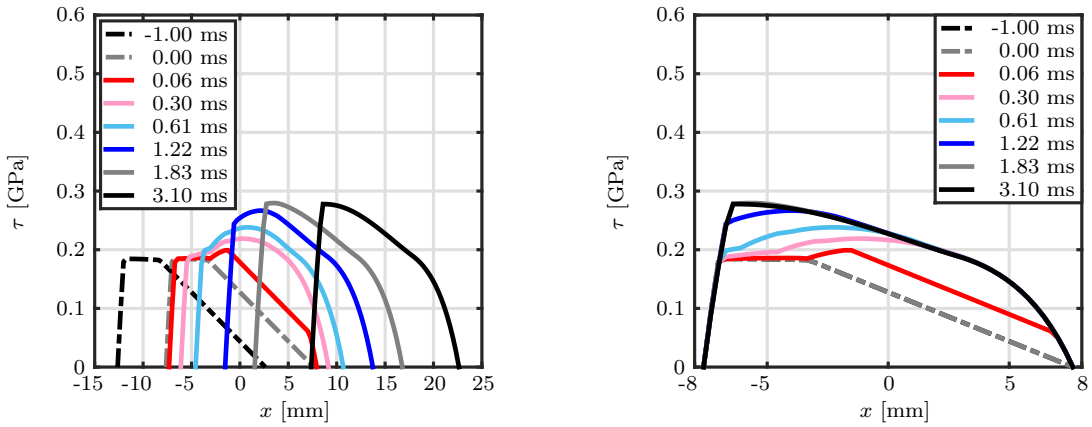

(a) Coordinate system fixed on rail.

(b) Coordinate system moving with wheel

Fig. 4.13: Difference between a coordinate system fixed on the rail and moving with the wheel for the investigation of transient effects. The creepage was changed by a step function as described by Eq. (4.36): $c_a = 0.1\%$ and $c_b = 1\%$.

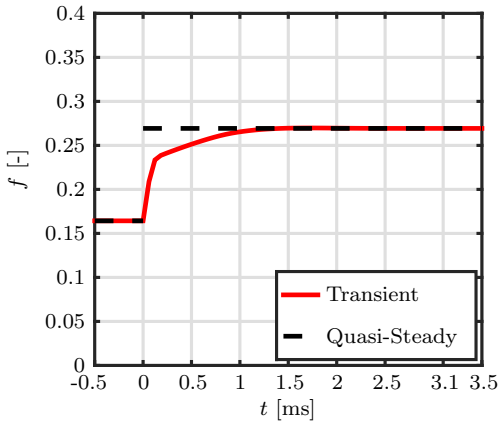

(a) Traction coefficient (f) vs. time (t)

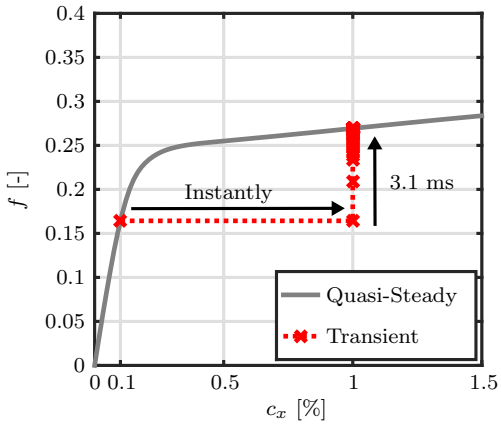

(b) Traction coefficient (f) vs. creepage (c_x)

Fig. 4.14: Transient results compared to the results of quasi-steady state. The creepage was changed by a step function (see Eq. (4.36)): $c_a = 0.1\%$ and $c_b = 1\%$.

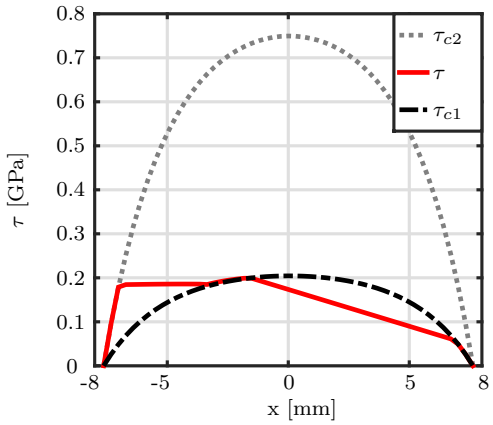

(a) $t = 0.1$ ms

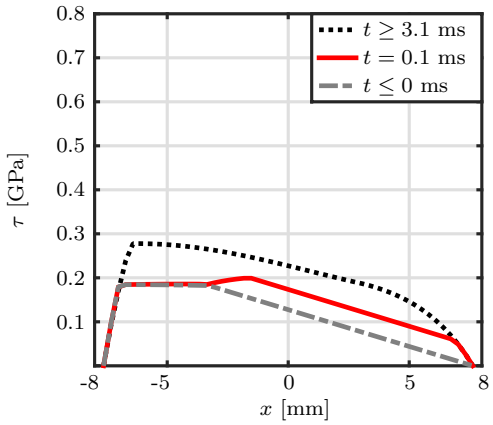

(b) $t = 0.1$ ms

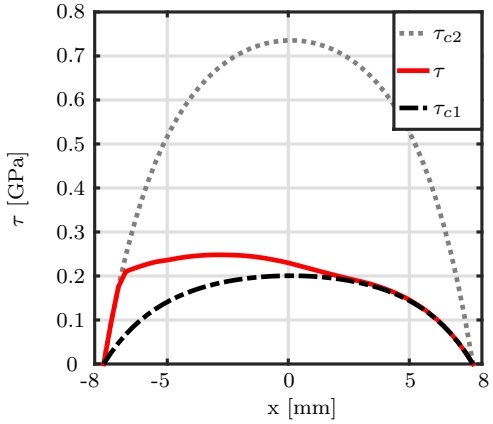

(c) $t = 0.8$ ms

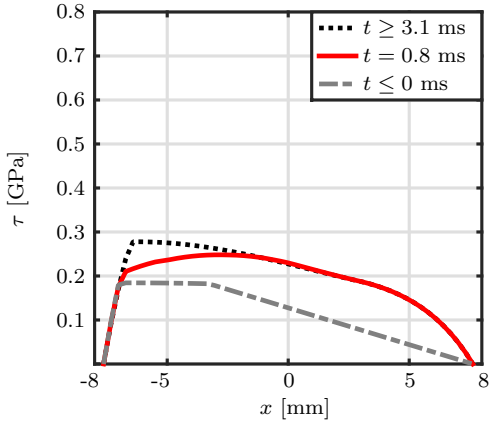

(d) $t = 0.8$ ms

Fig. 4.15: Transient results of the tangential stress distribution (τ), the critical shear stresses (τ_{c1}, and τ_{c2}) for different times (t). The creepages used were $c_a = 0.1\%$ and $c_b = 1\%$ (see Eq. (4.36)).

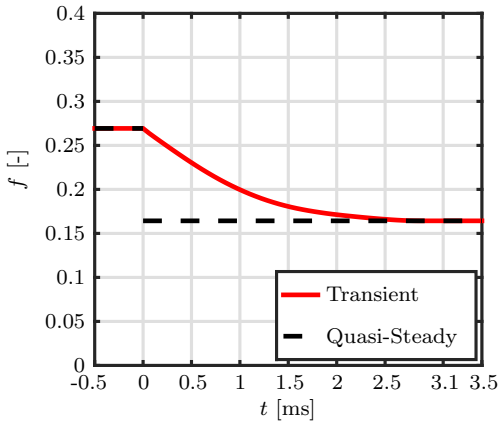

(a) Traction coefficient (f) vs. time (t)

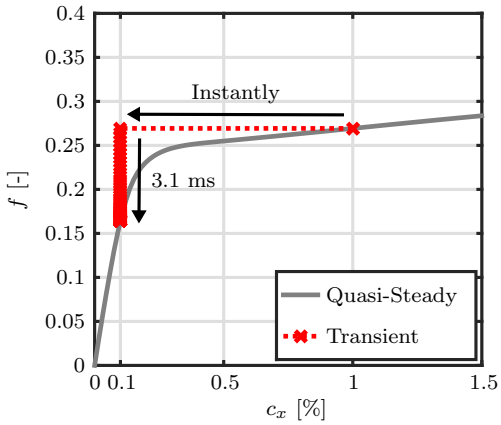

(b) Traction coefficient (f) vs. creepage (c_x)

Fig. 4.16: Transient results compared to the results of quasi-steady state. The creepage was changed by a step function (see Eq. (4.36)): $c_a = 1\%$ and $c_b = 0.1\%$.

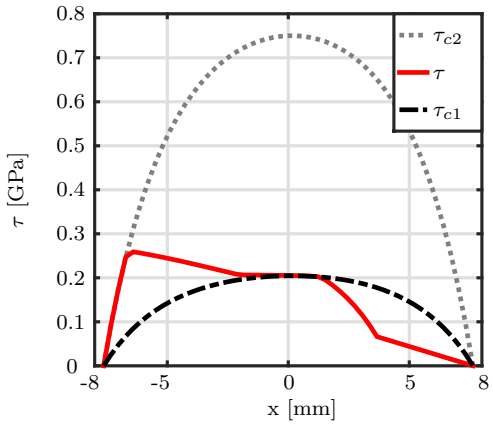

(a) $t = 0.8$ ms

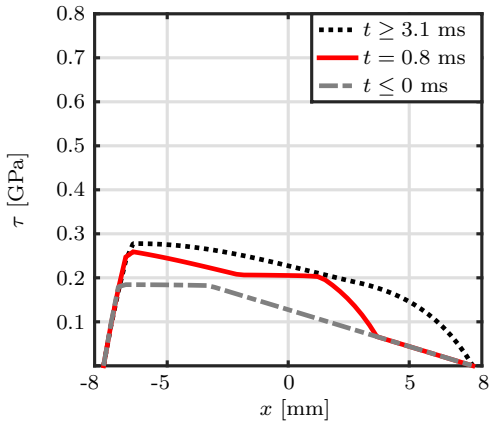

(b) $t = 0.8$ ms

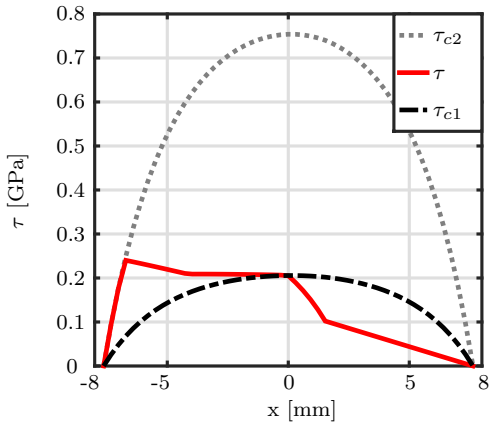

(c) $t = 1.2$ ms

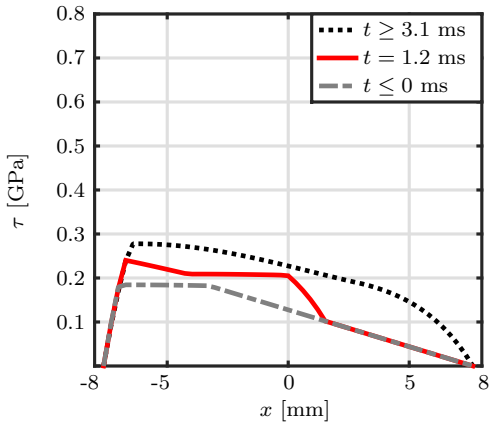

(d) $t = 1.2$ ms

Fig. 4.17: Transient results of the tangential stress distribution (τ), the critical shear stresses (τ_{c1}, and τ_{c2}) for different times (t). The creepages used were $c_a = 0.1\%$ and $c_b = 1\%$ (see Eq. (4.36)).

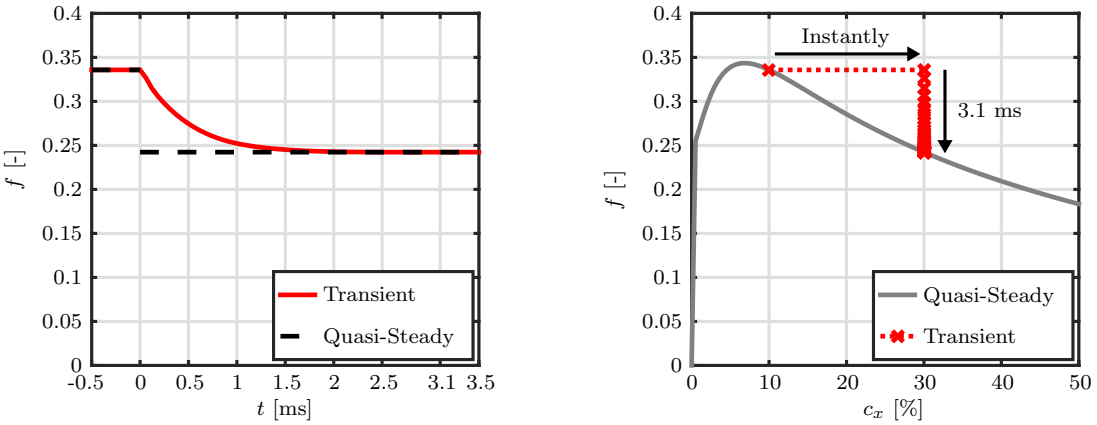

(a) Traction coefficient (f) vs. time (t)

(b) Traction coefficient (f) vs. creepage (c_x)

Fig. 4.18: Transient results compared to the results of quasi-steady state. The creepage was changed by a step function (see Eq. (4.36)): $c_a = 10\%$ and $c_b = 30\%$.

This is also shown in Fig. 4.14(a), where time dependency of the transient result is compared to the results for the quasi-steady state. In Fig. 4.14(b), the result is compared to the traction characteristic of the quasi-steady state, where the creepage is changed slowly enough to avoid transient effects.

Additional information can be gained by looking at the critical shear stress distributions (τ_{c1} and τ_{c2}), which are presented in Fig. 4.15 for a moving coordinate system. At $t = 0.1$ ms, it is shown in Fig. 4.15(a) that the bristles on the leading edge now deform plastically, explaining the increased displacement near the leading edge compared to the initial situation. The bristles around the middle of the contact deform elastically. Near the trailing edge, a similar behaviour as at the initial state can be seen. This leads to an increase in traction as can be seen in Fig. 4.15(b).

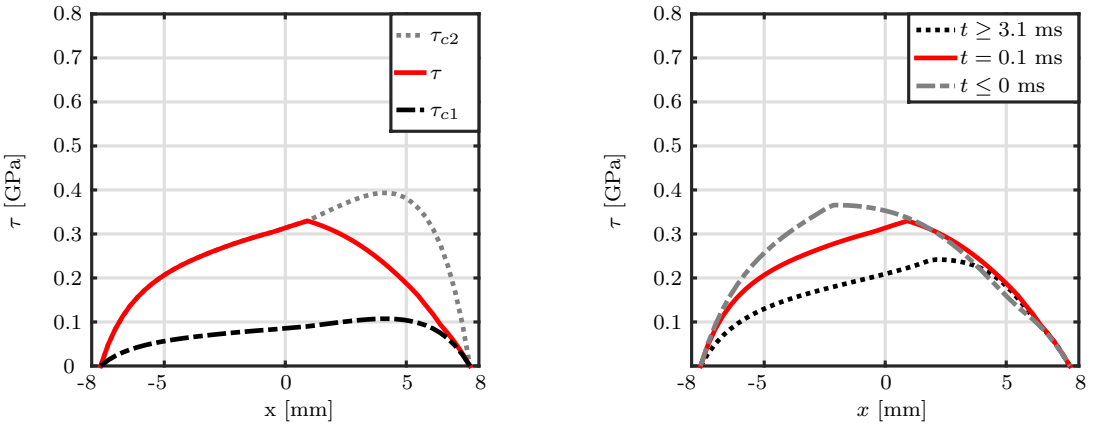

(a) $t = 0.1$ ms

(b) $t = 0.1$ ms

Fig. 4.19: Transient results of the tangential stress distribution (τ), the critical shear stresses (τ_{c1}, and τ_{c2}) for different times (t). The creepages used were $c_a = 10\%$ and $c_b = 30\%$ (see Eq. (4.36)).

The results for $t = 0.8$ ms are shown in Fig. 4.15(c) and Fig. 4.15(d). The resulting stress is now very similar to the results of $t \geq 3.1$ ms, which is also the quasi-steady state solution for $c_x = 1\%$. A small difference can be seen near the trailing edge. There, the bristles were already in the contact at $t \leq 0$.

Next, the reverse case is investigated in Fig. 4.16: the creepage was changed from $c_1 = 1\%$ to $c_2 = 0.1\%$. The results are qualitatively the same, although in the opposite direction. Again, transient effects are visible. Comparing Fig. 4.14(a) to Fig. 4.16(a) shows that the transient result takes longer to approach the quasi-steady state solution in this case. The reason can be seen when closely investigating the local tangential stress as shown in Fig. 4.17. The asymmetric behaviour is caused by a complex interaction of elastic and plastic behaviour together with the time dependency of the displacement. In case of increasing creepage, the leading edge becomes plastic for $t > 0$ ms. Here, the leading edge becomes elastic because of the now lower creepage. This results in an overall smaller change of traction than before, and therefore, a different behaviour.

Another interesting case is the change from $c_a = 10\%$ to $c_b = 30\%$. Both of these creepages are in R_3, where traction is decreasing with increasing creepage. Here, c_a closer to the creepage of the maximum traction. The results of this investigation are shown in Fig. 4.18. Qualitatively, it shows a similar behaviour as Fig. 4.16 but it takes less time to reach a traction close to the quasi-steady state solution. In this case, the underlying effect is highly influenced by the temperature dependency of the material parameters.

Again, this can be seen when investigating the local stress distribution. Fig. 4.19 shows that mainly the temperature dependency of the first and second critical shear stress (τ_{c1} and τ_{c2}) is responsible for the delay, instead of the complex interaction of elastic and plastic behaviour together with the time dependency of the displacement.

In Fig. 4.20, two creepages were chosen from R_2 and R_3 respectively: $c_a = 1\%$ and $c_b =$

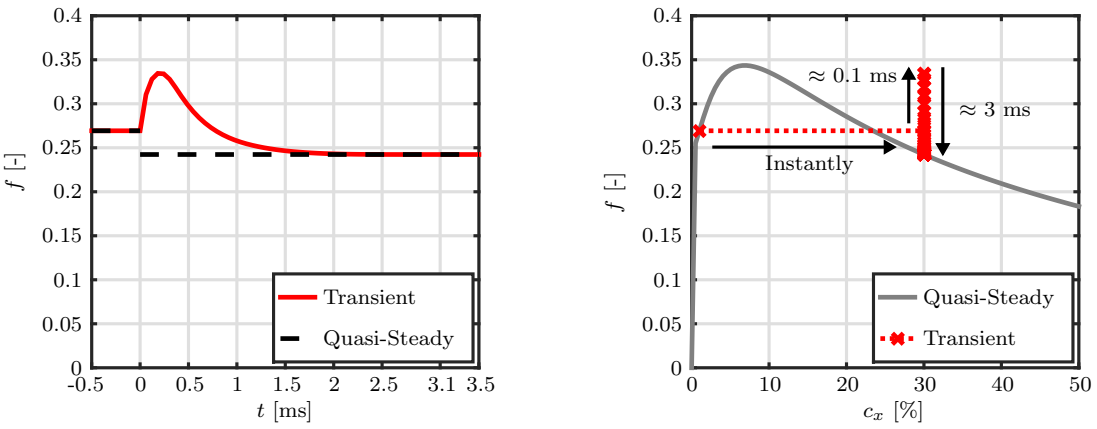

(a) Traction coefficient (f) vs. time (t)

(b) Traction coefficient (f) vs. creepage (c_x)

Fig. 4.20: Transient results compared to the results of quasi-steady state. The creepage was changed by a step function (see Eq. (4.36)): $c_a = 1\%$ and $c_b = 30\%$.

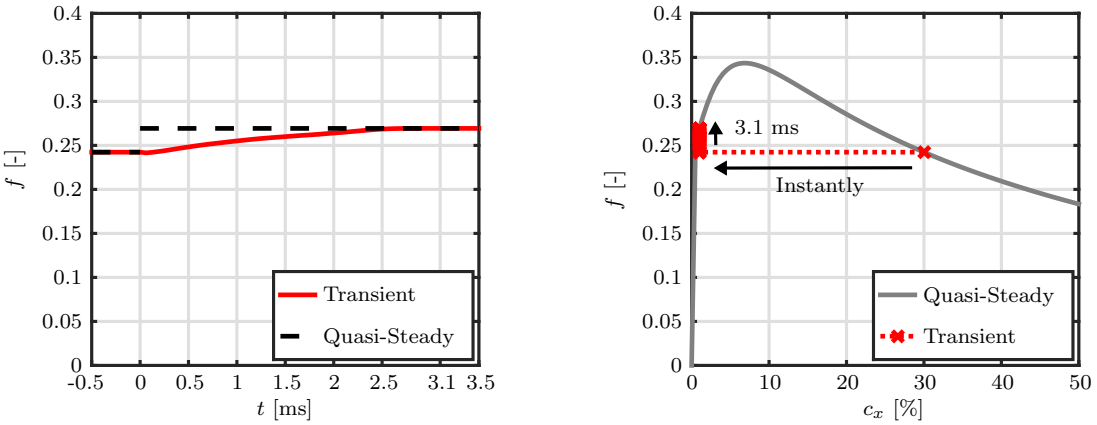

(a) Traction coefficient (f) vs. time (t)

(b) Traction coefficient (f) vs. creepage (c_x)

Fig. 4.21: Transient results compared to the results of quasi-steady state. The creepage was changed by a step function (see Eq. (4.36)): $c_a = 30\%$ and $c_b = 1\%$.

30%. Although the final traction coefficient at $t \geq 3.1$ ms is lower than at the beginning, an increase for 0 ms $< t \lesssim 0.1$ ms can be seen. There, the elasto-plastic displacements grow faster than the rising temperature can compensate (see also Fig. 4.10(b)). For $t \gtrsim 0.1$ ms, the influence of the increasing surface temperature becomes dominant and the resulting stresses decrease until the quasi-steady state solution is reached for $t \geq 0.31$ ms.

Fig. 4.21 shows the inverted transition: $c_1 = 30\%$ and $c_2 = 1\%$. Here, a small decrease of the traction coefficient is visible for 0 ms $< t \lesssim 0.1$ ms. This is less pronounced than the increase shown in Fig. 4.20. As before, the reason is the complex interaction of the temperature dependency and the elasto-plastic displacements in the 3BL.

4.5.2 Results for a Periodic Change of the Creepage

It is assumed that the longitudinal creepage is constant ($c_x = c_m$) for $t \leq 0$ ms. Then, it starts to change periodically. This is described by a sine function with a frequency of f_0:

$$c_x(t) = c_m + c_A \sin(2\pi f_0 t) \tag{4.37}$$

Here, c_m is the mean value and c_A is the amplitude of the oscillation. The material parameters used during these investigations are given in Tab. 4.2.

The first investigation was done for a frequency of $f_0 = 100$ Hz, while the mean value was set to $c_m = 20\%$ and the amplitude of the sine function was $c_A = 10\%$. The material parameters used are given in Tab. 4.2. In Fig. 4.22(a), it is shown that the resulting traction coefficient is also periodic, approaching its limit cycle for $t < 1$ ms. This results in a hysteresis as shown in Fig. 4.22(b), which is compared to the results for the quasi-steady state. Because the minimum and the maximum of the oscillating creepage are both in R_3, the hysteresis is mainly caused by the time dependency of the temperature model.

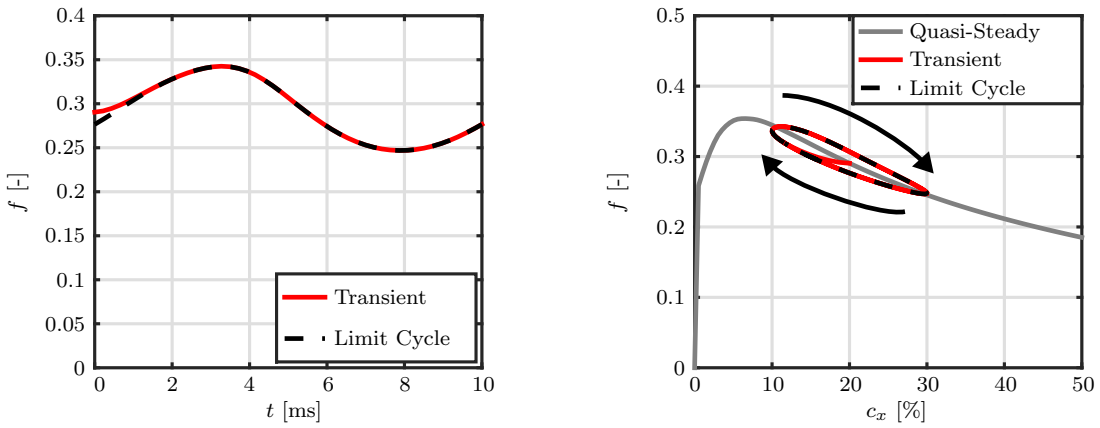

(a) Traction coefficient (f) vs. time (t)

(b) Traction coefficient (f) vs. creepage (c_x)

Fig. 4.22: Transient behaviour of the traction coefficient (f) caused by a periodically changing longitudinal creepage ($c_x(t)$). The parameters chosen for this investigation were $f_0 = 100$ Hz, $c_m = 20\%$ and $c_A = 10\%$. The resulting traction is also periodic and approaches a limit cycle.

The same investigation but with different parameters is shown in Fig. 4.23. Here, the mean value was changed to $c_m = 25\%$ and the amplitude to $c_A = 25\%$. Again, the resulting traction is periodic and approaching a limit cycle, but the shape is much more complex in this case. The traction is non-symmetrical and the resulting hysteresis crosses itself at $c_x \approx 5\%$. The reasons for this behaviour is that the minimum creepage was in $c_{\min} = (c_m - c_A) \in R_1$ while the maximum was in $c_{\max} = (c_m + c_A) \in R_3$. This resulted in a combination of the effects discussed at the end of Chapter 4.5.1 and presented in Fig. 4.20 and Fig. 4.21.

In the following, the influence of the sine function parameters (see Eq. (4.37)) on the limit

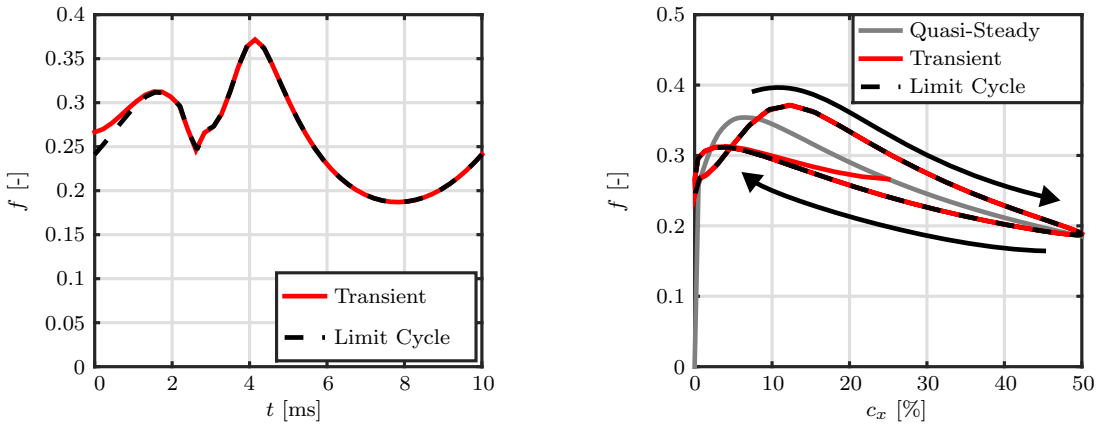

(a) Traction coefficient (f) vs. time (t)

(b) Traction coefficient (f) vs. creepage (c_x)

Fig. 4.23: Transient behaviour of the traction coefficient (f) caused by a periodically changing longitudinal creepage ($c_x(t)$). The parameters chosen for this investigation were $f_0 = 100$ Hz, $c_m = 25\%$ and $c_A = 25\%$. The resulting traction is also periodic and approaches a limit cycle.

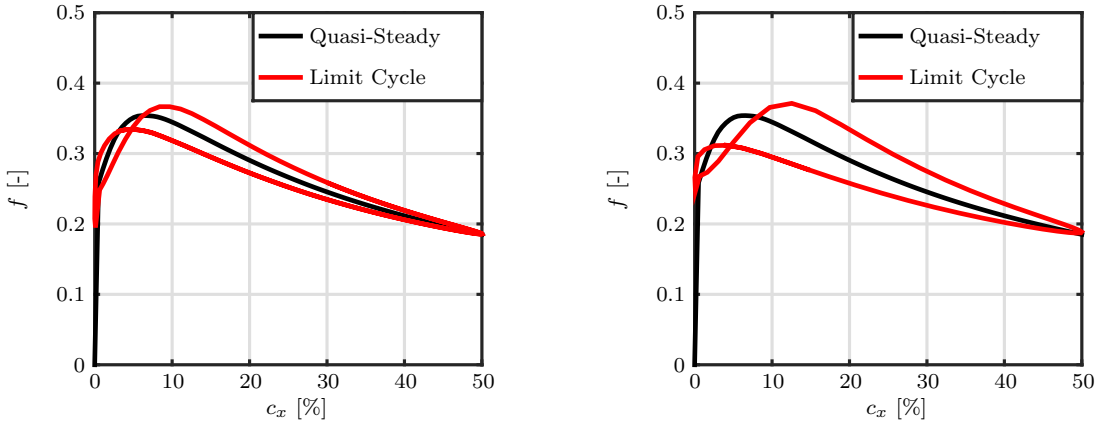

(a) Frequency of $f_0 = 50$ Hz

(b) Frequency of $f_0 = 100$ Hz (Default)

Fig. 4.24: Limit cycle for two different frequencies compared to the quasi-steady state. The material parameters used are given in Tab. 4.2 and the other parameters are $c_m = 25\%$ and $c_A = 25\%$.

cycles are investigated. Therefore, default values were chosen: $f_0 = 100$ Hz, $c_m = 25\%$ and $c_A = 25\%$.

Fig. 4.24 shows the limit cycle for two different frequencies: $f_0 = 50$ Hz and $f_0 = 100$ Hz. Both results are qualitatively the same: a hysteresis, which crosses itself at $c_x \approx 5\%$. Quantitatively, there are differences: for a higher frequency, the bristles have less time to adjust to the new creepage, resulting in a higher deviation compared to the results of the quasi-steady state. It must be added that the quasi-steady state can be interpreted as the limit for $f_0 \to 0$.

The next investigation shows the influence of the vehicle speeds in Fig. 4.25. For higher speeds, it can be seen that the limit cycle deviates less from the quasi-steady state. This

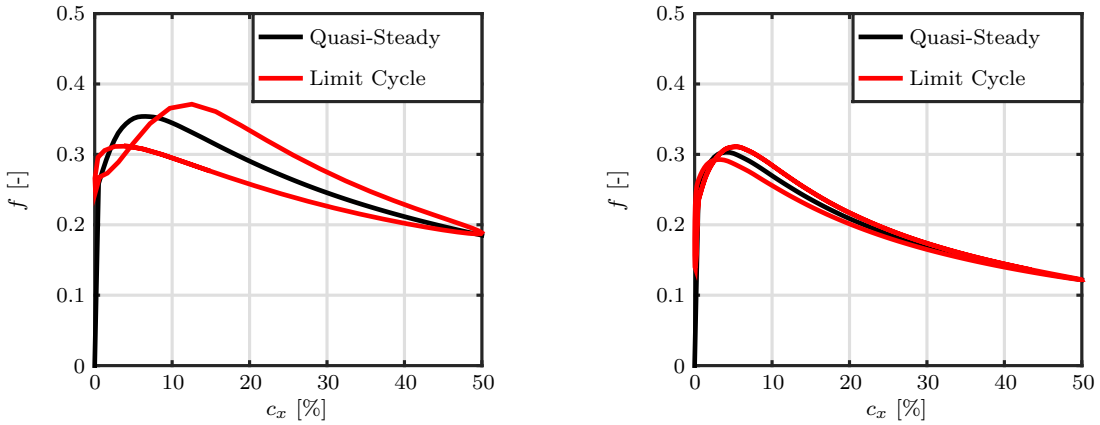

(a) $v = 5$ ms^{-1} (Default)

(b) $v = 20$ ms^{-1}

Fig. 4.25: Limit cycle for two different vehicle speeds compared to the quasi-steady state. The material parameters used are given in Tab. 4.2 and the other parameters are $f_0 = 100$ Hz, $c_m = 25\%$ and $c_A = 25\%$.

qualitatively, this effect is similar to the influence of the frequency on the hysteresis shown in Fig. 4.24. However, it is caused by a different mechanism: the time a bristle needs to traverse the contact is reduced for higher speeds. Thus, the traction coefficient responds faster to a change in creepage.

5 Parametrization

The ECF model, developed in Chapter 4, will now be parametrized with the results of the measurements presented in Chapter 3. Therefore, the set of twelve parameters ($\underline{\lambda} = (\lambda_1, \lambda_2, ...\lambda_i, ..., \lambda_{12}) \in \mathbb{R}^{12}$ with $\lambda_i \geq 0$) had to be found for which the RSME and, thus, the relative error (ϵ), was minimal (see also Eq. (2.9)):

$$\min_{\underline{\lambda} \in \mathbb{R}_+^{12}} (\text{RSME}) = \min_{\underline{\lambda} \in \mathbb{R}_+^{12}} \sqrt{\text{mean}\left([\tau - \hat{\tau}(\underline{\lambda})]^2 \right)} \tag{5.1}$$

First, the results of the HPT test presented in Section 5.1 are used. There, the optimal values for the pressure related coefficients (L_e^p, L_p^p, τ_{c1}^p, τ_{c2}^p) had to be found. Then, L_e^0, L_p^0, τ_{c1}^0, and τ_{c2}^0 are parametrized for different contact conditions, e.g., dry, wet, and sand in the contact.

The remaining parameters (L_e^T, L_p^T, τ_{c1}^T, and τ_{c1}^T) are related to the temperature behaviour of the material. It was not possible to directly measure these coefficients, so an indirect parametrization has to be used. Therefore, one vehicle test result for dry and one for wet conditions, both with a vehicle speed of $v = 10\text{ms}^{-1}$, are used to calibrate these parameters in Section 5.2.

5.1 Parametrization of the 3BL Sub-Model by HPT Test Results

First, the 3BL sub-model is compared to the results of the HPT tests on the first day under dry conditions for two different maximum normal stresses and two different surface roughnesses (see also Section 3.3). Therefore, the pressure related coefficients (L_e^p, L_p^p, τ_{c1}^p, τ_{c2}^p) and also L_e^0, L_p^0, τ_{c1}^0, and τ_{c2}^0 were chosen to minimize the mean relative error from Eq. (5.1). As mentioned in Section 3.3, the rotational speed of the discs was very low to reduce frictional heating. Thus, it was assumed that the contact temperature of the discs was the same as the environmental temperature and the respective parameters (L_e^T, L_p^T, τ_{c1}^T, and τ_{c1}^T) were neglected.

As mentioned in Section 4.4 and shown in Fig. 4.12, changing the inverted elastic stiffness by less than an order of magnitude has no significant influence on the resulting traction characteristic. Using a mean height for the 3BL of 20 µm (see also Section 3.2) and the shear modulus of steel (79.3 GPa) [72], it was possible to calculate an inverted stiffness:

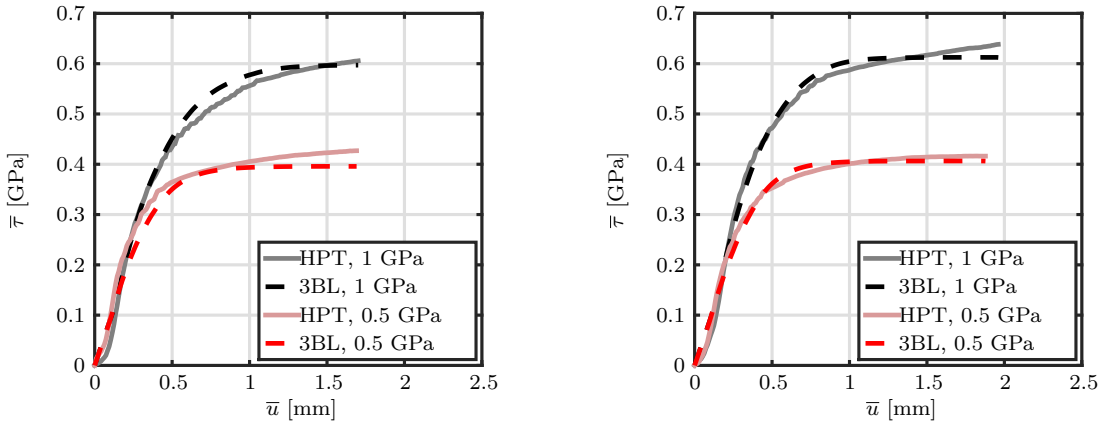

(a) Rough surface

(b) Smooth surface

Fig. 5.1: Comparison of the 3BL submodel to HPT test results for different normal stresses and different roughnesses under dry conditions. The used parameters can be found in Tab. 5.1.

$L_e^0 = \frac{20\ \mu m}{79.3\ GPa} = 0.2522\ \frac{\mu m}{GPa}$. For the remainder of this thesis, this value was used and the influence of the normal stress was neglected: $L_e^p = \infty \frac{1}{MPa}$.

Thus, only six parameters were optimized to fit the model to the test results. A comparison of the 3BL sub-model to the HPT results for dry conditions and two different surface roughnesses is presented in Fig. 5.1. The optimization was performed for every roughness seperately. The calibrated parameters and errors are shown in Tab. 5.1. The results also support the statement mentioned in Section 3.3: the influence of rough and smooth

Table 5.1: Parameters used in the normal stress investigation (Fig. 5.1). Red parameters will be used for the remainder of this thesis.

Roughness	ϵ	Parameters ($\underline{\lambda}$)			
Rough	2.75%	L_e^0 [$\frac{\mu m}{GPa}$]	L_p^0 [mm]	τ_{c1}^0 [GPa]	τ_{c2}^0 [GPa]
		0.2522	0.1640	0.2645	0.8113
		L_e^p [$\frac{1}{GPa}$]	L_p^p [$\frac{1}{GPa}$]	τ_{c1}^p [$\frac{1}{GPa}$]	τ_{c2}^p [$\frac{1}{GPa}$]
		∞	96.561	1.4474	1.3223
Smooth	3.65%	L_e^0 [$\frac{\mu m}{GPa}$]	L_p^0 [mm]	τ_{c1}^0 [GPa]	τ_{c2}^0 [GPa]
		0.2522	0.1490	0.2727	0.8349
		L_e^p [$\frac{1}{GPa}$]	L_p^p [$\frac{1}{GPa}$]	τ_{c1}^p [$\frac{1}{GPa}$]	τ_{c2}^p [$\frac{1}{GPa}$]
		∞	96.561	1.4474	1.3223
Mean Values		$\overline{L_e^0}$ [$\frac{\mu m}{GPa}$]	$\overline{L_p^0}$ [mm]	$\overline{\tau_{c1}^0}$ [GPa]	$\overline{\tau_{c2}^0}$ [GPa]
		0.2522	0.1562	0.2686	0.8231
		$\overline{L_e^p}$ [$\frac{1}{GPa}$]	$\overline{L_p^p}$ [$\frac{1}{GPa}$]	$\overline{\tau_{c1}^p}$ [$\frac{1}{GPa}$]	$\overline{\tau_{c2}^p}$ [$\frac{1}{GPa}$]
		∞	96.561	1.4474	1.3223

Table 5.2: Parameters calibrated for different conditions.

	Dry, Dry-Sanded, Wet-Sanded				
	ϵ	L_e^0 $[\frac{\mu m}{GPa}]$	L_p^0 [µm]	τ_{c1}^0 [GPa]	τ_{c2}^0 [GPa]
Day1	4.33%	0.2522	0.1700	0.2574	0.8196
Day2	10.68%	0.2522	0.4112	0.4167	0.5715
Day3	8.30%	0.2522	0.2480	0.1674	0.6817
Mean Values		0.2522	0.2429	0.2805	0.6909
	Wet				
	ϵ	L_e^0 $[\frac{\mu m}{GPa}]$	L_p^0 [µm]	τ_{c1}^0 [GPa]	τ_{c2}^0 [GPa]
Day1	10.36%	0.2522	0.1755	0.1525	0.6360
Day3	3.72%	0.2522	0.1196	0.2658	0.4884
Mean Values		0.2522	0.1422	0.2092	0.5622

surfaces was not significant, especially regarding the normal stress dependency. Therefore, the mean values for the pressure dependent parameters ($\overline{L_e^p}$, $\overline{L_p^p}$, $\overline{\tau_{c1}^p}$, and $\overline{\tau_{c2}^p}$) will be used for all subsequent calculations of the work presented in this thesis.

As mentioned in Section 3.3, dry, dry-sanded, and wet-sanded conditions showed similar results when performed on the same day, while the overall friction level differed from day to day. Therefore, the test results for each day were investigated separately to calibrate the parameters L_p^0, τ_{c1}^0, and τ_{c2}^0 for these conditions. The results are shown in Tab. 5.2. Also shown there are the results and the mean values for the investigation of wet conditions.

One very interesting result of this investigation is that all mean values for wet conditions are lower than for dry conditions. While it is easy to explain that water reduces the shear resistance in the contact and, thus, τ_{c1} and τ_{c2}, it is also interesting to see that the plasticity coefficient L_P is lower, which results in a less strain-hardening-like behaviour of the material compared to dry conditions (see also Section 3.3).

As mentioned before in Section 3.3, there are uncertainties in the results of the HPT tests. It should be added that such uncertainties were also found during the vehicle tests in Section 3.1. So, the chosen values for the parameters are not strictly defined and unchangeable, but rather softly defined and might be subject for additional future discussions and investigations. Additional tests will give more insight and will help to tighten the boundaries in which these values can be chosen from.

Nevertheless, the mean values from Tab. 5.2 and values presented in red from Tab. 5.1 will be used in the next section to calibrate the temperature related parameters by comparing the results of the ECF model to two selected vehicle tests.

5.2 Parametrization of the Temperature Coefficients by Vehicle Tests

Now, the temperature coefficients (L_e^T, L_p^T, τ_{c1}^T, and τ_{c1}^T) from Eq. (4.3) and Eq. (4.4) need to be parametrized. These define the shape of the traction loss that occurs at high creepages (R_3, see also Section 3.1 and Section 4.4).

Therefore, two of the measurements from the vehicle tests, one with dry conditions, one with wet conditions, are used to calibrate the necessary parameters accordingly. Using the same arguments as mentioned in Section 5.1, the temperature influence on the inverted elastic stiffness was neglected and, thus, the respective parameter was set to zero: $L_e^T = 0\frac{1}{°\mathrm{C}}$.

It must be added that the results for low creepages ($c_x < 1\%$) were neglected: there, the contact temperature is relatively low ($T \leq 43°\mathrm{C}$) and, thus, the temperature dependency is insignificant compared to all other influences. The results are shown in Fig. 5.2 and the chosen parameters are displayed in Tab. 5.3 for both conditions with the respective relative error (ϵ).

For dry conditions, an interesting result of the parametrization is that the temperature influence of the the plasticity factor (L_p^T) does not significantly effect the resulting relative error (ϵ). Thus, it was also neglected and set to zero.

However, for wet conditions, the temperature dependency of the plasticity factor (L_p^T) shows a high influence on the quality of the model results. Even more prominent is the temperature influence regarding the first critical shear stress (τ_{c1}^T) compared to dry conditions. On the other hand, the value of τ_{c2}^T is lower in this case than for dry conditions.

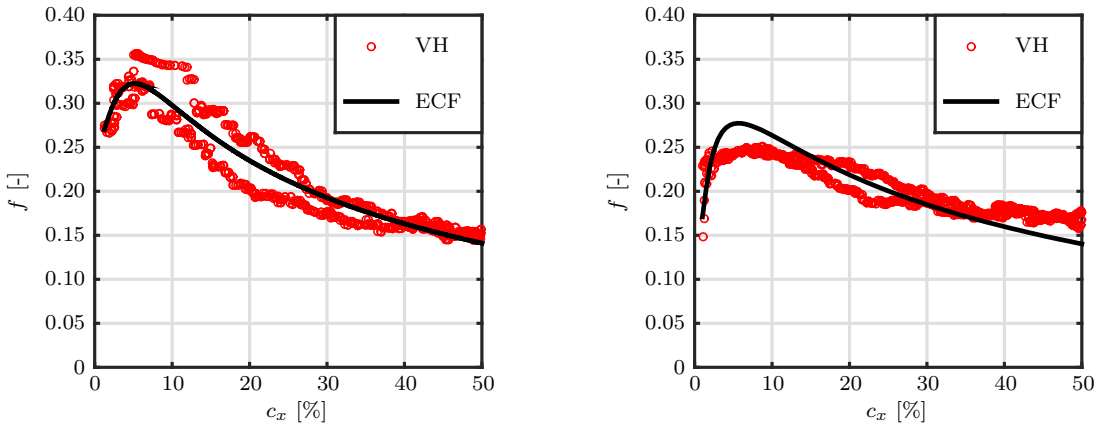

(a) Dry conditions, Section V, Day 1

(b) Wet conditions, Section IV, Day 2

Fig. 5.2: Comparison of vehicle tests (VH) and ECF model results for $v = 10$ ms^{-1} and two different contact conditions on two different days and sections. The parameters used are given in Tab. 5.1, Tab. 5.2, and Tab. 5.3.

Table 5.3: Temperature related parameters used for dry and wet conditions.

Condition	ϵ	L_e^T $[\frac{1}{°C}]$	L_p^T $[\frac{1}{°C}]$	τ_{c1}^T $[\frac{1}{°C}]$	τ_{c2}^T $[\frac{1}{°C}]$
Dry	8.64%	0	0	0.03368	0.00253
Wet	9.10%	0	0.01179	0.54879	0.00150

This leads to a different temperature behaviour when comparing dry and wet conditions as shown in Fig. 5.3. Although the overall friction level is decreasing for higher temperatures, the curves for dry conditions look qualitatively similar regardless of temperature. For wet conditions, the shape of the curves changes due to the temperature dependency of the plasticity factor and the material behaviour becomes dominated by its plasticity for higher temperatures.

Finally, the parameters used for the remainder of this thesis can be found in Tab. 5.4.

Table 5.4: Final parameters used in the remainder of this thesis.

Condition	Parameters			
All	$L_e^p = \infty \frac{1}{\text{GPa}}$	$L_p^p = 96.6 \frac{1}{\text{GPa}}$	$\tau_{c1}^p = 1.45 \frac{1}{\text{GPa}}$	$\tau_{c2}^p = 1.32 \frac{1}{\text{GPa}}$
Dry	$L_e^0 = 0.25 \frac{\mu\text{m}}{\text{GPa}}$	$L_p^0 = 0.24$ mm	$\tau_{c1}^0 = 0.28$ GPa	$\tau_{c2}^0 = 0.69$ GPa
	$L_e^T = 0 \frac{1}{\text{GPa}}$	$L_p^T = 0 \frac{1}{\text{GPa}}$	$\tau_{c1}^T = 0.034 \frac{1}{\text{GPa}}$	$\tau_{c2}^T = 0.0025 \frac{1}{\text{GPa}}$
Dry-Sanded	$L_e^0 = 0.25 \frac{\mu\text{m}}{\text{GPa}}$	$L_p^0 = 0.24$ mm	$\tau_{c1}^0 = 0.28$ GPa	$\tau_{c2}^0 = 0.69$ GPa
Wet-Sanded	$L_e^T = 0 \frac{1}{\text{GPa}}$	$L_p^T = 0 \frac{1}{\text{GPa}}$	$\tau_{c1}^T = 0.034 \frac{1}{\text{GPa}}$	$\tau_{c2}^T = 0.0025 \frac{1}{\text{GPa}}$
Wet	$L_e^0 = 0.25 \frac{\mu\text{m}}{\text{GPa}}$	$L_p^0 = 0.14$ mm	$\tau_{c1}^0 = 0.21$ GPa	$\tau_{c2}^0 = 0.56$ GPa
	$L_e^T = 0 \frac{1}{\text{GPa}}$	$L_p^T = 0.012 \frac{1}{\text{GPa}}$	$\tau_{c1}^T = 0.559 \frac{1}{\text{GPa}}$	$\tau_{c2}^T = 0.0015 \frac{1}{\text{GPa}}$

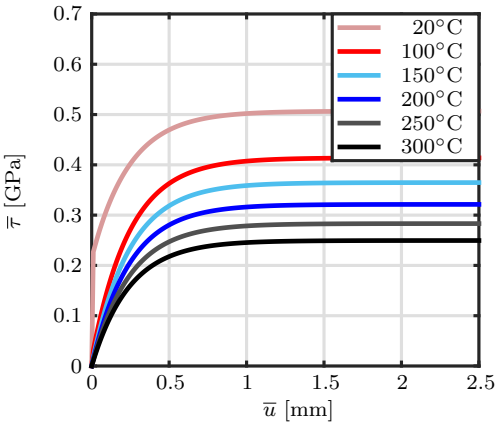

(a) Dry, Dry-Sanded, Wet-Sanded conditions

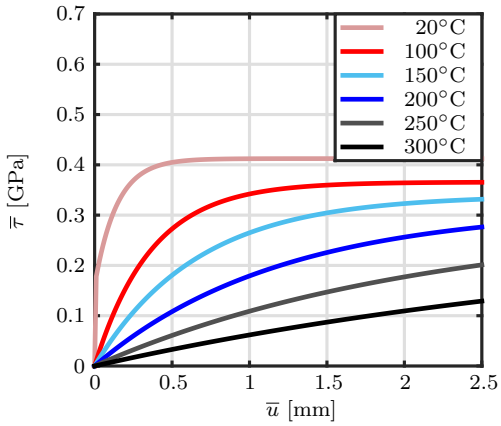

(b) Wet conditions

Fig. 5.3: Results for the parametrized material behaviour in the ECF model for different temperatures and contact conditions. The normal stress was set to 1 GPa. The parameters used are given in Tab. 5.1, Tab. 5.2, and Tab. 5.3.

6 Validation

In Chapter 5, the ECF model was parametrized and the results are presented in Tab. 5.4. Now, the model with this set of calibrated parameters is compared to different test results:

- First, the results of the ECF model and the other three models from the literature (see also Section 2.2) are compared to the quasi-steady drive-train behaviour of the vehicle tests presented in Section 3.1.1.
- Then, the ECF model is used to reproduce drive-train oscillations caused by transient effects as described in Section 3.1.2. Therefore, the ECF model was implemented as a subroutine into a Multi Body System software, i.e., SIMPACK. The same was done with FASTSIM and the results are then compared.
- At last, the results of the Twin-Disc tests from Section 3.2 are used to validate the normal stress dependency used in the ECF model.

6.1 Validation for Quasi-Steady Drive-Train Behaviour

In Section 3.1.1, the quasi-steady behaviour of the drive-train during the vehicle tests were presented and are now used for validation purposes. Therefore, the results of the ECF model are compared to the mean mean traction coefficient (f) depending on the mean creepage (c_x) of both wheels on the first axle (see also Eq. (3.5) and Eq. (3.2)).

First, the results of the ECF model were compared to the vehicle tests in section II under dry conditions. In Fig. 6.1, this comparison is presented together with the comparison to the three other models (see also Section 3.1 and Fig. 3.8). It can be seen that the results of the ECF model replicates the traction characteristic of the vehicle tests significantly better than the other three models: it is able to reproduce the velocity dependency, the

Table 6.1: The Relative error as defined by Eq. (2.9) for different models:

Model	5 ms^{-1}	20 ms^{-1}	Mean
FASTSIM	27.58%	49.53%	38.56%
Polach	21.30%	12.73%	17.01%
Tomberger	21.91%	17.07%	19.49%
ECF	11.52%	7.75%	9.63%

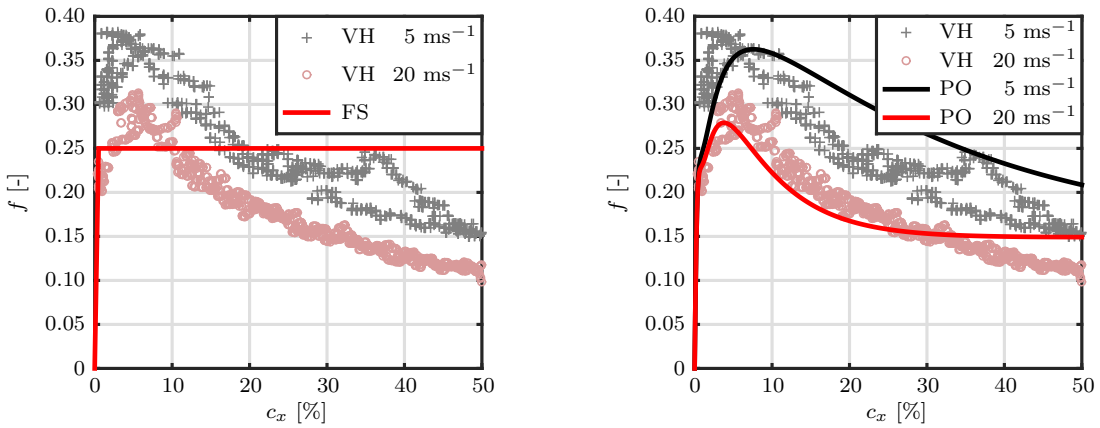

(a) Comparison to FASTSIM (FS)

(b) Comparison to Polach (PO) model

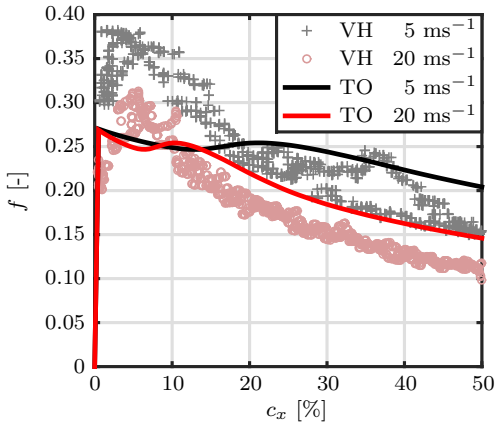

(c) Comparison to Tomberger (TO) model

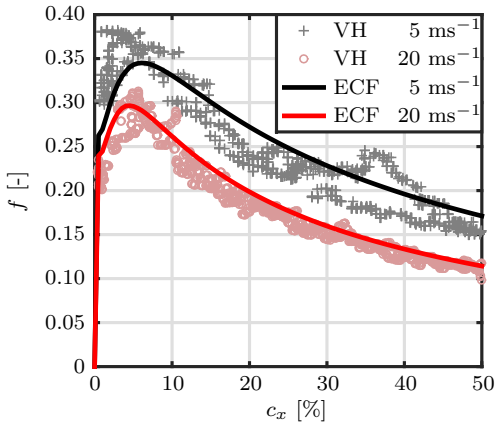

(d) Comparison to ECF model

Fig. 6.1: Comparison of the vehicle (VH) tests in section II under dry conditions to the three different models from the literature and the ECF model.

traction loss for high creepages (R_3), and the quantitative values of the measured traction characteristics. Thus, the relative errors (see also Eq. (2.9)) are all 5% to 10% lower for the ECF model compared to the other models as shown in Tab. 6.1: the mean relative error is even smaller than 10%. It must also be added that the vehicle test data used for the parametrization was not used in this comparison.

Next, Fig. 6.2 shows the results of a comparison of the parametrized ECF model to the vehicle tests for four different contact conditions and three different vehicle speeds. The relative errors are given in Tab. 6.2.

It can be seen that the mean error for dry conditions is low ($\bar{\epsilon} < 10\%$) compared to the other results ($15\% < \bar{\epsilon} < 30\%$). However, an investigation of the residual errors shows that the deviation between model and measurement is very large for low creepages ($c_x < 1\%$), where the increase in traction is very steep. This is also the part of the measurements, where small uncertainties during the test can cause huge inaccuracies of the results.

Therefore, the relative errors for $c_x \geq 1$ are given in Tab. 6.3. Comparing the errors for

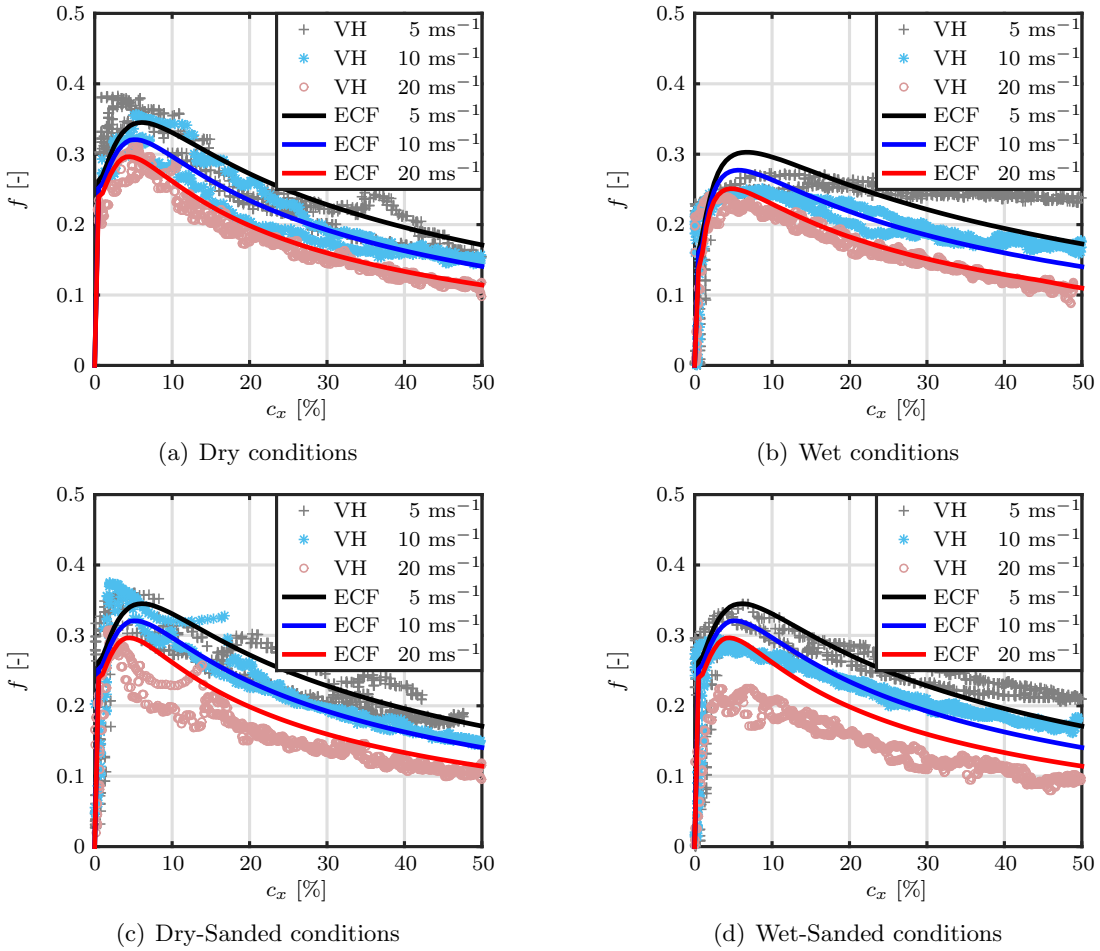

(a) Dry conditions

(b) Wet conditions

(c) Dry-Sanded conditions

(d) Wet-Sanded conditions

Fig. 6.2: Comparison of the results from the vehicle tests to the results of the ECF model that was parametrized in Chapter 5.

dry conditions to the results presented in Tab. 6.2 reveals no significant change: there were nearly no operating points with $c_x < 1\%$ in this case. However, nearly all other errors are reduced significantly, and all of their values, except two, are now below 16%. These two cases are the results for dry-sanded and wet-sanded conditions with a speed of $v = 20$ ms^{-1}. As discussed in Section 3.1.1, this might be attributed to uncertainties in the measurements, predominantly the speed independent application of the sand. Neglecting these values results in a mean error that is below 15% for all conditions.

Table 6.2: The relative error (ϵ) as defined by Eq. (2.9) for different conditions:

Condition	5 ms^{-1}	10 ms^{-1}	20 ms^{-1}	Mean
Dry	11.52%	8.64%	7.75%	9.30%
Wet	21.63%	19.51%	13.18%	18.11%
Dry-Sanded	21.09%	15.77%	23.43%	20.10%
Wet-Sanded	24.33%	22.52%	36.61%	27.82%

Table 6.3: The relative error (ϵ) as defined by Eq. (2.9) for $c_x \geq 1\%$:

Condition	5 ms^{-1}	10 ms^{-1}	20 ms^{-1}	Mean
Dry	11.12%	8.64%	7.52%	9.09%
Wet	15.79%	9.14%	8.16%	11.03%
Dry-Sanded	12.79%	10.27%	19.49%	14.18%
Wet-Sanded	15.41%	9.03%	33.75%	19.40%

6.2 Validation for Drive-Train Oscillations

One of the goals of this thesis was to develop a model that is able to reproduce the drive-train oscillations that occurred during the vehicle tests as in mentioned in Section 3.1.2. Therefore, Multi-Body-System (MBS) simulations were performed with SIMPACK, in which a model of a Vectron locomotive with two bogies was used. Each bogie is equipped with two wheelsets with independent drive-trains. The model used for the drive-trains is shown in Fig. 6.3.

A desired longitudinal creepage ($c_{x,\mathrm{des}}$) was prescribed and using the vehicle speed (v), the wheel radius (R), and the gear ratio (j_G), a desired angular motor speed ($\omega_{M,\mathrm{des}}$) was calculated from

$$c_{x,\mathrm{des}} = \frac{j_G v - \omega_{M,\mathrm{des}} R}{j_G v} \tag{6.1}$$

The function of the controller was to adjust the motor torque (T_M) in order to minimize the difference between the actual motor speed and the desired one:

$$\min_{T_M \geq 0} \left(\omega_M(T_M) - \omega_{M,\mathrm{des}}\right) \tag{6.2}$$

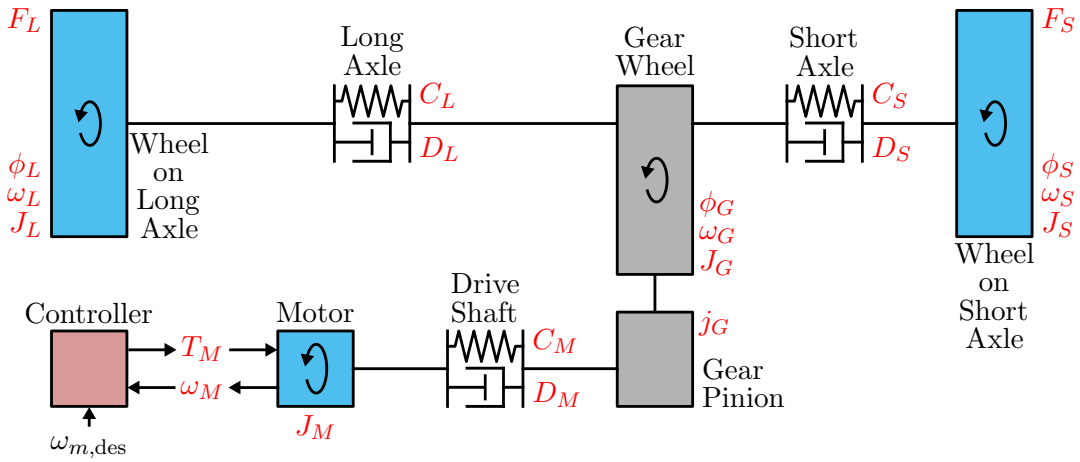

Fig. 6.3: Schematic overview of the wheelset model used in SIMPACK for investigations of drive-train oscillations.

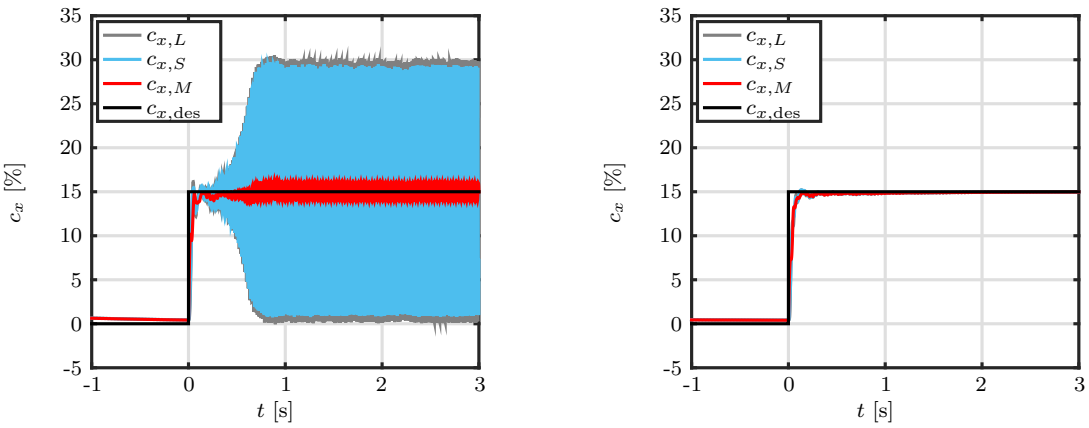

(a) SIMPACK with ECF

(b) SIMPACK with FASTSIM

Fig. 6.4: Results of the SIMPACK investigations on a straight track with a sudden change in creepage from $c_x = 0\%$ to $c_x = 15\%$. Shown is the influence of two different creep force models: ECF model and FASTSIM.

Fig. 6.4 shows the results of two SIMPACK simulations on a straight track with a vehicle velocity of $v = 5$ ms^{-1}. To simulate a transition from the regime R_1 to R_3 (see also Section 3.1 and Section 4.4), the desired creepage in the controller was suddenly changed from $c_{x,\mathrm{des}} = 0\%$ to $c_{x,\mathrm{des}} = 15\%$ at $t = 0$ s. Investigated were the longitudinal creepage of the wheel on the long axle ($c_{x,L}$), the longitudinal creepage of the wheel on the short axle ($c_{x,S}$) and the creepage ($c_{x,M}$) calculated from the angular speed of the motor by

$$c_{x,M} = \frac{j_G v - \omega_M R}{j_G v} \tag{6.3}$$

The results presented in Fig. 6.4(a) were obtained by using the ECF model to calculate the creep forces. It must be noted that the transient effects of the creep force were neglected in this investigation to lower the computational effort. Nevertheless, $c_{x,L}$, $c_{x,S}$, and $c_{x,M}$ are oscillating with a frequency of $f_0 \approx 54$ Hz.

To investigate this behaviour more closely, the damping of the contact (D_C) can be calculated by

$$F_N \Delta f = -D_C v \Delta c_x \tag{6.4}$$

where F_N is the normal load and v the vehicle speed. A linear stability analysis revealed that the system becomes unstable if the damping of the contact exceeds a certain threshold: $D_C \geq D_{\mathrm{stab}}$. For the parameters chosen in this investigation, this is the case if $c_x = 15\%$ due to the decreasing traction for high creepages in R_3 (see also Section 3.1.1 and Section 4.4).

In Fig. 6.4(b), FASTSIM was used as the creep force model. There, a constant coefficient of friction is assumed and, thus, the damping for $c_x = 15\%$ is below the threshold: $D_C = 0 < D_{\mathrm{stab}}$. Hence, no significant oscillations of $c_{x,L}$, $c_{x,S}$, and $c_{x,M}$ can be observed.

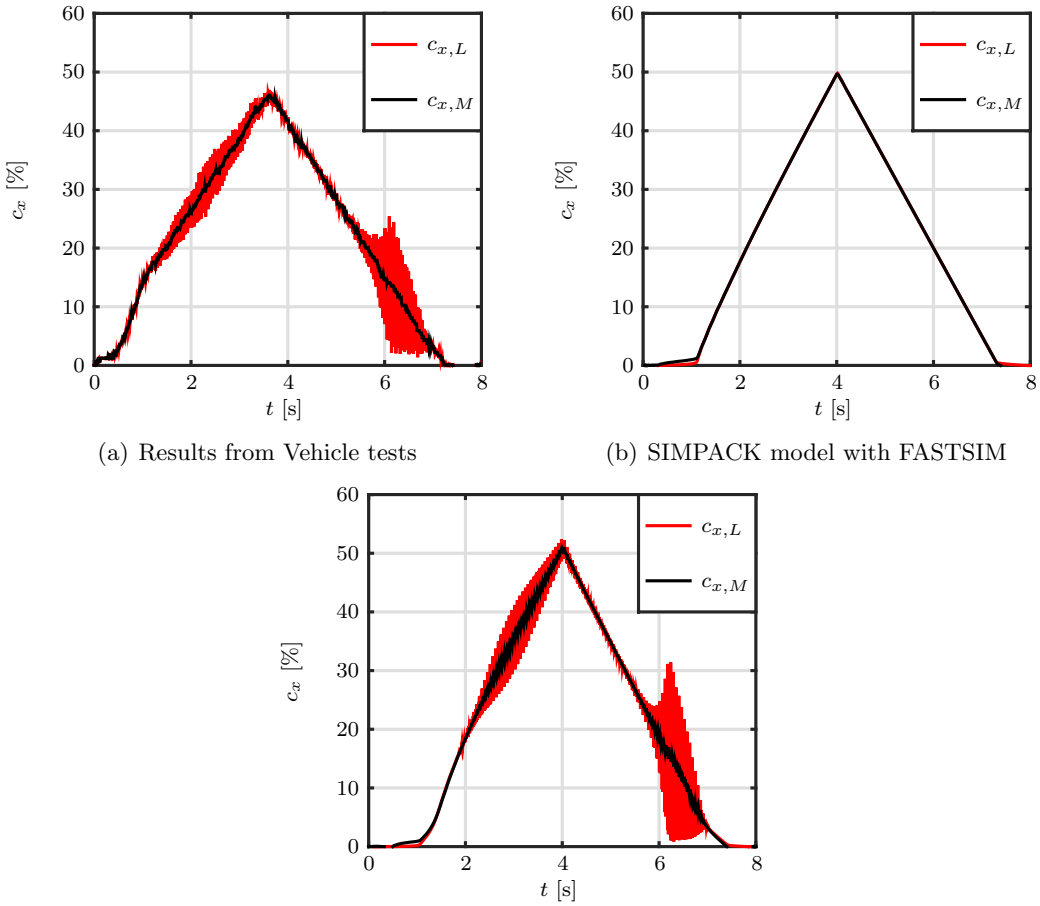

(a) Results from Vehicle tests

(b) SIMPACK model with FASTSIM

(c) SIMPACK model with ECF model

Fig. 6.5: Drive-train oscillations in vehicle tests and in the SIMPACK simulation for a vehicle velocity of $v = 5$ ms^{-1}.

After this initial investigation, the controller was modified to reproduce the creepage used during the vehicle tests as presented in Section 3.1. As shown in Fig. 3.1(b), the desired longitudinal creepage was increased and decreased from 0% to 50% and back in 8 s. Due to the used measurement procedure during the vehicle tests (see Section 3.1), only the behaviour of $c_{x,L}$ and $c_{x,M}$ were investigated here.

Fig. 6.5 shows the results of the vehicle tests compared to the SIMPACK simulations performed with the ECF model and FASTSIM to calculate the creep forces. It must be mentioned that the controller used in the simulation was a very simplified version of the real controller. Due to this fact and due to additional measurement inaccuracies, differences in the resulting creepage behaviour are expected, such as the differences in the initial increase or the maximum, which is higher in the simulation. Also, the oscillations of $c_{x,M}$ were not measurable during the tests.

However, the comparison shows that FASTSIM is not able to replicate the drive train oscillations observed during the vehicle tests. The reasons are the same as mentioned

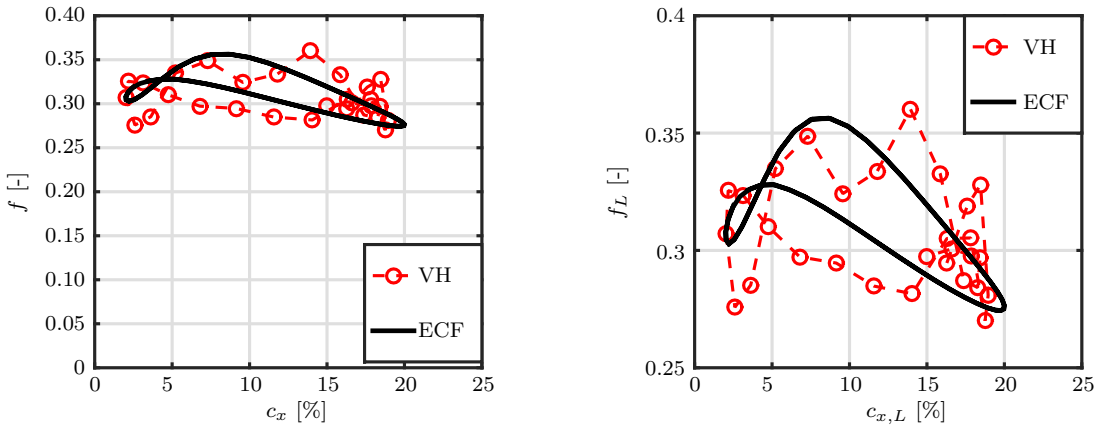

(a) Comparison of the vehicle test data (VH) to the results of the ECF

(b) Closer inspection of the comparison of the vehicle test data (VH) to the results of the ECF

Fig. 6.6: Hysteresis of the coefficient of traction of the wheel on the long axle (f_L) caused by the transient behaviour of the creepage ($c_{x,L}$) due to drive-train oscillations.

above: it is not able to produce unstable operating points. On the other hand, the ECF model is able to reproduce these instabilities and, therefore, is able to replicate the oscillation observed during the vehicle tests: the same asymmetry, the same frequency of 53 Hz, and a similar amplitude of the oscillations.

These oscillations of $c_{x,L}$ cause a transient behaviour of the resulting traction coefficient (f_L) that is shown in Fig. 6.6. The vehicle tests show a hysteresis due to rapid changes in the creepage as mentioned in Section 3.1.2. This is compared to the results of the ECF model. There, the oscillations of the creepage were modelled as sine functions with an amplitude of $c_A = 10\%$, a mean value of $c_m = 12\%$ and a frequency of 53 Hz (see Eq. (4.37)). Both results show a qualitative similar behaviour agreement: a similarly shaped, complex hysteresis encircling the steady state solution in the same direction. The resulting relative error is $\epsilon = 7.35\%$.

6.3 Validation by Twin-Disc Tests

In section Section 3.2, the performed Twin-Disc experiments were explained in detail. The results of these tests for two different normal loads are now compared to the results of the ECF model and the two other models from the literature (see also Section 2.2). Therefore, the same set of parameters was used as in Section 6.1. The results are shown in Fig. 6.7. There, it can be seen that the resulting creep forces are too low compared to the results of the Twin-Disc tests.

During the Twin-Disc tests, more than 16000 revolutions occurred, generating a 3BL with a thickness of up to 50 µm (see Section 3.2). On the other hand, the HPT tests were performed for only four cycles. Therefore, it is not expected that a significant 3BL was

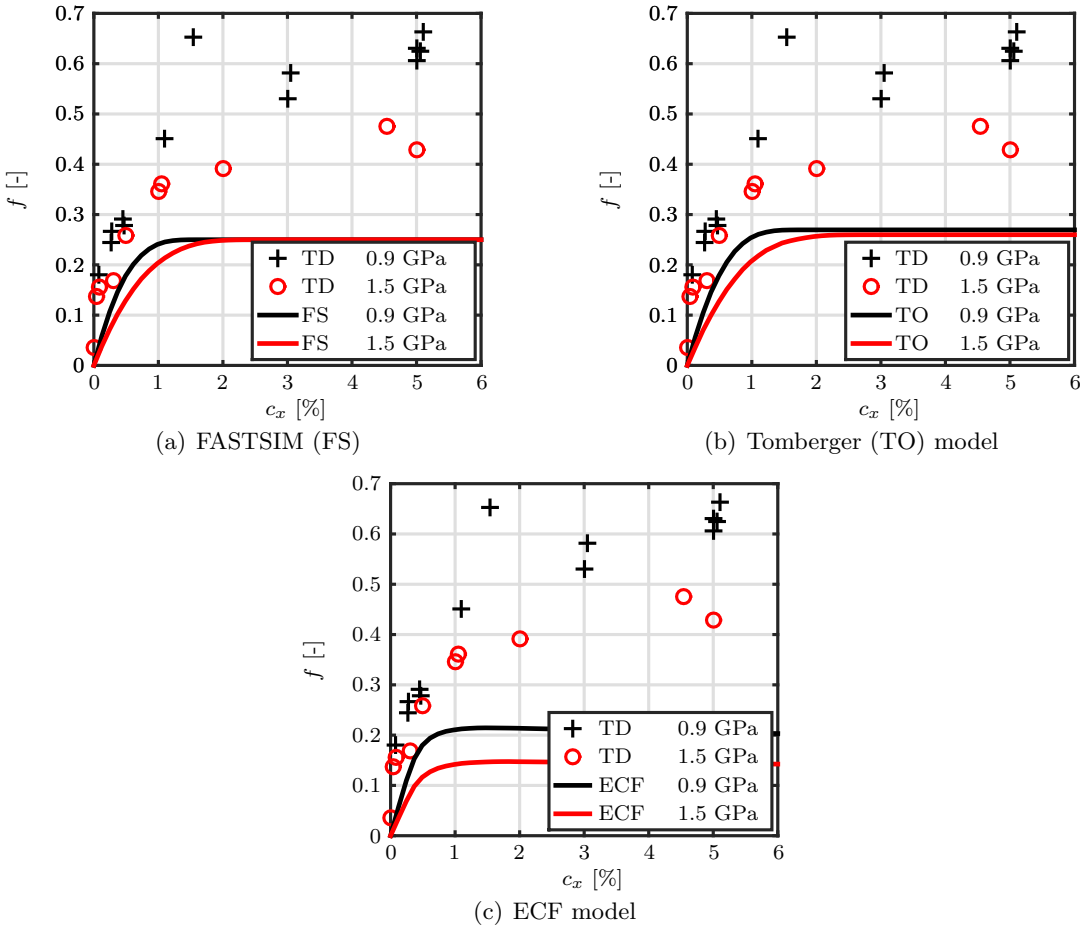

(a) FASTSIM (FS)

(b) Tomberger (TO) model

(c) ECF model

Fig. 6.7: Comparison of the traction coefficient (f) depending on the longitudinal creepage (c_x) measured on the Twin-Disc (TD) test machine vs. three different models from the literature and the newly developed ECF model for the same set of parameters as in Section 6.1.

present. Additionally, a 3BL occurring on a real track might vanish due to wind and other natural influences that do not exist under laboratory conditions. So, it can be reasoned that the thickness of the 3BL was much less during the vehicle tests and the HPT tests than during the Twin-Disc tests. Investigations showed that the 3BL encountered during the Twin-Disc tests consists of iron and, more importantly, iron oxides as shown in Section 3.2. Iron oxides are brittle materials with a high yield strength. Hence, a thick layer of iron oxides could cause an increase of friction. This might explain why the results of the HPT tests and the vehicle test are very similar while the Twin-Disc tests show a huge deviation and a higher friction.

To account for this, the parameters of all models were adjusted. In case of FASTSIM, the coefficient of friction was changed from to $\mu = 0.25$ to $\mu = 0.6$. The boundary lubrication factor was changed from $k_b = 0.6$ to $k_b = 1.3$ in the Tomberger model. For the ECF model, the critical shear stresses had to be changed to $\tau_{c1}^0 = 824.64$ Mpa and $\tau_{c2}^0 = 7937.81$ Mpa. This indicates that the 3BL is much harder compared to the HPT

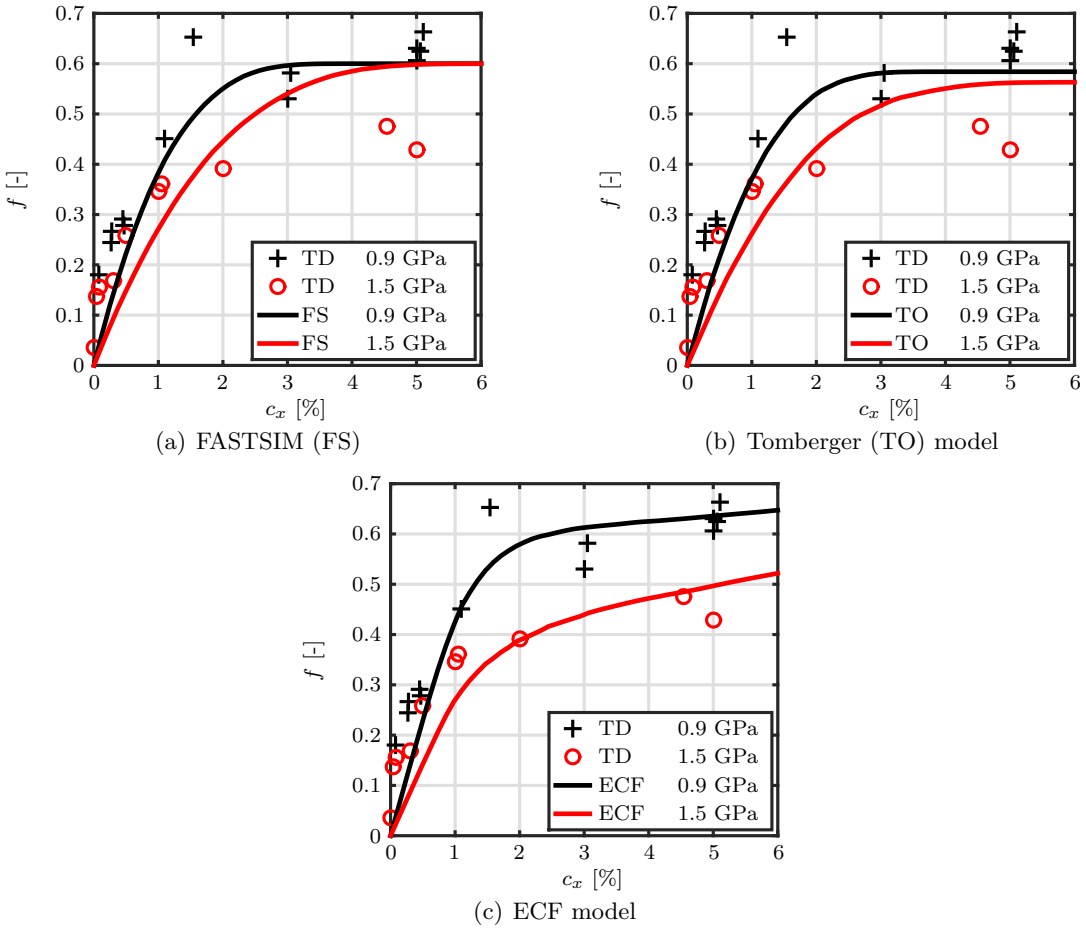

(a) FASTSIM (FS)

(b) Tomberger (TO) model

(c) ECF model

Fig. 6.8: Comparison of the traction coefficient (f) depending on the longitudinal creepage (c_x) measured on the Twin-Disc (TD) test machine vs. two different models from the literature and the newly developed ECF model.

and vehicle tests, strengthening the theory that the higher friction level during the Twin-Disc tests is caused by a high amount of iron oxides in the contact as well as highly strain-hardened steel particles.

The results are shown in Fig. 6.8. Because of the steep increase in traction at low creepages, small uncertainties in the measurement produce large errors. Therefore, the same reasoning as in Section 6.1 is used and only the relative errors for $c_x \geq 0$ were investigated. This is presented in Tab. 6.4.

Table 6.4: The relative error as defined by Eq. (2.9) for $c_x \geq 1$:

Model	0.9 GPa	1.5 GPa	Mean
FASTSIM	11.57%	26.74%	19.16%
Tomberger	12.72%	22.62%	17.67%
ECF	9.076%	14.55%	11.81%

There, it can be seen that the relative error for the ECF model is significantly smaller than for the other two models. The reason is the normal load dependency of the material parameters of the 3BL, which was previously parametrized by using HPT test data.

7 Summary

The goal of this work was to gather a deeper understanding of the dependencies regarding the frictional properties of the wheel-rail contact and to develop a new creep force model that is able to reproduce these dependencies within a small margin of error. Thus, three different experiments were performed during the work presented in this thesis to gain further insight into the problem. The results of these tests were compared to three existing models from the literature: FASTSIM [18], Polach model [33], and Tomberger model [37].

- A part of this work were Vehicle tests that were performed at the Siemens test ring in Wildenrath. There, the dependency of the traction coefficient on creepage, vehicle speed, contact conditions, and different sections were investigated on different days. In addition, drive-train oscillations were monitored. The results of these investigations showed that the most important parameters in these tests were the vehicle speed, the creepage, and the contact conditions. The models from the literature were not able to replicate the measured traction characteristics satisfyingly: either they were not able to reproduce the dependencies (FASTSIM and Tomberger model) or they were only phenomenological and no deeper understanding of the underlying effects could be gained (Polach model). The resulting errors were 39% in case of FASTSIM, 17% in case of the Polach model, and 19% for the Tomberger model.
- Another part of the work presented here were Twin-Disc tests, performed at the SUROS test rig of the University of Sheffield, to investigate the formation of a Third Body Layer (3BL). This layer is said to influence the traction characteristic and might explain the differences between the results measured at the vehicle tests and the models from the literature, i.e., FASTSIM and the Tomberger model [13, 54]. The Twin-Disc tests showed a 3BL consisting of iron and iron oxide with a maximum thickness of 50 µm. In addition, the normal load and speed dependency of the contact forces were investigated. Again, the results were compared to the existing models from the literature. None of these models was able to replicate the normal load dependency correctly, the resulting errors were 19% for FASTSIM and 18% in case of the Tomberger model.
- To investigate the influence of contaminants and the normal load dependency more closely, High Pressure Torsion tests were planned and performed at the Erich Schmid Institute in Leoben as part of the presented work. To the authors knowledge, this was a novel approach to investigate the frictional behaviour for high pressures. Those

tests consisted of two discs that were rotated against each other and then pressed together with a normal stress of up to 1 GPa. The resulting shear stress and the displacement were measured. The normal load and the contact conditions were varied. The results showed a non-linear dependency of the friction on the displacement, similar to strain-hardening known from elasto-plastic solids, and the applied normal load, similar to the behaviour of granular materials even for dry contact.

Summarizing and comparing the collected measurement data, it became clear that a new creep force model had to be developed to describe all the measured effects. The core of the Extended Creepforce (ECF) model, which was developed in the presented here, was the description of the 3BL, which is considered to consist of fluids and solid particles in between wheel and rail, as well as the surface layers of wheel and rail, including asperities and micro-cracks with a depth in the order of micrometers. In the 3BL sub-model used in the ECF model, the layer is modelled as a homogeneous and isotropic material with temperature and normal stress dependent elasto-plastic properties. Thus, it is possible to reproduce the strain-hardening like behaviour and granular material behaviour observed during the HPT tests. Therefore, exponential material laws are assumed, resulting in twelve parameters. In contrast to, e.g., the Polach model, these parameters do all have a physical meaning and can be measured by laboratory tests instead of full vehicle tests. It is also worth noting that the whole model is formulated to include full time dependencies, which allows the ECF model to reproduce transient effects caused by rapid changes of creepages, normal load, or contact geometry.

Next, the twelve material coefficients had to be parametrized. Eight of these parameters were adjusted by comparing the results of the 3BL sub-model to the results of the HPT tests. There, the normal load dependency and the dependency on different contact conditions was calibrated. A single result from the vehicle tests for dry conditions and a single one for wet conditions were used to parametrize the remaining four parameters that are responsible for the temperature influence on the material properties. The resulting errors were 9% in both cases.

The resulting parametrized model was validated for steady and unsteady state by comparing its results to different results from the vehicle tests and the Twin disc tests. In contrast to the existing models from the literature, it was shown that the new ECF model was able to qualitatively and quantitatively reproduce the influence of the creepage, the velocity, contact conditions, and the normal load, which none of the existing models was able to do. The error between measurement and model was reduced from 39% (FASTSIM), 17% (Polach model), and 19% (Tomberger model) to 10% for the ECF model for vehicle tests. For the Twin-Disc tests, the error was 12% (ECF model) compared to 19% in case of FASTSIM and 18% for the Tomberger model.

It was then implented in SIMPACK, a MBS software, to show that it was able to reproduce drive-train oscillations observed during measurements, including the hysteresis caused by

the transient behaviour. The resulting relative error was 7%.

The ECF model is now a completely parametrized model relying on physically measurable parameters that includes a creepage, normal load, and velocity dependency. It is able to reproduce the initial increase of traction for low creepages, the moderate increase for medium creepages, and the traction loss for high creepages as seen in the measurements. In addition, it is able to reproduce quasi-steady and transient behaviour like the occurrence of a hysteresis due to oscillations of the creepage. The computational effort is kept minimal, which leads to the possibility of implementing the ECF model into MBS software. In the future, the ECF model will be used for a multitude of applications, ranging from the investigation of the dynamic behaviour of railway vehicles with MBS software, which can be used for dimensioning of vehicles, to traction estimation, which will lead to an improvement of wear and damage prediction and an optimization of traction and braking control devices.

References

[1] H. H. Weber, Untersuchungen und Erkenntnisse über das Adhäsionsverhalten elektrischer Lokomotiven, Teil 1, Elektrische Bahnen 8 (1966) 181–190.

[2] C. F. Logston, G. S. Itami, Locomotive friction creep studies, Journal of Engineering for Industry 102 (1980) 275–281.

[3] W. Lang, G. Roth, Optimale Kraftschlussausnutzung bei Hochleistungs-Schienenfahrzeugen, Eisenbahntechnische Rundschau 42 (1993) 61–66.

[4] K. Knothe, R. Wille, B. W. Zastrau, Advanced contact mechanics - road and rail, Vehicle System Dynamics 35 (2001) 361–407.

[5] H. Fiehn, M. Weinhardt, N. Zeevenhooven, Drehstromversuchsfahrzeug der Niederländischen Eisenbahnen-Adhäsionsmessungen, Elektrische Bahnen 77 (1979) 329–338.

[6] O. Polach, Optimierung moderner Lok-Drehgestelle durch fahrzeugdynamische Systemanalyse, Eisenbahningenieur 53 (2002) 50–57.

[7] T. Ohyama, M. H., Traction and slip at higher rolling speeds: some experiments under dry friction and water lubrication, in: Proceedings of 1st International Conference on Contact Mechanics and Wear of Rail/Wheel Systems, 1982, pp. 395–418.

[8] D. I. Fletcher, A new two-dimensional model of rolling-sliding contact creep curves for a range of lubrication types, Proceedings of the Institution of Mechanical Engineers, Part J: Journal of Engineering Tribology 227 (2012) 529–537.

[9] D. Fletcher, S. Lewis, Creep curve measurement to support wear and adhesion modelling, using a continuously variable creep twin disc machine, Wear 298-299 (2013) 57–65.

[10] H. H. Weber, Untersuchungen und Erkenntnisse über das Adhäsionsverhalten elektrischer Lokomotiven, Teil 2, Elektrische Bahnen 9 (1966) 209–215.

[11] W. Zhang, J. Chen, X. Wu, X. Jin, Wheel/rail adhesion and analysis by using full scale roller rig, Wear 253 (2002) 82–88.

[12] A. Meierhofer, C. Hardwick, R. Lewis, K. Six, P. Dietmaier, Third body layer - experimental results and a model describing its influence on the traction coefficient, Wear 314 (2014) 148–154.

[13] K. Hou, J. Kalousek, E. Magel, Rheological model of solid layer in rolling contact, Wear 211 (1997) 134–140.

[14] M. Tomeoka, N. Kabe, M. Tanimoto, E. Miyauchi, M. Nakata, Friction control between wheel and rail by means of on-board lubrication, Wear 253 (2002) 124–129.

[15] A. Matsumoto, Y. Sato, H. Ono, Y. Wang, M. Yamamoto, M. Tanimoto, Y. Oka, Creep force characteristics between rail and wheel on scaled model, Wear 253 (2002) 199–203.

[16] E. Gallardo-Hernandez, R. Lewis, Twin disc assessment of wheel/rail adhesion, Wear 265 (2008) 1309–1316.

[17] A. Haigermoser, Schienenfahrzeuge, Technische Universität Graz, Maschinenbau, 2002.

[18] J. Kalker, Wheel-rail rolling contact theory, Wear 144 (1991) 243–261.

[19] K. L. Johnson, Contact Mechanics, Cambridge University Press, Cambridge, UK, 1985.

[20] K. Knothe, S. Stichel, Schienenfahrzeugdynamik, Springer Verlag, 2003.

[21] A. Alonso, J. Gimenez, Non-steady state modelling of wheel-rail contact problem for the dynamic simulation of railway vehicles, Vehicle System Dynamics 46 (2008) 179–196.

[22] S. Diaz, Analysis and Modelling of Unsteady Effects within the Wheel-Rail Contact, Master's thesis, Graz University of Technology, 2012.

[23] F. Alwahdi, A. Kapoor, F. Franklin, Subsurface microstructural analysis and mechanical properties of pearlitic rail steels in service, Wear 302 (2013) 1453–1460.

[24] G. Trummer, K. Six, C. Marte, P. Dietmaier, C. Sommitsch, An approximate model to predict near-surface ratcheting of rails under high traction coefficients, Wear 314 (2014) 28–35.

[25] G. Trummer, K. Six, C. Marte, A. Meierhofer, C. Sommitsch, Automated measurement of near-surface plastic shear strain, in: J. Pombo (Ed.), Proceedings of the Second International Conference on Railway Technology: Research, Development and Maintenance, 2014, Civil-Comp Press, Stirlingshire, United Kingdom, 2014.

[26] H. Hertz, Ueber die Berührung fester elastischer Körper, Journal für die reine und angewandte Mathematik 92 (1882) 156–171.

[27] B. Girstmair, Vergleich von Rad-Schiene Kontaktmodellen und deren Einfluss auf den Kraftschluss, Master's thesis, Graz University of Technology, 2012.

[28] J. J. Kalker, Three-dimensional elastic bodies in rolling contact, Kluwer Academic Press, 1990.

[29] C. Linder, Verschleiß von Eisenbahnrädern mit Unrundheiten, Ph.D. thesis, ETH Zürich, 1997.

[30] W. Kik, J. Piotrowski, A fast, approximate method to calculate normal load at contact between wheel and rail and creep forces during rolling, in: 2nd Mini Conference of Contact Mechanics and Wear of Rail-Wheel Systems, Budapest, 1996.

[31] J.-B. Ayasse, H. Chollet, Handbook of Railway Vehicle Dynamics, Taylor & Francis, pp. 85–120.

[32] A. Aichmayr, Generalization of a New Creepforce Model to Non-Elliptic Contact Conditions, Master's thesis, Karl-Franzens-University Graz, 2012.

[33] O. Polach, Creep forces in simulations of traction vehicles running on adhesion limit, Wear 258 (2005) 992–1000.

[34] M. Spiryagin, O. Polach, C. Cole, Creep force modelling for rail traction vehicles based on the fastsim algorithm, Vehicle System Dynamics: International Journal of Vehicle Mechanics and Mobility 51 (2013) 1765–1783.

[35] E. A. Vollebregt, Numerical modeling of measured railway creep versus creep-force curves with contact, Wear 314 (2014) 87–95.

[36] A. Alonso, J. G. Gimenez, Non-steady state contact with falling friction coefficient, Vehicle System Dynamics 46 (2008) 779–789.

[37] C. Tomberger, P. Dietmaier, W. Sextro, K. Six, Friction in wheel-rail contact: A model comprising interfacial fluids, surface roughness and temperature, Wear 271 (2011) 2–12.

[38] Y. Zhu, U. Olofsson, An adhesion model for wheel-rail contact at the micro level using measured 3d surfaces, Wear 314 (2014) 162–170.

[39] A. Schenk, M. Sinapius, Die experimentelle Modalanalyse des Intercity-Experimental auf dem Rollprüfstand, Eisenbahntechnische Rundschau Heft 4 (1991) 245–251.

[40] A. Jaschinski, H. Chollet, S. Iwnicki, A. Wickens, J. von Würzen, The application of roller rigs to railway vehicle dynamics, Vehicle System Dynamics 31 (1999) 345–392.

[41] A. Matsumoto, Y. Sato, H. Ohno, M. Tomeoka, K. Matsumoto, T. Ogino, M. Tanimoto, Y. Oka, M. Okano, Improvement of bogie curving performance by using friction modifier to rail/wheel interface: Verification by full-scale rolling stand test, Wear 258 (2005) 1201 – 1208.

[42] I. J. McEwen, R. F. Harvey, Full-scale wheel-on-rail wear testing: Comparisons with service wear and a developing theoretical predictive method, Lubrication Engineering 41 (1985) 80 – 88.

[43] M. C. Burstow, Rolling Contact Fatigue Laboratory Testing, Technical Report AEATR-ES-2004-907, Rail Safety and Standards Board (RSSB), 2006.

[44] R. Stock, D. T. Eadie, D. Elvidge, K. Oldknow, Influencing rolling contact fatigue through top of rail friction modifier application - a full scale wheel-rail test rig study, Wear 271 (2011) 134 – 142.

[45] J. H. Beynon, J. E. Garnham, K. J. Sawley, Rolling contact fatigue of three pearlitic rail steels, Wear 192 (1996) 94–111.

[46] Y.-C. Chen, L.-W. Chen, Effects of insulated rail joint on the wheel/rail contact stresses under the condition of partial slip, Wear 260 (2006) 1267–1273.

[47] E. Gallardo-Hernandez, R. Lewis, R. Dwyer-Joyce, Temperature in a twin-disc wheel/rail contact simulation, Tribology International 39 (2006) 1653–1663.

[48] O. Arias-Cuevas, Z. Li, R. Lewis, E. Gallardo-Hernandez, Laboratory investigation of some sanding parameters to improve the adhesion in leaf-contaminated wheel-rail contacts, in: Proceedings of the Institution of Mechanical Engineers, Part F: Journal of Rail and Rapid Transit, Volume 224, 2010, pp. 139–157.

[49] O. Arias-Cuevas, Z. Li, R. Lewis, E. Gallardo-HernÃ¡ndez, Rolling-sliding laboratory tests of friction modifiers in dry and wet wheel-rail contacts, Wear 268 (2010) 543–551.

[50] G. Donzella, M. Faccoli, A. Mazzù, C. Petrogalli, R. Roberti, Progressive damage assessment in the near-surface layer of railway wheel-rail couple under cyclic contact, Wear 271 (2011) 408 – 416.

[51] R. Lewis, R. Dwyer-Joyce, S. Lewis, C. Hardwick, E. Gallardo-Hernandez, Tribology of the wheel-rail contact: The effect of third body materials, International Journal of Railway Technology 1 (2012) 1.

[52] S. Descartes, A. Saulot, C. Godeau, S. Bondeux, C. Dayot, Y. Berthier, Wheel flange/rail gauge corner contact lubrication: Tribological investigations, Wear 271 (2011) 54–61.

[53] S. Descartes, Y. Berthier, Rheology and flows of solid third bodies: background and application to an mos1.6 coating, Wear 252 (2002) 546–556.

[54] S. Descartes, C. Desrayaud, E. Niccolini, Y. Berthier, Presence and role of the third body in a wheel-rail contact, Wear 258 (2005) 1081–1090.

[55] J. Garnham, J. Beynon, The early detection of rolling-sliding contact fatigue cracks, Wear 144 (1991) 103–116.

[56] D. I. Fletcher, J. H. Beynon, Development of a machine for closely controlled rolling contact fatigue and wear testing, Journal of Testing and Evaluation 28 (2000) 267–275.

[57] N. Ramakrishnan, V. S. Arunachalam, Effective elastic moduli of porous ceramic materials, Journal of the American Ceramic Society 76 (1993) 2745–2752.

[58] K. T. Kim, S. W. Choi, H. Park, Densification behavior of ceramic powder under cold compaction, Journal of Engineering Materials and Technology 122 (2000) 238–244.

[59] K. Kim, J. Cho, A densification model for mixed metal powder under cold compaction, International Journal of Mechanical Sciences 43 (2001) 2929–2946.

[60] H. Kim, O. Gillia, P. Dorémus, D. Bouvard, Near net shape processing of a sintered alumina component: adjustment of pressing parameters through finite element simulation, International Journal of Mechanical Sciences 44 (2002) 2523–2539.

[61] S. Dartevelle, Numerical and granulometric approaches to geophysical granular flows, Ph.D. thesis, Michigan Technological University, Department of Geological and Mining Engineering, Houghton, Michigan, 2003.

[62] C. Martin, D. Bouvard, S. Shima, Study of particle rearrangement during powder compaction by the discrete element method, Journal of the Mechanics and Physics of Solids 51 (2003) 667–693.

[63] D. Kadau, Porosität in kohäsiven granularen Pulvern und Nano-Pulvern, Ph.D. thesis, Fakultät der Naturwissenschaften der Universität Duisburg-Essen, 2004.

[64] F. Nicot, F. Darve, R. G. N. Hazards, V. of Structures, A multi-scale approach to granular materials, Mechanics of Materials 37 (2005) 980–1006.

[65] S. Lee, K. Kim, A study on the cap model for metal and ceramic powder under cold compaction, Materials Science and Engineering: A 445-446 (2007) 163–169.

[66] J.-F. Jerier, B. Hathong, V. Richefeu, B. Chareyre, D. Imbault, F.-V. Donze, P. Doremus, Study of cold powder compaction by using the discrete element method, Powder Technology 208 (2011) 537–541.

[67] M. Ertz, K. Knothe, A comparison of analytical and numerical methods for the calculation of temperatures in wheel/rail contact, Wear 253 (2002) 498–508.

[68] I. Goryacheva, F. Sadeghi, Contact characteristics of a rolling/sliding cylinder and a viscoelastic layer bonded to an elastic substrate, Wear 184 (1995) 125–132.

[69] S. Alexandrov, A property of equations of rigid/plastic material obeying a voce-type hardening law, Meccanica 34 (1999) 349–356.

[70] Jöller, Temperatureinfluß auf die mechanischen Eigenschaften von Schienenwerkstoffen, Technical Report, Voest-Alpine Stahl Donawitz GmbH, 1992.

[71] C. Tomberger, Der Rad-Schiene Kraftschluss unter Berücksichtigung von Temperatur, fluiden Zwischenschichten und mikroskopischer Oberflächenrauheit, Ph.D. thesis, Technische Universität Graz, 2009.

[72] Gottscheid, Physikalische Grundlagen der Materialkunde, Springer-Verlag Berlin Heidelberg, 2007.

List of Figures

List of Tables